Scholar Commons
USF University of South Florida

University of South Florida
Scholar Commons

Graduate Theses and Dissertations | Graduate School

8-24-2010

Interface Modifications with Atomic Monolayer

Jayeeta Lahiri
University of South Florida

Follow this and additional works at: http://scholarcommons.usf.edu/etd

 Part of the American Studies Commons

Scholar Commons Citation
Lahiri, Jayeeta, "Interface Modifications with Atomic Monolayer" (2010). *Graduate Theses and Dissertations.*
http://scholarcommons.usf.edu/etd/3641

This Dissertation is brought to you for free and open access by the Graduate School at Scholar Commons. It has been accepted for inclusion in Graduate Theses and Dissertations by an authorized administrator of Scholar Commons. For more information, please contact scholarcommons@usf.edu.

Interface Modifications with Atomic Monolayer

by

Jayeeta Lahiri

A dissertation submitted in partial fulfillment
of the requirements for the degree of
Doctor of Philosophy
Department of Physics
College of Arts and Sciences
University of South Florida

Major Professor: Matthias Batzill Ph.D.
Srikanth Hariharan, Ph.D.
Sarath Witanacch, Ph.D.
Martin Munoz, Ph.D
Rudy Schlaf, Ph.D

Date of Approval
August 24, 2010

Keywords: surface science, zinc oxide, nickel, graphene, carbide

Copyright © 2010, Jayeeta Lahiri

ACKNOWLEDMENTS

I would like to take this opportunity to express my gratitude to all those who helped me directly and indirectly with my research work to finish this dissertation.

I owe my deepest gratitude to my advisor Dr Matthias Batzill, Assistant Professor Department of Physics, for his support and guidance during my research. I will always be grateful to him for the numerous discussions we had during our group meeting. I am thankful for his valuable suggestions and his patience, during writing of this dissertation. I really appreciate my collaborators Dr Ivan Oleynik and his group for their theoretical calculations supporting my experimental work. I would also like to thank committee members for their advice and suggestions.

I would also like to give special thanks to Timothy Luttrell, my fellow lab member for his help in practical aspects of experimental work in lab. I am also thankful to Travis, REU student, who completed some experiments needed for completion of my thesis. I would also like to thank all the postdocs in our lab for their suggestions.

I would like to thank my parents and family for their constant support and inspiration. I am also grateful to my in-laws for taking care of my beloved son for the past there years, without which it would have been impossible to complete my PhD. Last but not least, I would also give thanks to my wonderful and supportive husband “Avanish S Parmar” for his constant encouragement and unconditional love.

TABLE OF CONTENTS

LIST OF TABLES

LIST OF FIGURES

1. INTRODUCTION

Surfaces and interfaces have played a critical role in many developments in technologically important research areas like semiconductor devices, corrosion, lubrication, heterogeneous catalysis, gas sensors, spintronics etc. [1-5]. Moreover most of the biochemical reactions that sustain life occur at biological surfaces and interfaces [6-8]. The performance of most semiconductor devices depends on the electronic properties of the semiconductor at the surface or interface [9, 10]. The chemistry of surfaces defines catalytic reactions. Vacuum surface science studies have played a central role in understanding the complex interactions that occur during molecule adsorption and reactions. This contribution of over 30 years of surface science to elucidate heterogeneous catalysis was recently acknowledged by awarding the Nobel Prize for Chemistry to Gerhard Ertl one of the preeminent researchers in this field [11-14]. Chemical solid state sensors obtain their sensitivity from the adsorption properties of gases and the changes this adsorption induces in the physical properties of the material. A common sensing material is, for example, ZnO, one of the materials studied in this work. The surface adsorption of molecules influences the bulk conductivity by charge transfer from the *n*-type semiconducting ZnO to the adsorbate. This change in electrical conductivity is exploited as the gas sensing signal and monitoring its changes can for example detect reducing or oxidizing gases. A typical application is the detection of poisonous and odorless CO [15, 16]. In the realization of spintronics, the injection of

spin-polarized electrons across ferromagnet - semiconductors interfaces is a major challenge and the interface properties play an important role [17, 18]. Discovery of magnetism in graphene has opened up possibilities for spintronics applications [19]. Therefore understanding and controlling surface and interface properties have large impact for diverse applications.

Research in surface and interface science is highly interdisciplinary, including the fields of physics, chemistry, material science, chemical engineering, bio-physics, geo-physics and more. Various advanced surface science experimental techniques have helped us increase our understanding of material surfaces and interfaces, and also our ability to control and tune the surface and interfacial characteristics for specific applications. Current surface science research focuses on atomic level studies of the structure (atomic and electronic), reactivity, dynamics, and magnetism at the surfaces and interfaces of different systems (like metals, oxides, polymers, biological molecules, liquids etc.). We focused on studying the surface and interface properties of oxides (i.e. ZnO) and graphene nickel interfaces.

Zinc oxide (ZnO) has received considerable attention because of its unique optical, semiconducting, and piezoelectric properties. It is used in numerous applications like, as transparent conducting electrode in solar cells, light emitting diodes and flat panel displays, as catalyst in methanol synthesis, as photocatalyst for hydrogen production from water, as chemical and biological sensors, etc [20-22]. ZnO has seen some intensive research in the past and still continues to maintain its interest with researchers due to the

ability to tune its electronic and optical properties by doping, alloying, heterostructures and nanostructures (quantum wells, nanorods etc)[23, 24].

Our research on ZnO was focused on studying the electronic properties of the ZnO/ZnS interface (both wide band semiconductors), using photoemission spectroscopy. Both ZnO and ZnS are photocatalytically active materials, however, their wide band gap limits their photoactivity to the UV-range of the spectrum. For solar light applications photoactivity in the visible range of the spectrum needs to be achieved. Our goal was to investigate if hybrid-materials consisting of two wide-band gap materials, such as ZnO and ZnS, could achieve visible light activity at the interfaces of these two materials. We were able to demonstrate that the surface band gap at the interface is, indeed decreased by 1 eV. This decrease demonstrates the potential of using wide band gap materials to engineer hybrid materials with potential visible light activity for specific interface structures [25]. Additionally to the applied studies we also investigate the stabilization mechanisms of the two polar surfaces of ZnO by soft x-ray photoemission spectroscopy. The stability of polar surfaces is a fundamental problem in surface science of ionic materials. For ZnO the apparent stability of 1x1 surfaces, i.e. surfaces that do not exhibit a higher periodic surface reconstruction, has been a mystery for a long time. For decades surface scientists were puzzled how the polar surfaces of ZnO could exist in this apparent bulk truncation, which is an inherently unstable configuration due to a diverging Madelung energy. Many different theories have been developed to explain how this surface may be stabilized. Our studies contribute to finally solving this mystery. Using soft x-ray and UV photoemission the surface electronic structure and composition could be identified. For the O-terminated side we observed charge transfer resulting in a surface

band bending for a clean surface at elevated temperatures while at room temperature the surface was always stabilized by hydrogen adsorption [26].

Graphene has shown promising electronic properties as a future material for device applications beyond the current technology based on silicon microelectronics. To fabricate graphene based devices, it is necessary to integrate various material components with different electronic properties such as metals, insulators, and semiconductors (both organic and inorganic). Fundamental properties of such components in graphene-based devices can be studied by investigating MG/M, MG/M1/M2 and Ad/MG/M interfaces (MG, M and Ad stands for monolayer of graphene, metal and adsorbate respectively).

Our goal is to study the morphology, chemical and electronic properties of such graphene interfaces using surface science experimental techniques like scanning tunneling microscopy (STM), temperature programmed desorption (TPD) and photoemission spectroscopy. In particular we have focused on the growth and interface formation between graphene and Ni surfaces. Graphene growth on planar Ni-catalysts has been known in the surface science community for decades. With the recent excitement in graphene these growth phenomena have experienced a huge burst of interest. In our research we showed for the first time that graphene can grow on Ni in two different growth modes. It either grows as an atomic sheet on top of the Ni-surface plane, which has been assumed to be the dominant growth mechanism, or it can grow by converting a surface confined Ni_2C phase into graphene. In both cases carbon is provided by segregation from the bulk. In the latter growth mode a one dimensional line interface is formed between the nickel carbide and the graphene which is a unique characteristics for

graphene growth on Ni. In further studies we found new ways of patterning graphene if supported on Ni and also demonstrated new one-dimensional carbon structures that are formed as extended defects in graphene sheets if grown on Ni(111) substrates [27, 28]. In this case the Ni(111) surface acts as an atomic-template to translate the graphene sheets by an appropriate vector to position carbon atoms with atomic precision to form new structures.

The thesis is organized as follows:

In Chapter 2 we describe some basic surface science background and experimental methods and techniques central to the remainder of this thesis. The first two sections of this chapter will provide conceptual introduction to polar surfaces, adsorption and adsorbate induced change in electronic properties of semiconductors. In the third section different experimental techniques used to study surface and interface properties are discussed. In the fourth section we briefly describe one ultra high vacuum chamber where some of the experiments were conducted. Finally, sample preparation methods are described.

Chapter 3 is organized in three sections: introduction, results& discussion and conclusion. In the introduction section we briefly discuss some properties of bulk ZnO, focus on the surface properties of ZnO and the stabilization mechanisms of ZnO polar surfaces. In the result and discussion section we discuss our experimental results on ZnO. This is subdivided in two parts: (a) Stabilization of clean ZnO polar surfaces- here we discuss the surface effects in the core-level photoemission spectra of ZnO and use this information to understand the stabilization mechanism of the polar surfaces of ZnO; (b)

functionalization of ZnO with a monolayer of ZnS-here we discuss the interface electronic properties between ZnS/ZnO (model system for coupled semiconductor photocatalysts) and demonstrate that combination of ZnO and ZnS, two wide band gap photocatalysts can yield a material with lower photoexcitation threshold than the individual components. In the final section we discuss the conclusion of our results.

Chapter 4 is organized in five sections. The first section gives a brief introduction to the properties of graphene and methods for its fabrication. The second one gives an introduction to graphene on transition metal substrates. The third section discusses carbon phases on Ni surfaces, especially the Ni(111) substrate. The fourth section presents my results and discussion of my graphene research on nickel-graphene interfaces. This section is further subdivided in four subsections: (a) Growth and stability of graphene on Ni(111) surfaces; (b) growth of graphene from surface carbide using STM; (c) Growth and stability of Ni clusters deposited on graphene/Ni(111) substrate; (d) One dimensional extended defect in graphene/Ni(111) substrate. In the final section we discuss the conclusions.

Chapter 5 provides the summary of results and also presents future research possibilities.

1.1 References

1. Allara, D.L., *A perspective on surfaces and interfaces.* Nature, 2005. **437**(7059): p. 638-639.

2. Duke, C.B., E.W. Plummer, and ScienceDirect (Online service), *Frontiers in surface and interface science*, in *Surface science, v.500, nos 1-3 (10 March 2002.).* 2002, Elsevier: Amsterdam.

3. Duke, C.B., *The birth and evolution of surface science: Child of the union of science and technology.* Proceedings of the National Academy of Sciences of the United States of America, 2003. **100**(7): p. 3858-3864.

4. Smith, G.C., *Surface analytical science and automotive lubrication.* Journal of Physics D-Applied Physics, 2000. **33**(20): p. R187-R197.

5. Marcus, P., *Surface science approach of corrosion phenomena.* Electrochimica Acta, 1998. **43**(1-2): p. 109-118.

6. Castner, D.G. and B.D. Ratner, *Biomedical surface science: Foundations to frontiers.* Surface Science, 2002. **500**(1-3): p. 28-60.

7. Nel, A.E., et al., *Understanding biophysicochemical interactions at the nano-bio interface.* Nat Mater, 2009. **8**(7): p. 543-557.

8. Fragneto, G., *Biological Physics near Surfaces/Interfaces: a Perspective.* European Physical Journal E, 2009. **30**(2): p. 239-243.

9. Lüth, H., *Solid surfaces, interfaces and thin films*. 4th, rev. and extended ed. Advanced texts in physics,. 2001, Berlin ; New York: Springer. xiii, 559 p.

10. Lüth, H., *Surfaces and interfaces of solid materials*. 3rd ed. 1995, Berlin ; New York: Springer. xii, 495 p.

11. Somorjai, G.A. and J.Y. Park, *The impact of surface science on the commercialization of chemical processes.* Catalysis Letters, 2007. **115**(3-4): p. 87-98.

12. Ertl, G., *Reactions at Surfaces: From Atoms to Complexity (Nobel Lecture)13.* Angewandte Chemie International Edition, 2008. **47**(19): p. 3524-3535.

13. Keil, F.J., *Catalytic reactions and reactors.* Chemical Engineering Science. **59**(22-23): p. 5473-5478.

14. Somorjai, G.A., *Introduction to surface chemistry and catalysis*. 1994, New York: Wiley. xxiv, 667 p.

15. Chaniotakis, N. and N. Sofikiti, *Novel semiconductor materials for the development of chemical sensors and biosensors: A review.* Analytica Chimica Acta, 2008. **615**(1): p. 1-9.

16. Janata, J. and M. Josowicz, *Conducting polymers in electronic chemical sensors.* Nat Mater, 2003. **2**(1): p. 19-24.

17. Zutic, I., J. Fabian, and S. Das Sarma, *Spintronics: Fundamentals and applications.* Reviews of Modern Physics, 2004. **76**(2): p. 323-410.

18. Fabian, J., et al., *Semiconductor spintronics.* Acta Physica Slovaca, 2007. **57**(4-5): p. 565-907.

19. Kan, E.J., Z.Y. Li, and J.L. Yang, *Magnetism in graphene systems.* Nano, 2008. **3**(6): p. 433-442.

20. Klingshirn, C., *ZnO: Material, physics and applications.* Chemphyschem, 2007. **8**(6): p. 782-803.

21. Klingshirn, C., *ZnO: From basics towards applications.* Physica Status Solidi B-Basic Solid State Physics, 2007. **244**(9): p. 3027-3073.

22. Ozgur, U., D. Hofstetter, and H. Morkoc, *ZnO Devices and Applications: A Review of Current Status and Future Prospects.* Proceedings of the Ieee. **98**(7): p. 1255-1268.

23. Jagadish, C. and S.J. Pearton, *Zinc oxide bulk, thin films and nanostructures : processing, properties and applications*. 2006, Amsterdam ; London: Elsevier. ix, 589 p.

24. Schmidt-Mende, L. and J.L. MacManus-Driscoll, *ZnO - nanostructures, defects, and devices.* Materials Today, 2007. **10**(5): p. 40-48.

25. Lahiri, J. and M. Batzill, *Surface functionalization of ZnO photocatalysts with monolayer ZnS.* Journal of Physical Chemistry C, 2008. **112**(11): p. 4304-4307.

26. Lahiri, J., S. Senanayake, and M. Batzill, *Soft x-ray photoemission of clean and sulfur-covered polar ZnO surfaces: A view of the stabilization of polar oxide surfaces.* Physical Review B, 2008. **78**(15): p. 10.

27. J. Lahiri, Y.L., P. Bozkurt, I. I. Oleynik, M. Batzill, *An extended defect in graphene as a metallic wire,* in *Nature Nanotech.* 2010. p. 326.

28. J. Lahiri, M.B., *Graphene destruction by metal-carbide formation: An approach for patterning of metal-supported graphene,* in *Appl. Phys. Lett.* 2010.

2. CONCEPTS

In this chapter, we describe some basic surface science background and experimental methods and techniques central to the remainder of this thesis. The first two sections of this chapter will provide conceptual introduction to polar surfaces, adsorption and adsorbate induced change in electronic properties of semiconductors. In the third section different experimental techniques used to study surface and interface properties are discussed. In the fourth section we briefly describe one ultra high vacuum chamber where some of the experiments were conducted. Finally, sample preparation methods are described.

2.1 Polar surfaces

Ionic solids consist of cations and anions that are held together by the electrostatic interaction between the opposite charges. The surfaces of ionic crystals determine many important properties such as mechanical strength, sintering and shape [1]. The surfaces of ionic crystals can be classified into three different types on the basis of simple electrostatic criterion according to Tasker [1-3]. The stability of a surface depends on the characteristics of the charge distribution in the structural unit which repeats itself in the direction perpendicular to the surface (see Figure 2.1). *Type 1* surfaces are those surfaces where each layer is electrically neutral (i.e. contain equal number of anions and cations) and therefore has a zero dipole moment ($Q=0$, $\mu=0$). For *Type 2* surfaces each layer is not

neutral but the anions and cations are stacked in such a way that the repeat unit has zero total dipole moment (Q≠0, μ=0).*Type 3* surfacets of charged layers stacked in such a fashion that the repeat unit exhibits a dipole moment(Q≠0, μ≠0). Type 3 surfaces are called polar surfaces. Polar oxide terminations are found in many crystallographic structures like rock-salt, spinel, inverse spinel, wurtzite and perovskite [4, 5]. Polar surfaces of compound semiconductors have been extensively studied in the past like zinc blende, zinc oxide etc. [6, 7].

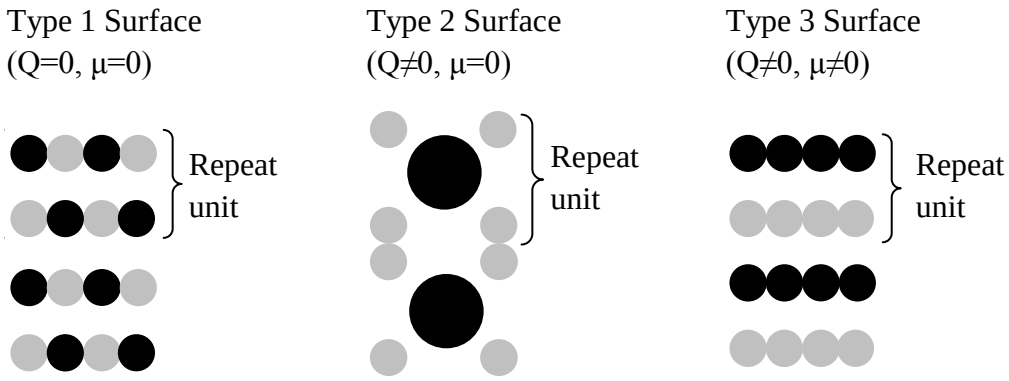

Figure 2.1: Classification of insulating surfaces according to Tasker[1]. *Q* and μ are the layer charge density and the dipole moment in the repeat unit perpendicular to the surface respectively. Black and grey circles represent anion and cation respectively.

The simplest representation of a crystalline compound cut along a polar direction is given in Figure 2.2(a). Two inequivalent atomic layers of opposite charge densities $\pm\sigma$ alternate along the normal to the surface, with interlayer spacings R_1 and R_2 [4]. Each repeat unit has a dipole moment $\mu = \sigma R_1$, and, as a result, the electrostatic potential increases monotonically across the system by an amount $\Delta V = 4\pi\sigma R_1$ per double layer. The total dipole moment of N bilayers is $\mu = N\sigma R_1$, and the electrostatic energy is then

given as $E = 2\pi NR_1\sigma$. The total electrostatic energy is thus proportional to the sample thickness and when $N \to \infty$ it diverges, creating surface instability.

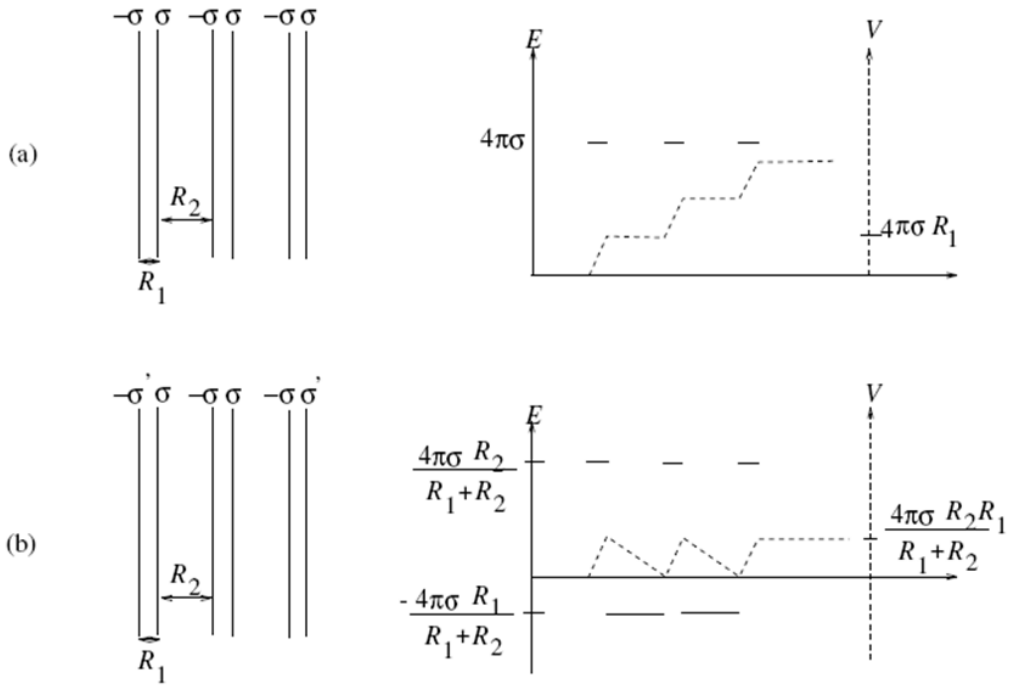

Figure 2.2: Spatial variation of electrostatic field (E) and electrostatic potential (V) in a sample cut along the polar direction (a) When the atomic planes have the opposite charge densities +/- σ the electrostatic potential increases monotonically (b) When the charge density on the outer planes are modified by $\sigma'=\sigma(R_2/R_1+R_2)$ the electrostatic potential does not increase with sample thickness but oscillates around a non zero value. Figure is taken from Ref[2].

This electrostatic instability can be removed by cancelling the dipole moment by the introduction of compensating charges in the outer planes as shown in Figure 2.2(b). If the charge density in the outer planes are modified to $\sigma' = \sigma R_2/(R_1 + R_2)$ then the total dipole moment is $\mu = \sigma R_1 R_2/(R_1 + R_2)$, is no longer proportional to the slab thickness.. Therefore divergence of the electrostatic potential is suppressed as it is no longer proportional to the slab thickness. Thus a polar surface is stabilized by compensating

charges present in the outermost layers [4, 5, 8]. This suggests that either the charges or the stoichiometry in the surface layers are modified with respect to a bulk truncation. There are three scenarios that may provide the necessary surface charges to compensate for the diverging electrostatic potential of polar surfaces: (i) Surface reconstruction that alter the surface composition, (ii) adsorption of impurity atoms that carry a net charge such as hydrogen (protons) or (iii) change in electronic structure that induce surface states [4, 5, 9].

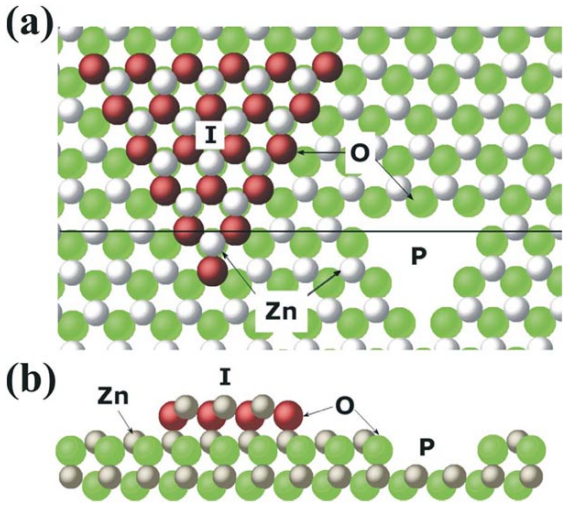

Figure 2.3: Top view of the $ZnO(0001)$-Zn surface showing triangular pits (p) and islands (i). The step edges exhibit three-fold coordinated oxygen atoms compared to the fourfold coordination on the terraces. The cross section indicated in (a) is shown in (b).

For example ZnO which crystallizes in hexagonal wurtzite structure has two polar surfaces; the Zn-terminated $ZnO(0001)$ and O- terminated $ZnO(000\bar{1})$ surface. According to electrostatic arguments ¼ of the surface charge needs to be compensated to stabilize the two polar surfaces of ZnO. This can be achieved by several mechanisms [10-13]. Firstly, surface states may be created by transfer of negative charges from the O-

terminated side to Zn-terminated side without any rearrangement of the ions. This mechanism is also referred as 'metallization of the polar surfaces'. Secondly, adsorbed impurities may change the oxidation state of the ions. Thirdly charge compensation can be achieved by the removal of surface ions which changes the surface stoichiometry inducing surface reconstructions [11]. For the $ZnO(0001)$-Zn surface the probable stabilization of the clean surface in ultrahigh vacuum is by removal of 1/4 ML of Zn atoms from the surface in a nonperiodic manner. This is achieved by formation of high density of triangular shaped pits and ad islands that exhibit step edges that are O-terminated (see Figure 2.3). For the $ZnO(000\bar{1})$-O surface the stabilization mechanism is not fully explained yet and all of the above mentioned stabilization mechanisms have been invoked in the past [14, 15]. In Chapter 3, we discuss soft x-ray photoemission studies to investigate the stabilization mechamism of polar surfaces of ZnO.

2.2 Adsorption

Adsorption of atoms or molecules from their vapor phase to a solid surface occurs when there is attractive interaction between them at short distance from the surface. Depending on the magnitude and origin of these attractive forces and the extent of perturbation of the electronic structures of the adsorbate and the surface, adsorption is broadly classified into two types: physisorption and chemisorption[16].

The attractive forces in physisorption originate from correlated charge fluctuations that develop when an atom or a molecule is brought very close to a solid surface [17]. These attractive forces are van der waals forces. The physisorption of molecules or atoms on a solid surface is characterized by largely unperturbed electronic

structures of both the adsorbate and the solid. Adsorption of noble gas atoms on metal surfaces is a typical example of physisorption [18]. In chemisorption the attractive forces arise from the overlap of adsorbate and surface wave functions or charge transfer. Depending on the extent of the electron transfer, the chemisorptive bond can be ionic or covalent. An ionic bond is characterized by a complete charge transfer between the adsorbate and substrate while a covalent bond is characterized by the sharing of electrons between adsorbate and surfaces. This modifies their electronic structures. The rupture of intramolecular adsorbate bonds and the formation of new surface bonds during chemisorption are important steps in heterogeneous catalysis [17, 19, 20].

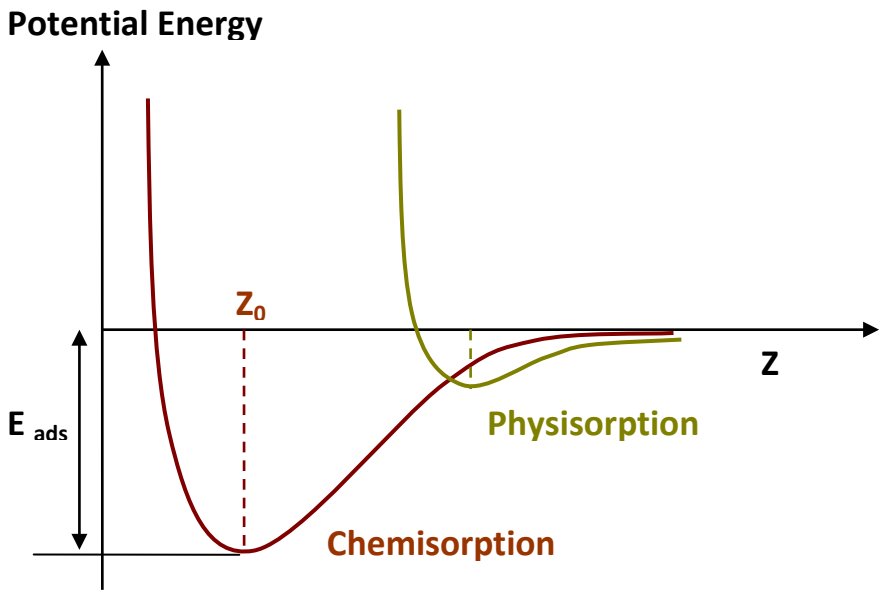

Figure 2.4: Potential energy diagram of physisorption and chemisorption process (Z_0 is the equilibrium distance from the surface and E_{ads} is the adsorption energy)

The physisorption potentials are characterized by a low binding energy E_{ads}, about 10 to 100 meV, and by a relatively large equilibrium separation z_0 , of about 3–10Å, from the surface [17]. Physisorbed particles are therefore located at relatively large distances

from the surface and are therefore highly mobile in the plane parallel to the surface. A qualitative description of the chemisorption potential is similar to the physisorption potential (see Figure 2.4). However, the equilibrium distance, z_0, is much smaller when compared to those of physisorption and typically has values 1–3 Å. Also, chemisorption results in stronger bonding with typical binding energies, E_{ads} of about 1 eV.

2.3. Adsorbate induced changes in electronic properties of semiconductors

Adsorbates can modify both the surface atomic structure and electronic structure. Adsorbates can induce reconstruction of surfaces in different ways [21]. Adsorbates can either produce new reconstructions that were not present on the clean surface or remove reconstruction by producing more bulk like structure. The energy needed for reconstructions is comparable to the bond energies of adsorbate and substrate. Therefore chemisorption can produce surface reconstructions. Chemisorption on semiconductors also induces surface states and surface dipoles, modifying the surface density of states and position of the Fermi level at the surface [22]. Consequently, it affects the electronic properties of semiconductor surfaces such as work function and surface conductivity.

2.3.1 Adsorbate induced work function change

The work function is the minimum amount of energy required to remove an electron from the surface of a condensed phase to a point at infinity. Work function in semiconductors can be described as the contribution from three terms: the electron affinity (χ), band bending (eV_s) and the difference between the Fermi level and the conduction band minimum in the bulk (E_C-E_F) (see Figure 2.5).

$$\Phi = eV_s + \chi + (E_C - E_F) \quad (1)$$

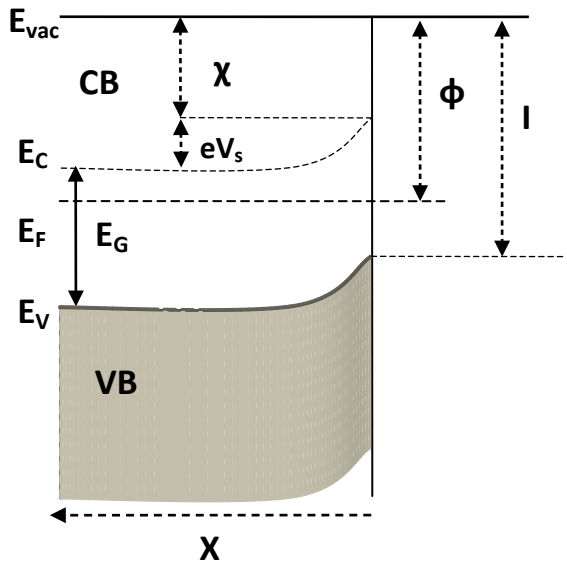

Figure 2.5: Energy diagram of an n type semiconductor. φ is the work Function, electron affinity χ, ionization energy I, band bending eV_s, the conduction band minimum E_C, E_F is the Fermi Energy , E_V is the valence band maximum and E_G is the band gap.

As the electron has to move through the surface region, its energy is influenced by the characteristics of the surface charge layer. Hence, the work function is an extremely sensitive indicator of surface condition and is affected by adsorbed molecules, surface reconstruction, surface charging, surface and bulk contamination, surface orientation in single crystals etc. The change in work function is given by

$$\Delta\Phi = e\Delta V_S + \Delta\Phi_{Dip} + \Delta(E_C - E_F)_{bulk} \quad (2)$$

In the case of weak interactions (physisorption) polarization of the adsorbed atoms may change Φ_{dip}; in case of stronger interactions electron transfer between substrate and adsorbate may induce a dipole layer. This dipole layer together with

inherent dipole moments of adsorbed molecules will constitute Φ_{dip} in chemisorbed systems. Rarely, the bulk term ($E_C - E_F$) is influenced. The quantity ($E_C - E_F$) is a characteristic property of the bulk, and is therefore only changed by molecules diffused into the bulk. Since there is no change in doping for our samples the change in work function (Φ) thus includes contribution only from band bending (eV_s) and change in the dipole moment (Φ_{Dip}) given as

$$\Delta\Phi = e\Delta V_S + \Delta\Phi_{Dip} \quad (3)$$

The contributions from band bending can be determined separately by X-ray photoelectron spectroscopy (XPS) and thus by measuring the change in the work function by e.g. determining the cut-off energy of the secondary electron background in ultraviolet photoelectron spectroscopy (UPS) measurements, enables to determine all contributions to the change in the work function.

2.4 Surface and interface characterization techniques

To completely characterize a surface we need to study the structural, electronic and chemical property of the surface. No single technique can provide all this information; so many different types of techniques are used to analyze surfaces and interfaces. Here we describe some of the characterization techniques used in this work, including Scanning Tunneling Microscopy (STM), X-ray photoelectron spectroscopy (XPS), Auger Electron Spectroscopy (AES), Low Energy Electron Diffraction (LEED) and Temperature Programmed Desorption (TPD).

2.4.1 Scanning probe microscopy

Scanning probe microscopies (SPM) such as scanning tunneling microscopy (STM) and atomic force microscopy (AFM) are extremely useful techniques, providing direct observation of local surface structure at the atomic scale (1 Å) and characterization of surface morphology at larger length scales. In SPM techniques, an atomically sharp probe is used to monitor a probe-surface interaction which is strongly distance-dependent. Tunneling current in STM (decays exponentially with distance from the surface); Van der Waals interactions in AFM (exhibits a power-law decay). Atomic force microscopy can be used in various environments (air, liquid, vacuum) and characterize different types of materials such as metal, semiconductors, soft biological samples, conductive and non-conductive samples.

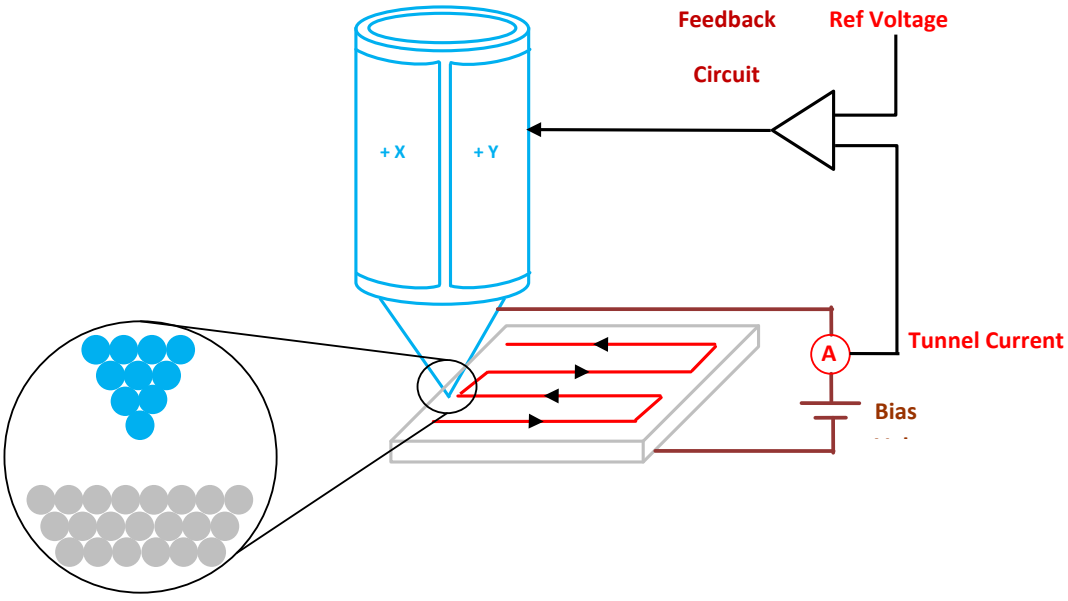

Figure 2.6: Schematic diagram of scanning tunneling microscope

2.4.1.1 Scanning tunneling microscopy

The invention of STM by G. Binning and H. Rohrer started a revolution in the field of microscopy, where one has for the first time an opportunity to observe the physical and chemical process at an atomic/molecular scale [23]. They were awarded the Nobel Prize for their invention in 1986. The basic working principle of STM is illustrated in Figure 2.6.

A sharp metallic tip usually made from a W or Pt-Ir wire is brought in close vicinity (0.1-1 nm) to a conducting sample [24]. If a small voltage is applied between the sample and the tip, the electrons (quantum mechanically) tunnel through the gap and thus an electrical current can be measured. The direction of the tunneling current is defined by the polarity of the applied voltage. The tunneling current is then amplified by the current amplifier, which is compared with a reference value and a corresponding voltage is fed to the z-piezo. The position of the tip in three dimensions is accurately controlled by the piezoelectric tube scanner, which selects the directions and elongations of scan according to the potential applied to corresponding electrodes. The feedback system constantly adjusts the tip-sample distance in real time, so that when the tip is moved to a point (x, y) over the sample, the signal $V_z(x, y)$ fed to the piezo scanner is proportional to the local movement of the sample surface from the ideal plane x, y ($z = 0$). This makes possible to use the values $V_z(x, y)$ to map the surface topography. This is continued in the x and y axes and produces finally the STM image. This type of imaging is called a “constant current mode”, where the reference value of the current is kept constant throughout the experiment and produces the topography of the surface. There is another mode of

operation called “constant height mode”. In this case the tip height is kept constant throughout the measurement and only the variation in the current over the x, y plane is measured. Advantage of this mode over the constant current mode is the stability of the tip but it also has the disadvantage of a risk of tip crash at irregular surfaces or due to thermal drift etc. This makes the constant height mode not practical in most STM set-ups and is mainly of ‘hypothetical’ value.

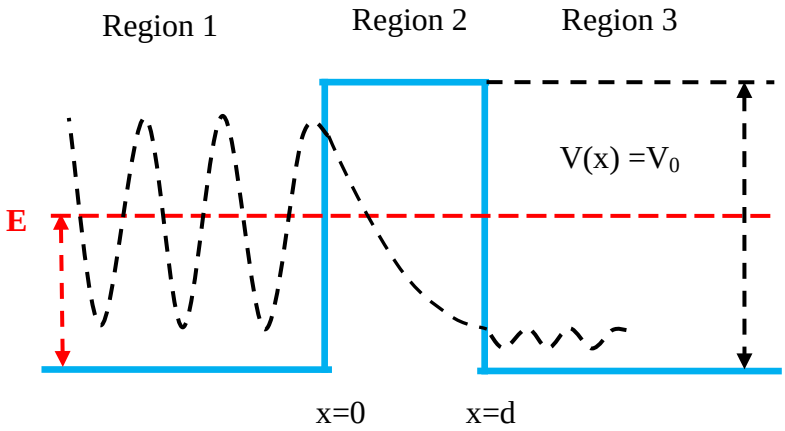

Figure 2.7: Schematic diagram of electron tunneling trough a rectangular barrier: V_0 is the height of the potential barrier, E is the energy of the incident electron, d is the thickness of the barrier. In STM the barrier height V_0 is equal to average of the work function of the sample and the tip, the barrier thickness d is the distance between tip and sample.

The physical basis of STM is quantum mechanical electron tunneling. The probability of electrons tunneling from a sample into the tip across vacuum (barrier) is given by quantum mechanics. In classical physics an electron cannot penetrate into or across a potential barrier if its energy E is smaller than the potential Φ within the barrier. Conversely in quantum mechanics such a particle has a nonzero probability of passing through this potential (see Figure 2.7). When this model is used to describe the STM tunnel junction, the barrier height is of the order of the work function and the barrier

width corresponds to the tip-sample distance in vacuum. So we can write the electron wave function in the vacuum (barrier) as

$$\Psi(x) = \Psi(0)\exp(-\kappa x) \text{ where } \kappa = \sqrt{2m(V_0 - E)/\hbar^2} \quad (4)$$

The height of the barrier can roughly be approximated by the average work-function of sample and tip, $V_o = \frac{1}{2}(\Phi_S + \Phi_T) = \Phi$. If the bias voltage is much smaller than the work-function, the decay length for all tunneling electrons can be approximated as

$\kappa \cong \sqrt{2m\Phi/\hbar^2}$. The probability of finding the electron at distance d is proportional to

$$P \propto |\Psi(d)|^2 = |\Psi(0)|^2 \exp(-2\kappa d) \quad (5)$$

which is very similar to the transmission probability calculated for a rectangular barrier. Thus the probability density of a tunneling particle is exponentially dependent on the width of the barrier.

The tunneling current is then given by

$$I \ \alpha \ \sum_{Ef-eV}^{Ef} |\psi(0)|^2 \exp(-2\kappa d) \quad (6)$$

where E_F is the Fermi energy at the Fermi level.

Therefore resulting tunneling current is also exponentially dependent on the width of the barrier. As the barrier width decreases the probability density on the opposite side of it, and therefore the current through it, increases exponentially. Work functions are typically in the range of 4 to 5 eV. From Equation (6), this would indicate that $\kappa \sim 1$ Å^{-1}. We see that if *d* increases by just 1 Å, the tunneling current decreases by approximately

$(1/e^2)$ or by almost an order of magnitude. Thus the tunneling current is an extremely sensitive measure of the distance between the tip and sample.

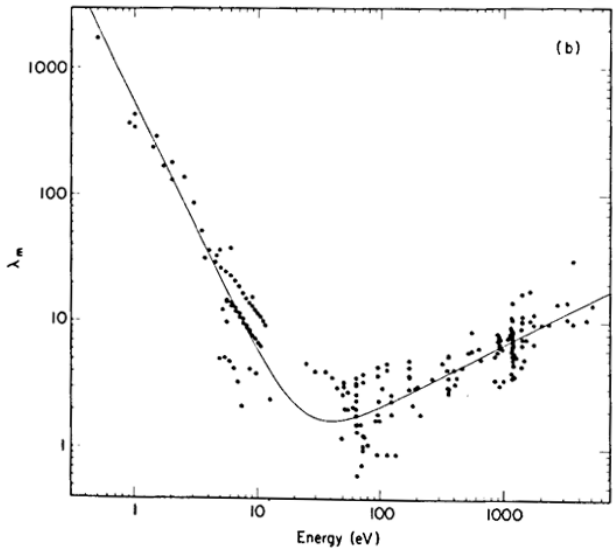

Figure 2.8: The universal curve showing the inelastic mean free path (in Å) of electrons as a function of their kinetic energy. Figure is taken from Ref[27].

2.4.2 Auger electron spectroscopy

Auger Electron Spectroscopy (*Auger spectroscopy* or AES) is used to identify elemental compositions of surfaces by measuring the kinetic energy of Auger electrons. The Auger effect was discovered by Pierre Auger in 1925 while working with X rays and using a Wilson cloud chamber but it was actually developed in the late 1960's, when ultra high vacuum technology was available [25, 26]. The surface sensitivity of AES is due to the low energy of these electrons ($E \leq 1000$ eV). Electrons in this energy range interact with solid matter very strongly; as a result, their inelastic mean free paths within the solid are only a few atomic layers. Figure 2.8 shows the change in inelastic mean free path λ (mean distance between successive inelastic collision) of electrons as a function of their

kinetic energy [27-29]. The solid line describes the theoretical values. The minimum value of λ is around 5 Å when the kinetic energy of the electron is about 50-70 eV. Therefore AES is a suitable technique for surface analysis. It cannot detect hydrogen or helium, but is sensitive to all other elements, being most sensitive to the low atomic number elements.

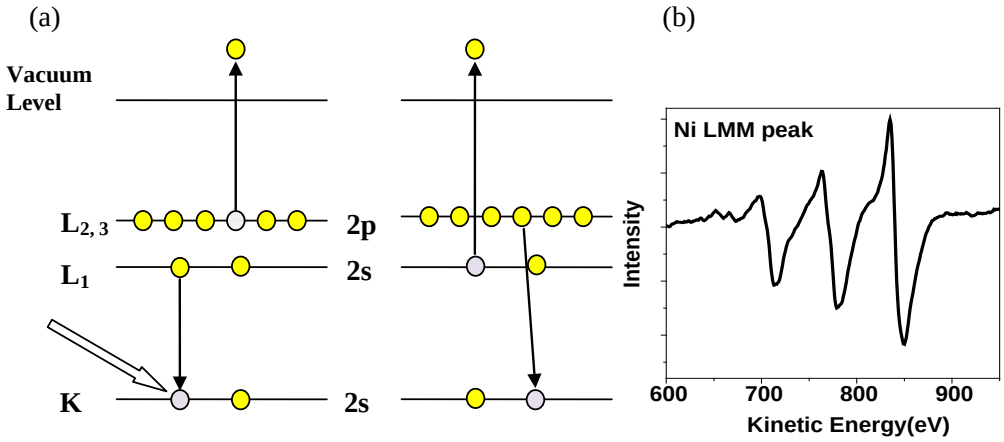

Figure 2.9: (a) Schematic diagram showing KLL transition ($KL_1L_{2,3}$ and $KL_{2,3}L_1$) (b) Auger spectra of Ni LMM transition.

An Auger process is a three step process: (i) atomic ionization by removal of a core electron (ii) relaxation (iii) Auger electron emission. In the example shown in Figure 2.9(a), a hole is created on the K level in the initial ionization step. The hole can be produced by an electron beam (or x-rays) with primary energy greater than the binding energy of the electron in the shell. In practice, typical primary energies of 3 keV are used. The ionized atom is in a highly excited state and rapidly relaxes back to a lower energy state by filling the hole with an electron from an outer level, as L_1 in Figure 2.9(a). The energy released in this process ($E_K - E_{L1}$) is simultaneously transferred to a second electron. Fraction of this energy is used to overcome the binding energy of this second

electron, while the rest is transformed into kinetic energy of the emitted Auger electron. In the Auger process, the final state is a doubly-ionized atom with core holes in the L_1 and $L_{2,3}$ shells (see Figure 2.9(a)). An AES transition is written as ABC, where A indicates the initial level of ionization, B the level where the second electron involved in the transition comes from, and C the level from which the Auger electron is emitted. The Auger transition represented in Figure 2.9(a) is called $KL_1L_{2,3}$. Electrons originating from the valence band, are often denoted by V. More details on the notations and the corresponding electronic configurations can be found in Ref [30]. The KLL series, for example, consists of five components, i.e. KL_1L_1 (1 transitions), $KL_1L_{2,3}$ (2 transitions) and $KL_{2,3}L_{2,3}$ (2 transitions).

Therefore the kinetic energy E_{ABC} of an Auger transition ABC in an atom of atomic number Z is given by

$$E_{ABC} = E_A(Z) - E_B(Z) - E_C^*(Z) - \Phi \qquad (7)$$

where E_I are the binding energies on the 'i' atomic level and Φ is the work function of the sample. The star in E_C* indicates that it is the binding energy of electron in level C in the presence of a hole. Eq. (7) shows that the kinetic energy of an Auger electron is independent of the type of primary beam (i.e. electrons or X-rays) and its energy. For this reason, AES spectra are always plotted on a kinetic energy scale. Since the kinetic energy is only a function of the atomic energy levels, all elements of the periodic table have a unique spectrum. Auger spectra are also often shown in a differentiated form. For example the spectrum shown in Figure 2.9(b) is that of Ni $L_3M_{4,5}M_{4,5}$. This spectrum

was recorded with a lock-in amplifier by modulating the analyzer voltage. Using a lock-in amplifier, results in the direct electronic differentiation of the signal.

2.4.2.1 The Auger line shape

Elements present on the surface can be identified by the Auger peak energies, changes in chemical environment can be deduced from changes in Auger peak positions, intensities, and line shapes. Therefore AES derivative spectra can be used qualitatively to identify the chemical state of elements. Quantitative spectral line shape analysis can provide more information about the electronic structure of different chemical states, but is very difficult because the Auger process involves three electrons.

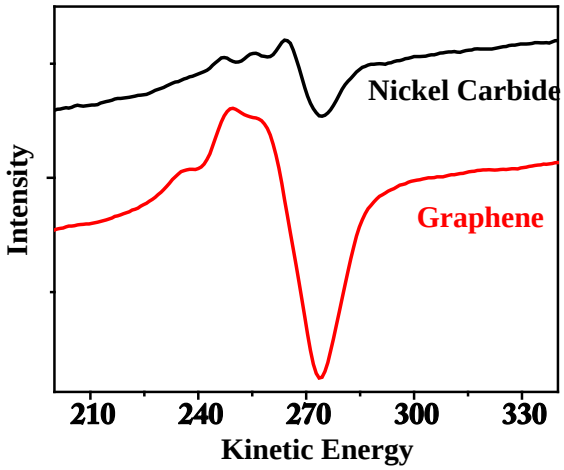

Figure 2.10: Auger spectra showing the C(KVV) peak of carbide and graphene phase on Ni(111).

Auger line shapes may contain information about valence electronic structure if the valence electrons are involved in the Auger transition. If one or both the core holes of an Auger transition lies in the valence band then the spectral line shape of that transition contains information about the local density of states surrounding the excited atom [31].

In fact the shape of a CVV peak, C being a core level, is related to the density of states (DOS) in the valence band. Since the DOS varies from one chemical environment to another, a variation in peak shape is observed. This effect is commonly observed in Auger spectra of non-metallic elements such as C, S, O, N [32]. It has been shown that AES line shape changes with carbon hybridization in the gas phase [33, 34]. The line shape of AES spectra of solid phases can distinguish carbidic and graphitic phases [35]. Figure 2.10 above, shows C(KVV) Auger peak for the carbidic and graphitic phase of carbon on Ni(111) surface [36].The line shape C(KVV) changes from the carbidic to graphitic phase due to difference in valence band. Thus we can use Auger spectroscopy as a probe to distinguish between different chemical states of carbon. We exploit this effect on graphene formation discussed on Ni(111) discussed in Chapter 4.

2.4.3 Photoemission spectroscopy

Photoemission spectroscopy (PES) or photoelectron spectroscopy analyzes the kinetic energy distribution of the emitted photoelectrons to study the composition, chemical state, and electronic structure in the surface region of a sample. PES has been used in various fields like surface chemistry or material science, and has significantly contributed to the understanding of fundamental principles in solid state physics. PES can be subdivided in X-ray photoelectron spectroscopy (XPS) and Ultraviolet Photoemission Spectroscopy (UPS). In XPS, X-rays (with photon energy of 200-2000 eV) are used to examine the core levels while in UPS UV radiation (with photon energy of 10-45 eV) is used to study the valence energy levels.

2.4.3.1 X-ray photoelectron spectroscopy

X-ray photoelectron spectroscopy (XPS) involving core level electrons are used to analyze the composition and chemical state of surfaces. Shifts in the core levels of adsorbate and substrate atoms provide information about changes in chemical character like oxidation states. XPS was developed in the 1960s by K. Siegbahn and his research group at the University of Uppsala, Sweden. K. Siegbahn was later awarded the Nobel Prize for Physics in 1981 for his work in XPS. The principle behind the XPS technique is the photoelectric effect, first observed by Hertz in 1887 which was later explained by Einstein in 1905. In the photoelectric effect, when the sample is irradiated with photons electrons are ejected from the surface. The kinetic energy (KE) of the ejected photoelectron is determined by the energy of the x-ray radiation, *hv*, the electron binding energy, E_B, and the work function of the sample Φs as $KE = hv - E_B - \Phi s$.

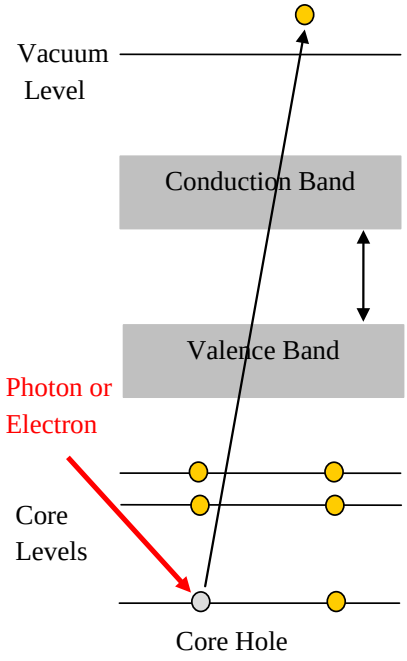

Figure 2.11: Schematic Diagram showing photoemission process.

During the measurement, the sample is in electrically contact with the spectrometer. Then, their Fermi level is in equilibrium. The work function of the sample and the analyzer is Φs and Φ_A, respectively. The difference in work function between the sample and analyzer gives rise to a contact potential $\Delta\Phi = \Phi_S - \Phi_A$. So the energy of the photoelectrons detected by the electron energy analyzer is now given by

$$KE = h\upsilon - E_B - \Phi_S - (\Phi_A - \Phi_S) = h\upsilon - E_B - \Phi_A \quad (8)$$

Therefore, the detected kinetic energy of the photoelectrons is independent of the work function of the sample and only depends on the analyzer work function, which is calibrated and remains constant for different experiments/samples.

Photoemission occurs in a three step process. First, the incident photon is absorbed by an electron. Second, the photoelectron travels to the surface and third, escapes the solid into vacuum. During its travel to the surface most of the ejected photoelectrons suffer inelastic collisions and lose their kinetic energy. So the photoelectron spectrum is composed of two types of electrons-primary electrons which did not suffer any inelastic collisions and the secondary electrons. The secondary electrons give rise to a continuous background which is superimposed on the primary electron spectrum. The different peaks in a photoelectron spectrum reflect the electronic structure of the sample. Every element has a unique set of binding energies and, therefore, an XPS spectrum gives information about the chemical composition of the sample. A typical XPS spectrum is shown in Figure 2.12.

The XPS spectrum has peaks from photoemission processes and Auger processes. The most intense peaks are from photoelectrons like Ni 2p peaks. Photoelectrons emitted

from orbitals with non zero orbital angular momentum (p,d,f orbitals) show spin orbit splitting in the photoemission peaks e.g. Ni 2p shows multiplet splitting, into Ni $2p_{3/2}$ and Ni $2p_{½}$ peaks. The magnitude of the spin orbit splitting is characteristic feature of the element. The "Ni LMM" structure results from the excitation of Auger electron emission. Auger electrons are emitted with a kinetic energy that is independent of the X-ray energy, so in cases where Auger peaks are superimposed on photoelectron peaks, the Auger peaks can be displaced elsewhere on the binding energy scale by changing the X-ray photon energy. In addition to these features there are X-ray satellite and X-ray ghost features. Emission from non monochromatic X-ray sources produces *satellite peaks* in the XPS spectrum appearing at lower binding energy with respect to the corresponding photoemission peaks. The stepped background of XPS spectra is due to the electrons from inelastically scattered photoelectrons at higher binding energy.

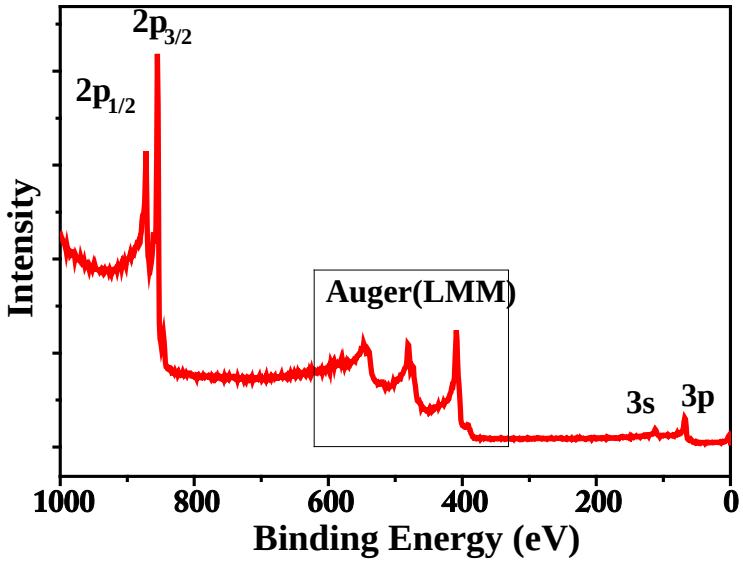

Figure 2.12: XPS spectrum of Nickel sample using Mg Kα X-ray line (1253.6 eV) for excitation.

Bulk and surface sensitive experimental conditions can be achieved by varying the photon energy. X-rays penetrate deeply into the substrate before being absorbed, so the emitted photoelectrons have to travel some distance to escape from the solid surface. The distance photoelectrons can travel without any losses due to scattering depend on its kinetic energy (see Figure 2.8). The escape depth is the product of the inelastic mean free path λ and the cosine of the emission angle θ, D=λ cos(θ). Therefore the escape depth of the photoelectrons depends on their kinetic energy, which can be tuned by tuning the photon energy. Decreasing the kinetic energy of the photoelectrons therefore makes it more surface sensitive. Therefore using photons with energies between 50-1000 eV we can probe the near surface region. This is also known as soft x-ray photoelectron spectroscopy (SXPS). The core level photoemission lines contain a wealth of information on the chemical and electronic environment of the atoms or energy losses of the photoemitted electrons to collective excitations such as plasmons. Some of the information one can extract from peak positions is discussed next.

2.4.3.2 Core level shifts

The measured binding energy of an electron is the energy difference between the initial state (atom with n electrons) and the final state (atom with n-1 electrons and the photoelectron).

$$E_b = E_b(n-1) - E_b(n) \approx -\varepsilon_{HF}^{atom} \quad (9)$$

where ε_{HF}^{atom} is the orbital energy of the ejected electron. This is also known as Koopmans theorem [37]. The theorem is an approximation as it assumes that the electrons orbitals freeze during photoemission ignoring any relaxation of electrons within

the atom. Actually the orbitals are not frozen during photoemission but the electrons relax by rearranging themselves or screening. If this intra atomic relaxation energy is taken into account then the binding energy of the photoelectron is given as

$$E_b = -\varepsilon_{HF}^{atom} - R_a \quad (10)$$

A binding energy of a core-level electron in an atom depends also on surroundings of atoms. Therefore the binding energy of an electron in atom 'j' in the solid is given as

$$E_b(j) = -\varepsilon_{HF}^{atom} + V_a(j) - R_a(j) + V_{ea}(j) - R_{ea}(j) - \Phi \quad (11)$$

where $V_a(j)$ is the change in energy due to valence electrons that represents the change in the valence charge due to bonding

$R_a(j)$ are intraatomic relaxation energies that represents the rearrangement of the electron density within the atom

$V_{ea}(j)$ are extratomic Madelung energy that represents the change in orbital energy when the atom is inserted in the solid

$R_{ea}(j)$ are extratomic relaxation energies that represent the rearrangement of electron density surrounding the ionized atom

Φ is the work function of the material

The main use of XPS is the accurate determination of binding energies. Shifts in binding energy give valuable information about the chemical state of the element and their local environment [38]. Therefore the change in binding energy is given as

$$\Delta E_b \approx \Delta V_a + \Delta V_{ea} - \Delta R_{ea} \tag{12}$$

$$= \underbrace{\frac{\Delta q}{r} + \alpha \frac{\Delta q}{r}}_{Initial\ State\ Effect} - \underbrace{\Delta R_{ea}}_{Final\ State\ Effect} \tag{13}$$

The intraatomic potential $\Delta V_a = \frac{\Delta q}{r}$ is an initial state effect which is proportional to the displacement or transfer of charge from the valence electrons, determined by the electronegativities of the atoms involved. The extratomic Madelung potential $\Delta V_{ea} = \alpha \frac{\Delta q}{r}$ (α is the Madelung Constant) is an initial state effect that shows the presence of neighboring atoms or ions. The extra atomic relaxation energy(ΔR_{ea}) is a final state effect determined by the polarizability of the neighboring atoms.

Shift in the binding energy of a core level electron of an element due to change in valence charge is called chemical shift. If an atom loses charge to more electronegative neighbors, its core electrons will experience a net increase in Coulombic attraction, and their binding energies will go up. Similarly, if an atom becomes more negatively charged, then its core electrons will have lower binding energies. The interaction between core electrons and the nucleus can be reduced by the screening of the nuclear charge by all the other electrons in the atom. The shift in the binding energy of the surface atoms with respect to the bulk atoms are also known as surface core level shifts. These shifts can be a consequence of initial state effects and/or final state effects. In metals the reduced coordination at the surface decreases the binding energy of the surface atoms while in ionic solids the reduced coordination changes the Madelung potential experienced by the surface ions which changes the binding energies of the surface ions [39-41].

In ionic solids the Madelung potential (initial state effect) plays an important role in surface core level binding energy shifts. The Madelung energy of ions at the surfaces/interfaces are different from the ions in the bulk [42]. The reduced coordination of atoms on the surfaces reduces the surface electrostatic potential or the surface Madelung potential. The reduced value of Madelung potential decreases (increases) the cation (anion) binding energy compared to a cation (anion) in the bulk. This causes shift in the surface electronic levels compared with the bulk. As the Madelung energy depends on the local coordination of the surface atoms, different shifts may be expected for surface atoms at step edges compared to terraces. The core level binding energies can be resolved into surface and bulk core level components in XPS spectra collected from the sample. Therefore using high resolution, surface sensitive core level spectroscopy can provide valuable information about the Madelung potential of the surface atoms and consequently about the surface structure and composition.

2.4.4 Low energy electron diffraction

Low-energy electron diffraction (LEED) is a well established and versatile technique for characterizing surface structure. LEED uses diffraction effects of electrons whose kinetic energies are in the range from about 20eV to 200eV. The wavelength of low energy electrons is about 1-2Å which is of the order of or less than the interatomic distances and thus satisfies the diffraction condition. Also the mean free path of these low energy electrons is very short (see Figure 2.8), which limits the elastic scattering within a few atomic layers of the sample. Therefore LEED provides information about the 2D atomic structure of the sample surface. The first LEED experiment was carried

out by Davisson & Germer in 1927, demonstrating the wave nature of the electron [43]. Figure 2.13 shows a typical experimental setup that is used to obtain diffraction patterns.

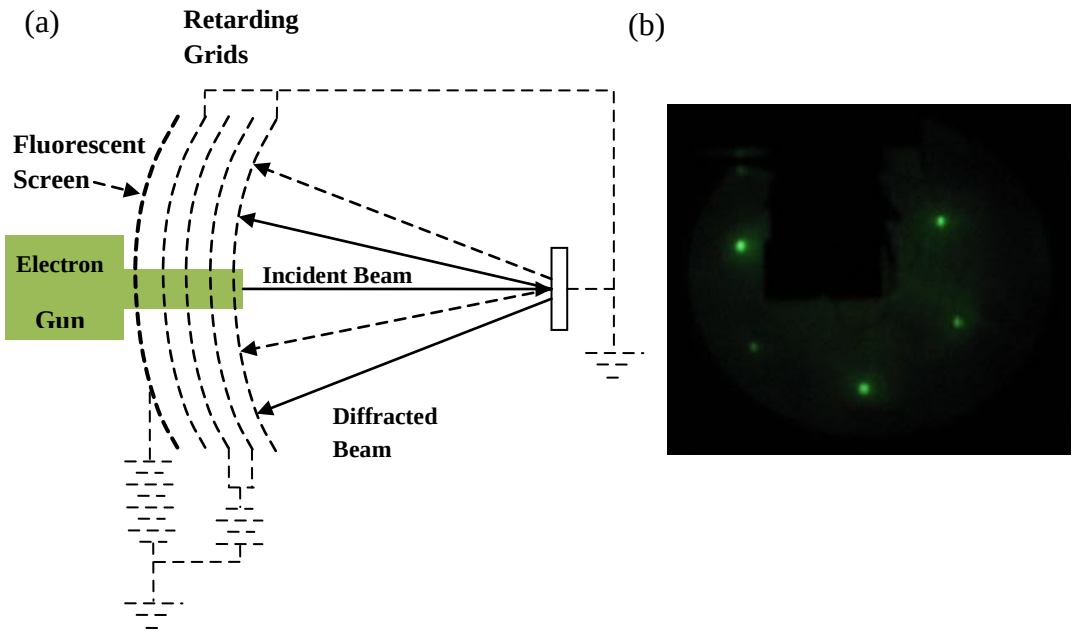

Figure 2.13: (a) Schematic Diagram of LEED experimental setup (b) LEED pattern of Ni(111).

LEED instrumentation consists of an electron gun, retarding grids, and a fluorescent screen which permits direct viewing of the diffraction pattern produced by a crystal surface [44]. The electrons emitted from the gun are accelerated by a variable voltage and are incident perpendicular on a crystalline sample. The incident electrons are then back-scattered and fall on the grid at the same side as the gun. The elastically scattered electrons form a diffraction pattern and inelastically scattered electrons are filtered by the retarding grids placed in front of the fluorescent screen. The sample and the first grid are grounded, producing a field-free zone for the low energy electrons to travel without deflections. The negatively biased second and third grids remove the inelastically scattered electrons. The fourth grid is also grounded which shields the other

grids from the field of the fluorescent screen which is at high voltage. The diffracted beams excite fluorescence in the screen and thus the bright LEED diffraction spots are seen. The LEED pattern characterizes the two-dimensional symmetry of the surface crystal lattice as described next.

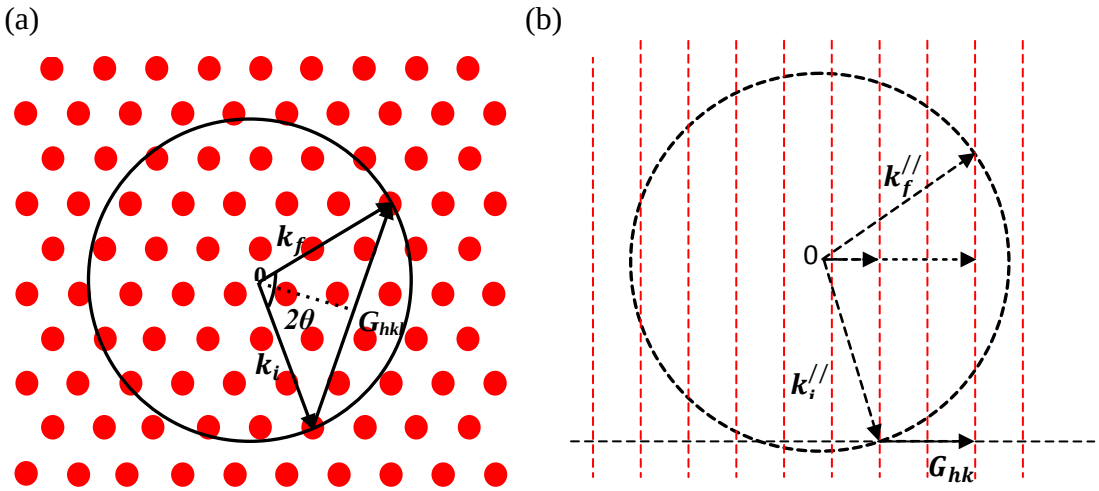

Figure 2.14: Ewald sphere construction for 3D lattice (a) and 2D lattice (b) respectively.

2.4.4.1 Diffraction from 2D crystal

The Laue Condition for diffraction is given as

$$\boldsymbol{k_f - k_i = G_{hkl}} \tag{14}$$

where $\boldsymbol{k_i}$ is the incidence lattice vector ($k_i = 2\pi/\lambda_i$), $\boldsymbol{k_f}$ is the scattered wave vector ($k_f = 2\pi/\lambda_f$) and $\mathbf{G_{hkl}}$ is the reciprocal lattice vector. As the scattering is elastic we get

$$|\boldsymbol{k_f}| = |\boldsymbol{k_i}| \tag{15}$$

Ewald Sphere Construction is a way to represent the Laue condition of diffraction schematically. A sphere of radius k=$2\pi/\lambda$ is constructed in the reciprocal lattice. The incident wave vector $\boldsymbol{k}_i$ terminates at a reciprocal lattice point. Reciprocal lattice points lying on the surface of the Ewald sphere satisfies both the conditions (Eqn 14 and 15) for diffraction.

The interplanar distance in reciprocal space between (hkl) plane can be calculated as

$$|\boldsymbol{G}_{\boldsymbol{hkl}}| = \frac{2\pi}{a}\sqrt{h^2 + k^2 + l^2} = \frac{2\pi}{d} \tag{16}$$

where *a* is the lattice constant and *d* is the interplanar distance in real space. In this case the diffraction angle is half of the angle between the incident and scattered wave vector. We can calculate

$$\sin\theta = \frac{|\boldsymbol{G}_{\boldsymbol{hkl}}|/2}{k_i} = \frac{\frac{2\pi}{d}}{2(\frac{2\pi}{\lambda})} = \frac{\lambda}{2d} \tag{17}$$

which is equivalent to Bragg's Diffraction condition. In a 2D crystal the crystal periodicity is disrupted in the direction normal to the surface so we write eqn (14) as

$$\boldsymbol{k}_{\boldsymbol{f}}^{//} - \boldsymbol{k}_{\boldsymbol{i}}^{//} = \boldsymbol{G}_{\boldsymbol{hk}} \tag{18}$$

The wave vector component perpendicular to the surface is not conserved in this case. The Ewald construction for a 2D lattice is shown in Figure 2.14. The 2D lattice can be thought of as a 3D lattice with infinite periodicity in the normal direction which will give rise to reciprocal lattice points infinitely dense, forming rods. Therefore the reciprocal lattice rods perpendicular to the surface can be attributed to every 2D reciprocal lattice

point. The intersection of the rods with the Ewald sphere defines the scattered wave vectors $\boldsymbol{k_f}$ for the diffracted beam (see Figure 2.14(b)). We can imagine the fluorescent screen being the Ewald sphere and the diffraction spots where the reciprocal rod intersects the Ewald sphere. Therefore the number of diffraction spots observed in a LEED pattern depends on the size of the Ewald sphere. Increasing the electron energy increases the size of Ewald sphere and thus more diffraction spots are visible. Therefore the diffraction spots will move away or closer to the center of the screen as the energy of the incident electrons is decreased or increased. The intensity of the spots also changes as the electron energy is changed. Detailed analysis of the intensity changes and function of the energy of the electrons can provide more information about the surface structure. Figure 2.13(b) shows the LEED pattern of hexagonal Ni(111) surface.

2.4.5 Temperature programmed desorption

Temperature-programmed desorption (TPD) is an important method for the determination of kinetic and thermodynamic parameters of desorption processes or decomposition reactions. In TPD, gaseous species are adsorbed on the sample at low temperatures and then a temperature ramp is applied to the sample. As the sample is heated the thermal energy needed to break surface bonds becomes available and desorption is observed. The rate of desorption is measured by monitoring the amount of desorbing species as a function of temperature. The desorption temperature of the gaseous species indicates the strength of surface binding and has been used to infer the presence of different adsorption sites at the surface. The total area under a peak is proportional to the amount originally adsorbed, i.e. proportional to the surface coverage.

Analysis of desorption traces is based on treating the desorption process as a kinetic phenomenon. The rate of desorption is given by the Arrhenius or Polyani Wigner equation as

$$r_{des} = -\frac{d\theta}{dT} = \upsilon^n \theta^n \exp\left(-\frac{E_d}{k_B T}\right) \quad (19)$$

where, ν^n is the pre-exponential frequency factor, E_d is the activation energy of desorption, k_B is the Boltzmann constant and θ is the fractional coverage expressed in units of monolayers (MLs). During desorption, the temperature of the sample surface is controlled in a linear fashion, (i.e, $T = T_0 + \beta t$), T_0 is the initial sample temperature and β is the heating rate $dT = \beta dt$. Since the temperature of the sample is varied linearly with time we rewrite this equation as

$$r_{des} = -\frac{d\theta}{dT} = -\frac{1}{\beta}\frac{d\theta}{dt} = \frac{\upsilon^n \theta^n}{\beta} \exp\left(-\frac{E_d}{k_B T}\right) \quad (20)$$

The general shape of the $r_{des}(T)$ with temperature depends on the exponential term as shown in eqn 19. At low temperatures the exponential term is negligible so desorption rate is negligible, but at high temperature the desorption rate increases rapidly following the increase in the exponential term. However the coverage (θ) also decreases with increased desorption which slows down the desorption rate until it becomes zero. Therefore the desorption rate is characterized by a peak at a certain temperature. This desorption peak temperature is related to the activation energy, initial coverage, heating rate and order of desorption. Redhead derived a relation between activation energy and desorption temperature assuming that for first order desorption E_d and υ is independent of coverage [28].

$$E_d = k_B T(ln\frac{\upsilon_1 T_m}{\beta} - 3.64) \quad (21)$$

The shape of desorption curves as a function of coverage provides information about the order of desorption. The various adsorption and desorption parameters, such as: number and population of various desorbing phases, activation energy of desorption (E_d), the order of desorption (n) and the pre-exponential frequency factor for the desorption (*υ),* can be determined by the analysis of the desorption spectrum. There are different methods developed to analyze the desorption spectrum such as Redhead analysis, leading edge analysis etc.[45].

A typical desorption spectrum is shown in Figure 2.15. It shows the desorption of CO from Ni(111) surface for saturation coverage. The two desorption peaks at 340K and 410K are for two different binding sites with different activation energy. The low temperature peak and high temperature peak corresponds to CO adsorbed at top sites and bridge sites respectively. Adsorption of CO on transition metal surfaces have been studied extensively [46]. It is known for clean Ni(111) substrates, that CO adsorb at top, bridge or hollow sites depending on CO coverage. At high coverages, CO is more favorable to occupy the bridge sites and on top sites. Bonding at the bridge sites is much stronger than on-top sites so the desorption from these sites occur at higher temperature and CO from top sites are desorbed first. In our studies of graphene growth on Ni(111) we use the adsorption of CO on Ni as a probe for detecting the presence of Ni-sites. The shape and intensity of the CO desorption traces from such samples give information of the kind and amount of Ni-sites present at the surface. This use of TPD is described in more detail chapter 4.

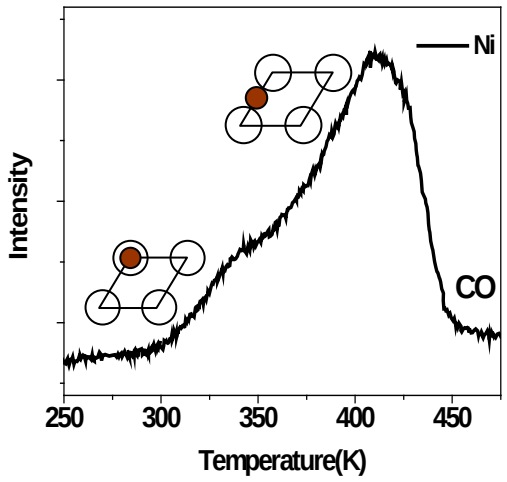

Figure 2.15: Desorption spectra from clean Ni(111) sample. The high and low temperature peak corresponds to CO desorption from bridge and top sites respectively.

The principal components of the TPD system consist of the sample heater and quadrupole mass spectrometer (QMS). TPD is carried out by heating the sample with a linear rate in front of a multiplexing QMS. The sample is in thermal contact with a liquid N_2 filled cold finger via two copper conductors, enabling cooling to about 120 K. The sample can be resistively heated to about 1200 K. The temperature is measured by a type K thermocouple attached directly to a metallic sample or glued on the surface of oxide samples. A schematic of the TPD system representing the main functional blocks is given in Figure 2.16 [47, 48].

For implementing TPD in the experiments described below I wrote a program in LABVIEW for data acquisition and communicating with instruments. A data acquisition (DAQ) board, installed on the computer (National Instruments PCI-6036) is used for digital-to-analog conversion and vice versa. Through the DAQ board the computer

controls the power supply that feeds the heating current to the sample and also reads the voltage output of the thermocouple attached to the sample. The Quadrupole Mass Spectrometer (UTI 100C) receives the control input from the DAQ board as well, in the form of an analog signal (*m*/*e* setting). The desorption flux reading recorded by the QMS is then returned to the computer. A flowchart of the program for TPD is shown in Appendix 1.

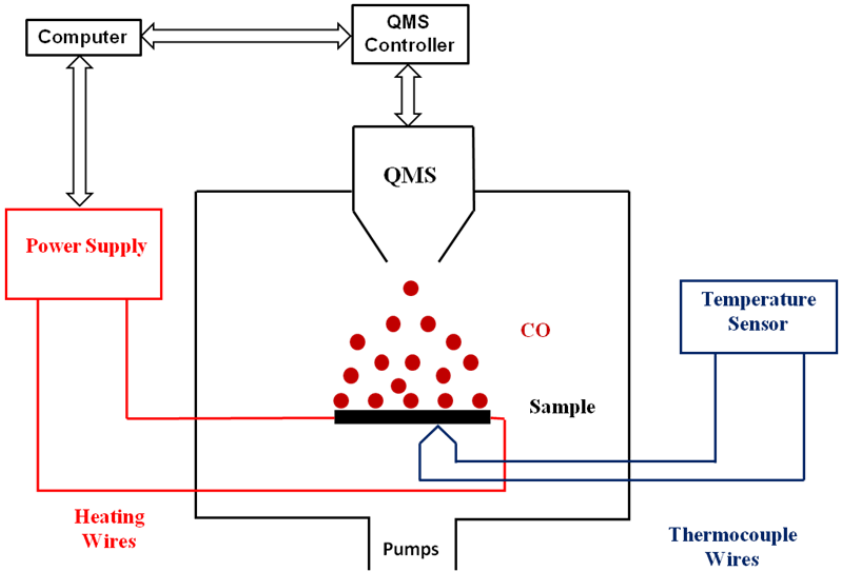

Figure 2.16: Schematic Diagram of experimental setup of Temperature Programmed Desorption apparatus with the control electronics.

2.5. Experimental apparatus

The experiments were performed at the Surface & Nanophysics Lab, Department of Physics, University of South Florida and at the U12a soft x-ray beamline, National Synchrotron Light Source (NSLS), Brookhaven National Laboratory. The experiments were conducted in three separate ultra high vacuum (UHV) chambers. The base pressure in all the UHV chambers were in the low 10^{-10} Torr range. To achieve UHV a

combination of different pumps were used. All the UHV chambers were equipped with four main types of pumps - a rotary-vane pump, a turbomolecular pump (turbo pump), ion pumps and titanium sublimation pump (TSP).

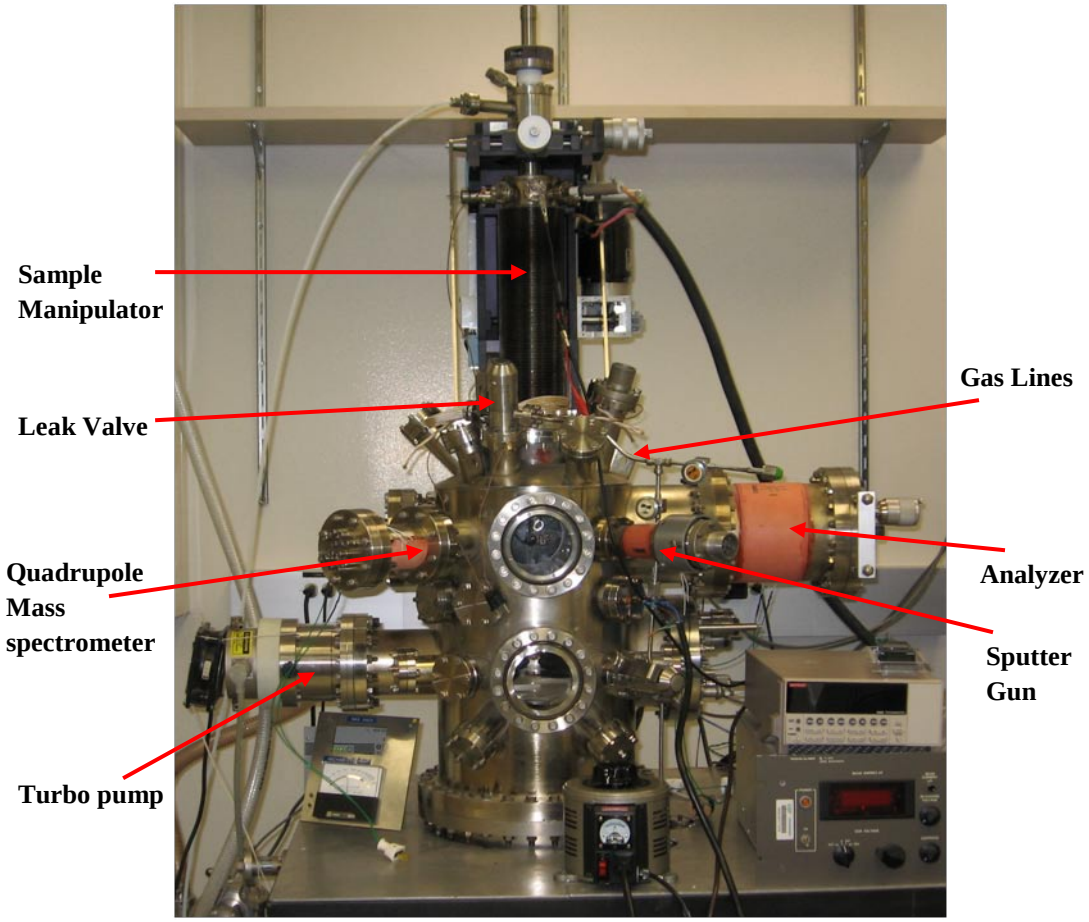

Figure 2.17: Ultra high vacuum chamber.

Figure 2.17 shows one of the UHV chamber used in this study. The UHV chamber is equipped with an electron gun housed within a cylindrical mirror analyzer for AES measurements, X-ray source for XPS measurements, a quadrupole mass spectrometer (QMS) for TPD measurements, low energy electron diffraction (LEED)

optics, low energy ion gun for sputter-cleaning samples, and mini e-beam evaporator for metal depositions. The components are described briefly below.

2.5.1 Electron Gun for AES

The electron gun generates a primary electron beam of energy 1-5 keV. The electron gun, either be a thermionic or on a field emitter source. In a simple thermionic source, a tungsten filament is heated by current and when the electrons get sufficient energy to overcome the work function of the material electrons are emitted. In a field emission source, an electric field is applied to the filament and an electrode which reduces the barrier for electron tunneling out of the filament into vacuum. In this case it is a thermionic electron source. The electron gun for AES is housed in the cylindrical mirror analyzer.

2.5.2 X-ray Source for XPS

A lot of different X-ray sources are used in XPS studies like the standard lab X-ray source with twin Al/Mg anode and synchrotron light sources. In our lab we have a PHI Model 04-500 X-ray source with Al/Mg anode. Electrons produced from the filament (cathode) bombard the anode, which is kept at very high potential ~ 15 kV. Electrons ionize the anode producing core holes which then relaxes by emitting X-rays. The characteristic X-ray produced by Al and Mg anode has line energies/line widths of 1486.6 eV/0.85 eV and 1253.6 eV/0.70 eV respectively. In synchrotron light source radiation (X-ray, UV and IR) is emitted from electrons moving at relativistic velocities when they are accelerated by a magnet. A charged particle constrained to move in curved path by bending magnets, experience centripetal acceleration which produces radiation.

Advantage of synchrotron radiation over lab source is high intensity and ability to tune photon energies. The synchrotron radiation has a wide distribution of frequencies and using a mochoromator can choose a single frequency thereby tuning the photon energy. The intensity of this radiation can be ~ 10 times greater than a lab source. For more information on synchrotron light sources see Ref [49, 50].

2.5.3 Cylindrical mirror analyzer

In both AES and XPS an energy analyzer is used to measure the kinetic energy of the electrons. The most common types of analyzers are Cylindrical mirror analyzer (CMA) and Concentric Hemispherical Analyzer (CHA). We use a PHI Model 15-255G Precision Energy analyzer which is a double pass cylindrical mirror analyzer with retarding grids and an integrated electron gun for Auger surface analysis. A CMA consists of two coaxial metal cylinders (outer and inner cylinder) which are kept at different potentials so that an electric field exists between them. The outer cylinder potential is at negative potential compared to the inner cylinder. For a given negative potential applied to the outer cylinder, electrons with certain kinetic energy are able to pass through the output aperture and reach the detector while the rest are deflected in the region between the two cylinders. Therefore by varying the potential applied to the outer cylinder we can a energy distribution of the electrons passing through it. The voltages on the inner and outer cylinder are different for XPS and AES measurements. A channeltron is usually used a as an electron detector.

2.5.4 Quadrupole Mass spectrometer

A quadrupole mass spectrometer is a versatile instrument which is used in wide range of applications like surface studies, gas and liquid chromatography etc. In our case the QMS is mostly used for residual gas analysis, detecting leaks in vacuum chamber and TPD measurements. We use a UTI 100C Precision Mass analyzer able to scan from 0-300 amu. The analyzer has three main components, the ion source, the quadrupole mass filter and the detector (electron multiplier/Faraday Cup). The gas molecules are ionized with electrons from the filaments which are then injected in the quadrupole mass filter. The ionized molecules are filtered according to their mass/charge ratio (m/e) in a high frequency electric field produced by four rods and then they are detected with an ion detector. The detected ions are converted into current which is then plotted as a function of m/e ratio for different ions. For more information quadrupole mass spectrometry see Ref [51].

2.5.5 Sputter Gun

The sputter gun produces a beam of energetic inert gas ions for sputtering surfaces of materials. Inert gas like Ar is leaked into the chamber which is then ionized by electrons emitted from the filament (cathode).These ions are then accelerated towards the anode (kept at high positive potential) and focused by a lens system to produce a beam of high energy Ar ions at the sample surface. The energy of the ions incident on the sample is equal to the positive potential applied at the anode.

2.5.6 E-beam evaporator

For e beam evaporation an electron beam is used to heat the target material to very high temperatures until it evaporates atoms from the source material. These evaporated atoms have only thermal energy and can be condensed on the substrate that is positioned in front of the evaporator. The source-material to be evaporated is either put in a refractory-metal crucible or evaporated directly from a rod is used. When the tungsten filament surrounding the rod or crucible is heated by high current (6-7A) it starts emitting electrons. A positive high voltage (1-3 kV) applied to the rod or crucible attracts the electrons of the filament and the source material is heated by the electron impact. Due to the very high electron density on the tip of the rod or to the crucible temperatures of >3100K can be achieved. The filament and source material is contained in a water cooled jacket that keeps the surrounding vacuum chamber from heating up allowing to maintaining a low pressure (~10^{-9} Torr) in the vacuum chamber during evaporation and film growth. We use a Tectra e flux E beam evaporator which is also provided with a flux monitor and a shutter. The flux monitor detects ionized atoms within the vapor of the evaporated source material. This can be used to calibrate the deposition rate. Since the fraction of ionized to neutral atoms is different for every source material calibrations have to be performed for every new material.

The UHV chamber also has several precision leak valves for dosing of gases like COand C_2H_4. The sample manipulator allows polar rotational motion and translational motion in the XYZ direction of the sample. The sample can be either mounted on a Ta sample plate and then spotwelded to the sample holder with Ta wires or directly

spotwelded to the sample holder with Ta wires. The sample is heated resistively with Ta heating wires. The sample holder is connected to a cold finger which can be cooled down to -140°C by addition of liquid nitrogen. The temperature is monitored by a K-type thermocouple that is spot-welded to the sample.

The STM measurements were performed in a commercial Omicron-VT STM. More information about the STM can be found at http://www.omicron.de/products/spm/variable_temperature_instruments/vt_stm/media/vt_stm_1.pdf (website accesses on 08/30/10) Photoemission studies were performed at the U12a beamline at NSLS. This beamline is optimized for soft X-ray photoemission spectroscopy with a photon energy range between 1 and 0.1 keV which enables acquisition of both core-level and valence band photoemission spectra. More information about the UHV chamber at U12a beamline at NSLS can be found at http://www.nsls.bnl.gov/beamlines/beamline.asp?blid=U12A (website accessed on 08/30/10).

2.6 Sample preparation

Clean surfaces are prepared by sputtering and annealing. Contaminants are sputtered off from the surface with Ar ions. After sputtering the surface becomes rough so annealing to high temperatures are required to restore the surface crystallinity and to remove ion-implanted Ar atoms from the sample. In practice several cycles of sputtering and annealing are required to prepare well ordered clean surfaces.

We have worked with ZnO and Ni (111) samples. The ZnO samples were cleaned by cycles of 1 keV Ar ion sputtering and annealing to 900 K. The surface cleanliness was

checked by SXPS. A two side polished 0.5 mm thick ZnO single crystal with polar surface orientation from Scientific Production Co. Goodwill was used. The crystal was broken in half and both halves were mounted on a 0.5 mm thick tantalum plate. One half exposed the Zn terminated side and the other half exposed the O-terminated side. This way both orientations could be measured under identical conditions. The ZnO surface was passivated with (sub) monolayer sulfide by backfilling of the UHV chamber with H_2S with the sample at 600 K. The H_2S exposure was measured with an ion gauge.

Ni(111) sample was also cleaned similarly. Before each experiment the Ni crystal was cleaned by cycles of 0.5 keV Ar^+ ion sputtering followed by annealing to 800 °C. Then, the sample was annealed in 10^{-6} Torr O_2 for 10 min at 500 °C to burn off any remaining surface carbon, and flashed at 800 °C in UHV. The cleanliness of the surface was checked by Auger electron spectroscopy (AES) or scanning tunneling microscopy (STM). Carbide or graphene was grown on the clean Ni(111) surface by exposure of the sample to 10^{-5} Torr ethylene for 4 min at the temperature cited in the text. In additional experiments, Ni and Cu were deposited on the sample containing graphene and/or carbide. Ni deposition was done by sublimation of a high purity 2 mm-diameter Ni-rod in a water-cooled mini e-beam evaporator. For Cu-deposition, high purity Cu wire was wrapped around a tungsten filament that was heated by an electrical current.

2.7 References

1. Tasker, P.W., *Stability of Ionic-Crystal Surfaces.* Journal of Physics C-Solid State Physics, 1979. **12**(22): p. 4977-4984.

2. Tasker, P.W., *Surface-Properties of Uranium-Dioxide.* Surface Science, 1979. **87**(2): p. 315-324.

3. Cox, P.A., F.W.H. Dean, and A.A. Williams, *Electrostatic Models for Surfaces of Ionic-Crystals.* Vacuum, 1983. **33**(10-1): p. 839-841.

4. Noguera, C., *Polar oxide surfaces.* Journal of Physics-Condensed Matter, 2000. **12**(31): p. R367-R410.

5. Noguera, C., *Physics and chemistry at oxide surfaces*. 1996, Cambridge [England] ; New York: Cambridge University Press. xv, 223 p.

6. Wright, K., et al., *Simulation of the structure and stability of sphalerite (ZnS) surfaces.* American Mineralogist, 1998. **83**(1-2): p. 141-146.

7. Moore, D., et al., *Wurtzite ZnS nanosaws produced by polar surfaces.* Chemical Physics Letters, 2004. **385**(1-2): p. 8-11.

8. Goniakowski, J., F. Finocchi, and C. Noguera, *Polarity of oxide surfaces and nanostructures.* Reports on Progress in Physics, 2008. **71**(1): p. 016501-54.

9. Barbier, A., et al., *Stability and stoichiometry of (polar) oxide surfaces for varying oxygen chemical potential.* Journal of Physics-Condensed Matter, 2008. **20**(18): p. -.

10. Kresse, G., O. Dulub, and U. Diebold, *Competing stabilization mechanism for the polar ZnO(0001)-Zn surface.* Physical Review B, 2003. **68**(24): p. 245409-23.

11. Dulub, O., U. Diebold, and G. Kresse, *Novel stabilization mechanism on polar surfaces: ZnO(0001)-Zn.* Physical Review Letters, 2003. **90**(1): p. 016102-05.

12. Dulub, O., L.A. Boatner, and U. Diebold, *STM study of the geometric and electronic structure of ZnO(0001)-Zn, (000(1)over-bar)-O, (10(1)over-bar0), and (11(2)over-bar0) surfaces.* Surface Science, 2002. **519**(3): p. 201-217.

13. Meyer, B. and D. Marx, *Density-functional study of the structure and stability of ZnO surfaces.* Physical Review B, 2003. **67**(3): p. 035403-13.

14. Lahiri, J., S. Senanayake, and M. Batzill, *Soft x-ray photoemission of clean and sulfur-covered polar ZnO surfaces: A view of the stabilization of polar oxide surfaces.* Physical Review B, 2008. **78**(15): p. 155414-23.

15. Meyer, B., *First-principles study of the polar O-terminated ZnO surface in thermodynamic equilibrium with oxygen and hydrogen.* Physical Review B, 2004. **69**(4): p. 045416-25.

16. Masel, R.I., *Principles of adsorption and reaction on solid surfaces*. Wiley series in chemical engineering. 1996, New York: Wiley. xiv, 804 p.

17. Lüth, H., *Solid surfaces, interfaces and thin films*. 4th, rev. and extended ed. Advanced texts in physics,. 2001, Berlin ; New York: Springer. xiii, 559 p.

18. Bruch, L.W., R.D. Diehl, and J.A. Venables, *Progress in the measurement and modeling of physisorbed layers.* Reviews of Modern Physics, 2007. **79**(4): p. 1381-1454.

19. Norskov, J.K., *Chemisorption on Metal-Surfaces.* Reports on Progress in Physics, 1990. **53**(10): p. 1253-1295.

20. Norskov, J.K., *Electronic Factors in Catalysis.* Progress in Surface Science, 1991. **38**(2): p. 103-144.

21. Somorjai, G.A. and M.A. Vanhove, *Adsorbate-Induced Restructuring of Surfaces.* Progress in Surface Science, 1989. **30**(3-4): p. 201-231.

22. Rothschild, A., Y. Komem, and N. Ashkenasy, *Quantitative evaluation of chemisorption processes on semiconductors.* Journal of Applied Physics, 2002. **92**(12): p. 7090-7097.

23. Binnig, G. and H. Rohrer, *Scanning Tunneling Microscopy - from Birth to Adolescence.* Reviews of Modern Physics, 1987. **59**(3): p. 615-625.

24. Kuk, Y. and P.J. Silverman, *Scanning Tunneling Microscope Instrumentation.* Review of Scientific Instruments, 1989. **60**(2): p. 165-180.

25. Harris, L.A., *Some Observations of Surface Segregation by Auger Electron Emission.* Journal of Applied Physics, 1968. **39**(3): p. 1428-&.

26. Auger, P., *The directions of the emission of photo-electrons.* Comptes Rendus Hebdomadaires Des Seances De L Academie Des Sciences, 1928. **186**: p. 758-760.

27. Vos, M., S.G. Anderson, and J.H. Weaver, *Inelastic mean free paths for electrons at disordered interfaces.* Physical Review B, 1989. **39**(5): p. 3274-3278.

28. Oura, K., *Surface science : an introduction.* Advanced texts in physics,. 2003, Berlin ; New York: Springer. xii, 440 p.

29. Seah, M.P. and W.A. Dench, *Quantitative electron spectroscopy of surfaces: A standard data base for electron inelastic mean free paths in solids.* Surface and Interface Analysis, 1979. **1**(1): p. 2-11.

30. Groot, F.d., A. Kotani, and ebrary Inc., *Core level spectroscopy of solids*. 2008, CRC Press: Boca Raton. p. 490.

31. Madden, H.H., *Auger Lineshape Analysis.* Surface Science, 1983. **126**(1-3): p. 80-100.

32. Stucky, G.D., et al., *Auger Line-Shape Studies of the Bonding Transition-Metal Carbonyls and Nitrosyls.* Journal of the American Chemical Society, 1982. **104**(22): p. 5951-5959.

33. Madey, T.E., et al., *Chemical State Effects in Auger-Electron Spectroscopy.* Journal of Vacuum Science & Technology, 1978. **15**(2): p. 651-651.

34. Rye, R.R., et al., *Chemical-State Effects in Auger-Electron Spectroscopy.* Journal of Chemical Physics, 1978. **69**(4): p. 1504-1512.

35. Goodman, D.W., et al., *Kinetics of the Hydrogenation of Co over a Single-Crystal Nickel-Catalyst.* Journal of Catalysis, 1980. **63**(1): p. 226-234.

36. Houston, J.E., D.E. Peebles, and D.W. Goodman, *Auger Line-Shape Studies of Carbon Species on Rh and Ni Surfaces.* Journal of Vacuum Science & Technology a-Vacuum Surfaces and Films, 1983. **1**(2): p. 995-999.

37. Koopmans, T., *The classification of wave functions and eigen-values to the single electrons of an atom.* Physica, 1934. **1**: p. 104-113.

38. Bagus, P.S., et al., *Mechanisms responsible for chemical shifts of core-level binding energies and their relationship to chemical bonding.* Journal of Electron Spectroscopy and Related Phenomena, 1999. **100**: p. 215-236.

39. Riffe, D.M., et al., *Surface core-level shifts and atomic coordination at a stepped W(110) surface.* Physical Review B, 1994. **50**(19): p. 14481.

40. Cho, J.-H., D.-H. Oh, and L. Kleinman, *Core-level shifts of low coordination atoms at the W(320) stepped surface.* Physical Review B, 2001. **64**(11): p. 115404.

41. Purcell, K.G., J. Jupille, and D.A. King, *Coordination number and surface core-level shift spectroscopy: Stepped tungsten surfaces.* Surface Science, 1989. **208**(3): p. 245-266.

42. Mannhart, J. and D.G. Schlom, *Oxide Interfaces-An Opportunity for Electronics.* Science, 2010. **327**(5973): p. 1607-1611.

43. Davisson, C. and L.H. Germer, *Diffraction of electrons by a crystal of nickel.* Physical Review, 1927. **30**(6): p. 705-740.

44. Lagally, M.G. and J.A. Martin, *Instrumentation for Low-Energy Electron-Diffraction.* Review of Scientific Instruments, 1983. **54**(10): p. 1273-1288.

45. Nieskens, D.L.S., A.P. van Bavel, and J.W. Niemantsverdriet, *The analysis of temperature programmed desorption experiments of systems with lateral*

interactions; implications of the compensation effect. Surface Science, 2003. **546**(2-3): p. 159-169.

46. Wong, Y.T. and R. Hoffmann, *Chemisorption of Carbon-Monoxide on 3 Metal-Surfaces - Ni(111), Pd(111), and Pt(111) - a Comparative-Study.* Journal of Physical Chemistry, 1991. **95**(2): p. 859-867.

47. Chalamala, B.R., D. Uebelhoer, and R.H. Reuss, *Apparatus for temperature programmed desorption studies of thin films.* Review of Scientific Instruments, 2000. **71**(1): p. 320-321.

48. Kondratyuk, P. and J.T. Yates, *Design and construction of a semiautomatic temperature programmed desorption apparatus for ultrahigh vacuum.* Journal of Vacuum Science & Technology A, 2005. **23**(1): p. 215-217.

49. Margaritondo, G., *Introduction to synchrotron radiation*. 1988, New York: Oxford University Press. xi, 280 p.

50. Wiedemann, H. and SpringerLink (Online service), *Particle accelerator physics*. 2007, Springer: Berlin ; New York. p. xxvii, 948 p.

51. Dawson, P.H., *Quadrupole mass spectrometry and its applications*. 1976, New York: Elsevier Scientific Pub. Co. ;. 349 p.

3. SOFT X-RAY PHOTOEMISSION STUDIES OF ZINC OXIDE POLAR SURFACES AND INTERFACES

This chapter is organized in three section introduction, results& discussion and conclusion. In the introduction section we briefly discuss some properties of bulk ZnO, focus on the surface properties of ZnO and the stabilization mechanisms of ZnO polar surfaces. In the result and discussion section we discuss our experimental results on ZnO. This is subdivided in two parts (a) Stabilization of clean ZnO polar surfaces- here we discuss the surface effects in the core-level photoemission spectra of ZnO and use this information to understand the stabilization mechanism of the polar surfaces of ZnO [1] (b) functionalization of ZnO with a monolayer of ZnS-here we discuss the interface electronic properties between ZnS/ZnO [2]. In the final section we discuss the conclusion of our results.

3.1 Introduction

ZnO is a wide band gap, *n*-type semiconductor with a direct band gap around 3.37 eV, and high exciton binding energy of 60 meV [3-6]. In the past there was intensive research on ZnO, due to its unique optical, semiconducting and piezoelectric properties. Research on ZnO started gradually in the fifties of the last century and peaked around the end of the seventies and the beginning of the eighties [7] . Then research interest faded as it was proving difficult to control its electrical conductivity; ZnO crystals were mostly n-

type and it was not possible to dope it to make it p-type. Over the past decade we have witnessed a revival of interest in ZnO research due to the availability of high quality ZnO substrates (single crystals, epitaxial films, nanostructures) and reports of p-type conduction when doped with transition metals [7, 8]. ZnO is used in numerous applications like, as transparent conducting electrode in solar cells, light emitting diodes and flat panel displays, as catalyst in methanol synthesis, as photocatalyst for hydrogen production from water, as chemical and biological sensors, etc. [9, 10]. Next we will summarize some of ZnO properties briefly.

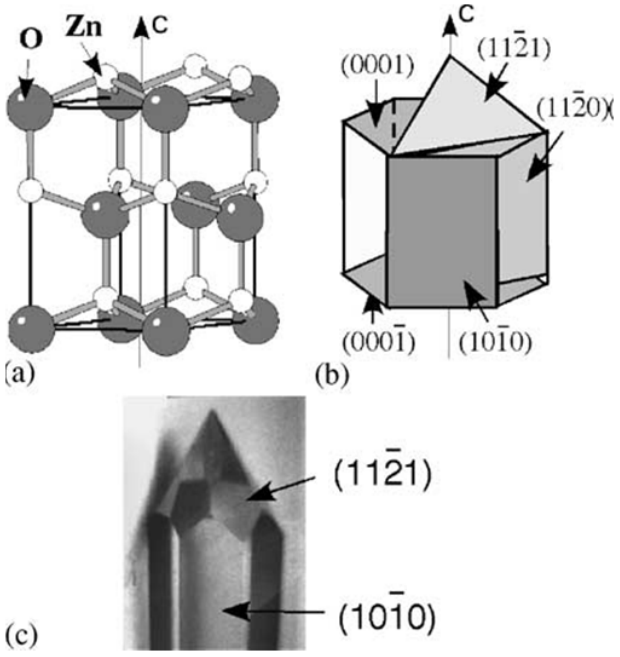

Figure 3.1: Crystal Structure of ZnO (a) Unit cell of the ZnO wurtzite crystal structure; (b) low index planes of the crystal. Figure is taken from Ref[11].

3.1.1 Crystal structure

ZnO crystallizes in the hexagonal wurtzite-type structure. The lattice constant of the ZnO hexagonal unit cell are a=3.25 Å and c=5.20 Å .This hexagonal lattice consists

of two interconnecting hexagonal-close-packed (hcp) sub-lattices of Zn^{2+} and O^{2-}, such that the two sublattices are displaced with respect to each other along the *c*-axis by the amount of u =3/8=0.375. Each sublattice includes four atoms per unit cell and each cation is surrounded by four anions and vice versa. The tetrahedral coordination gives rise to polar symmetry along the c-axis. This polarity is responsible for its piezoelectricity and spontaneous polarization [3]. The most common surfaces of wurtzite ZnO are the polar Zn terminated (0001) and O terminated $(000\bar{1})$ faces (*c*-axis oriented), and the non-polar $(11\bar{2}0)$ (*a*-axis) and $(10\bar{1}0)$ faces. The $(10\bar{1}0)$ and $(11\bar{2}0)$ surfaces are the prism faces and the $(11\bar{2}1)$ surface is the pyramid face of the crystal (see Figure 3.1) [11].

The tetrahedral coordination is also a common indicator of sp^3 covalent bonding but Zn-O possesses a very strong ionic character. Thus ZnO is on the borderline between a covalent and ionic compound. Additional to the wurtzite phase, ZnO is also known to crystallize in the cubic zinc blende and rocksalt (NaCl) structures. Zinc blende ZnO is stable only by growth on cubic substrates, while the rocksalt structure is a high-pressure metastable phase [12, 13].

3.1.2 Electronic property

The band structure of ZnO has been studied extensively both theoretically and experimentally. The LDA band structure of bulk wurtzite ZnO was calculated using dominant atomic self-interaction-corrected pseudopotentials (SIC-PP) as shown in Figure 3.2 [14]. The bottom 10 bands (occurring around −9 eV) correspond to Zn 3*d* levels. The next 6 bands from −5 eV to 0 eV correspond to O 2*p* bonding states. The upper VB of ZnO is composed of Zn- 3*d* and O-2*p* orbitals, while the lower VB is essentially

composed of O-2*s* orbitals. The conduction band is composed of unoccupied Zn-4*s* and -4*p* orbitals. The conduction band minima and valence band maxima line up at the Γ gamma point showing that ZnO is a direct band gap semiconductor. The band gap of ZnO calculated in this method is 3.77 eV which is greater than the experimental measured value of 3.37 eV at room temperature. This large band gap of ZnO is advantageous for optoelectronics applications in the blue/UV region, including light-emitting diodes, laser diodes and photodetectors. The band gap of ZnO can be tuned from~3-4 eV by addition of divalent cations like Cd or Mg respectively [15]. Undoped ZnO has *n*-type conductivity which is attributed to Zn interstitials, oxygen vacancies, or hydrogen. The intrinsic defect levels that lead to *n*-type doping lie approximately 0.01-0.05 eV below the conduction band [16, 17].

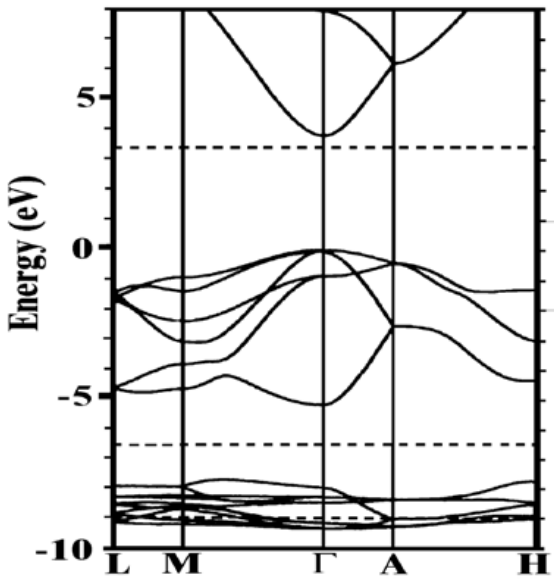

Figure 3.2: The LDA band structure of bulk wurtzite ZnO calculated using dominant atomic self-interaction-corrected pseudo-potentials (SIC-PP). Figure is taken from Ref [5].

3.1.3 Optical property

The optical properties of ZnO strongly depend on the band structure. The optical spectra reflect the direct band gap, a strongly bound exciton state, and band gap states due to point defects. The photoluminescence (PL) spectra of ZnO usually exhibit ultraviolet (UV) and visible bands. The UV band is attributed exciton states while the visible emission band observed is due to band gap states introduced by some defects, like oxygen vacancies, zinc vacancies etc.[18] The large exciton binding energy (~60 meV) makes ZnO a promising material for optical devices that are based on excitonic effects.

3.2 Surfaces of ZnO

There are four stable low index surfaces of ZnO- two nonpolar $(10\bar{1}0)$ and $(11\bar{2}0)$ parallel to the c-axis and two polar (0001) and $(000\bar{1})$ perpendicular to the c-axis. The nonpolar $(10\bar{1}0)$ and $(11\bar{2}0)$ surfaces show higher stability compared to the polar surfaces [19]. The nonpolar surfaces contain equal number of Zn and O ions. At these surfaces the coordination of the surface atoms is reduced from fourfold to threefold, thereby creating dangling bonds at the surface which makes them catalytically active surfaces. The nonpolar $(10\bar{1}0)$ surface the Zn ions have large (0.4 Å) inward relaxation compared to the O ions in the top-layer while $(11\bar{2}0)$ surface has an ideal bulk like termination [19].

The polar (0001) and $(000\bar{1})$ surfaces of ZnO are produced by cutting the crystal perpendicular to the <0001> direction which are Zn and O terminated only (see Fig 20). An (0001)-oriented ZnO surface with Zn termination is referred to as ZnO(0001)-Zn

surface, and O termination surface as ZnO$(000\bar{1})$ -O. The two polar ZnO surfaces are the most interesting ones from the fundamental and applied points of view. For the two polar ZnO surfaces, different stabilization mechanisms have been proposed. The polar faces are known to have different chemical and physical properties [20, 21]. The chemical etching behaviors of the polar surfaces are very different - with the formation of pyramidal hillocks and etch pits on the O- terminated and Zn terminated face respectively [22]. ZnO$(000\bar{1})$-O face also etches much faster than ZnO(0001)-Zn surface.

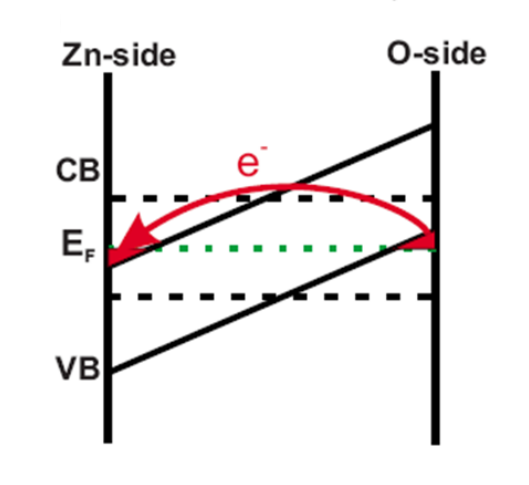

Figure 3.3: Schematic of surface metallization: The conduction and valence-band edges (CB and VB) are shown relative to the Fermi level E_F in a crystal terminated by two polar surfaces.

Polar surface of ionic crystals have surface energy that diverges with sample size, which should make them unstable but surprisingly a large number of naturally occurring materials display polar surfaces. The stabilization of both polar ZnO surfaces has been the focus of various experimental and theoretical studies [23-28]. Polar surface stabilization can occur through three mechanisms: (1) creation of surface states and transfer of negative charge from the O to the Zn face; (2) positively (negatively) charged

impurity atoms on the O (Zn) surfaces and (3) removal of surface atoms. All these mechanisms affect the surface properties differently. Till now no common stabilization mechanism for both polar surfaces has been established. In general any combination of the three mechanisms can occur simultaneously as long as the charge compensation rule is obeyed. Here I will briefly discuss the stabilization mechanisms proposed for the polar surfaces of ZnO separately.

3.2.1 ZnO(0001)-Zn surface

ZnO(0001) was believed to exist in an unreconstructed- bulk like state for a long time as (1x1) structure were observed for ZnO(0001) in LEED by Chang et.al. in 1974 and other diffraction experiments subsequently [29-33]. Ideal, unreconstructed- bulk like surface termination of ZnO(0001) surface can only achieve stabilization through electronic rearrangement between the two polar surfaces by mechanism (1). Therefore in all theoretical calculations ideal bulk like surface terminations were assumed. The calculations showed that charges (½ e^- per surface atom) are transferred from O side to Zn side which reduces the iconicity of Zn and O ions to ± 3/2 [23]. Therefore for ZnO the partial iconicity implies that the electrons on the (0001)-Zn side stay in the conduction band while the valence band at the (000-1)-O side is only partially filled, with half electron missing (see Figure 3.3). As a consequence of the partially filled surface bands both the surfaces would be metallic. However the expected 2D metallic surface states have not been observed in photoemission or scanning tunneling spectroscopy experiments [34, 35]. Moreover all calculations have consistently predicted an inward relaxation or contraction of the first Zn-O double layer, whereas in experiment a small

outward relaxation of the topmost Zn layer was found [36]. This indicates that the metallization used in all theoretical studies is not an adequate model to describe the polar Zn-terminated surface.

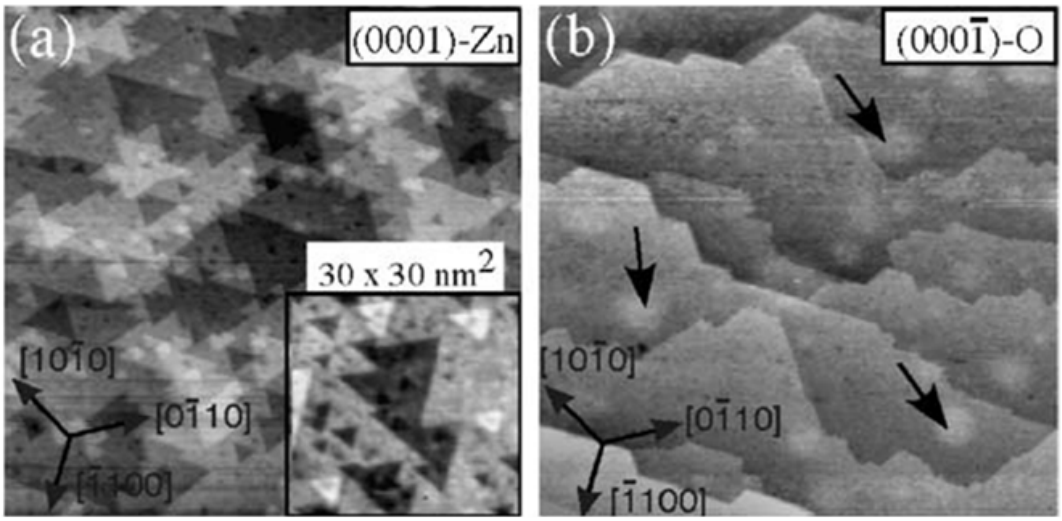

Figure 3.4: Scanning tunneling microscopy (STM) results of ZnO surfaces (a) The Zn terminated (0 0 0 1)-Zn surface is characterized by many triangular islands with monatomic step height. Step edges are O-terminated, and the resulting non-stoichiometry stabilizes this polar surface. (b) The O-terminated (00 0-1) surface exhibits stoichiometric double steps with a 120° angle. Figure is taken from Ref[11].

The compensation of charges can also be achieved by the addition of ½ ML OH^- groups or ½ ML of H^+ atoms at the Zn- and O-terminated polar surfaces respectively, according to mechanism (2). To form OH groups water or hydrogen must dissociate at the surface. Ab initio calculation by Wander and Harrison investigated the stabilization of ZnO(0001) surface by dissociation of water and adsorption H^+ and OH^- ions [37]. They found that this mechanism was energetically unfavorable compared to mechanism (1) because they had considered 1ML of H^+ and OH^- ions instead of ½ ML in their calculations. Density Functional Theory calculations by Kresse et. al. confirmed that

addition of ½ ML OH atoms depletes the surface state completely forming a stable structure [38]. They also demonstrated that ½ ML of adsorbed H stabilizes the surface. Experimental investigations however observed (1x1) pattern with hydrogen adsorbed on the surfaces [27, 39].

Jedrecy et. al. demonstrated by surface x-ray diffraction experiments on the ZnO(0001)-Zn surface that it could best be fitted by allowing a 0.75 occupancy of the topmost Zn layer , in agreement with stabilization mechanism (3) [36]. The experiments however gave no indication how this was achieved. The Zn vacancies might be ordered forming a reconstruction or may be distributed randomly. Interestingly, the most-ordered of a (2 x 2) configuration of Zn vacancies (remove every 4^{th} Zn atom) has never been observed. Another stabilization mechanism was proposed by Dulub et.el. where triangular reconstructions are formed by the removal of ¼ ML of Zn atoms in a non-periodic manner [23]. This reconstruction is characterized by triangular islands and pits of monolayer height and terminated with O atoms at the step edges (see Figure 3.4(a)). This kind of 'reconstruction' gives rise to (1x1) LEED pattern because of the lack of a periodicity in the surface structure. Density Functional Theory Calculations by Kresse et. al. also confirmed that crystal termination with triangular shaped islands and pits are indeed lower in energy than the perfect bulk terminated surfaces for a wide range of oxygen and hydrogen chemical potentials [38]. They concluded that in hydrogen-rich conditions, the surface is passivated by overlayer of hydroxyl groups, while under hydrogen poor conditions the surface forms triangular reconstructions. Thus under UHV conditions the triangular reconstruction is the most common mechanism of stabilization on the ZnO (0001) surface.

3.2.2 ZnO$(000\bar{1})$-O surface

For the ZnO$(000\bar{1})$ -O surface the stabilization mechanism is not explained yet and all of the above mentioned stabilization mechanisms have been invoked in the past. For ZnO(000-1)-O surface no island and pit like structure was found in STM studies. Smooth flat terraces separated by step edges of double layer heights and bulk stoichiometry were observed (see Figure 3.4) [11, 25] .The number of these double layer steps were not large enough to account for a similar stabilization mechanism as seen for the Zn-terminated surface (mechanism (3) by removal of $1/4^{th}$ of surface ions). Recently Wöll and co-workers observed a 1x3 surface reconstruction for a clean surface, which was interpreted as an ordered array of O-vacancies with 1/3 oxygen atoms missing [27]. This structure does, however, not entirely satisfy the electrostatic stabilization criteria (which requires 1/ 4 ML of missing oxygen) and density functional theory calculations have shown that it is not a stable surface structure [26, 40].

Surfaces states leading to metallization of the surface can make it stable but no such states were observed (mechanism (1)). So the only way of achieving stabilization is through the adsorption of charged impurities (mechanism (3)). Wöll and co-workers also proclaimed that surfaces that did not exhibit the 1x3 reconstruction were hydrogen terminated. This observation was disputed by others who claimed that a 1x1 hydrogen-free surface can be prepared [41]. *Ab initio* thermodynamics calculations for varying hydrogen and oxygen chemical potentials, allowed a construction of a phase diagram. This diagram showed that a phase with a 1/4 oxygen atoms missing is the stable phase under O and H poor conditions [24]. However, it was doubted that these conditions can

be achieved. Under realistic conditions hydrogen termination was predicted with different stable phases with hydrogen coverage of 1/2, 1/ 3, and 1/4 ML. Those phases have, however, not been experimentally confirmed and thus there still exists controversy about the surface properties of the polar ZnO surfaces.

3.3 Results and Discussion

In this section we discuss my results on ZnO research. In the first part we discuss the surface effects in the core-level photoemission spectra of ZnO and use this information to understand the stabilization mechanism of the polar surfaces of ZnO. In the second part we discuss the effect of functionalizing the ZnO polar surface with a monolayer of ZnS.

3.3.1 Soft x-ray photoemission of clean and sulfur-covered polar ZnO surfaces: A view of the stabilization of polar oxide surfaces

The two polar surfaces of ZnO were investigated by soft x-ray photoemission spectroscopy (SXPS). The low kinetic energy of the photoemitted electrons in SXPS assures a high surface sensitivity and thus enables us to measure properties of the topmost surface layers. We exploit surface effects in core-level photoemission lines in order to obtain information about the surface properties of the polar ZnO surfaces. Sulfur adsorption (by dissociate adsorption of H_2S) was used to passivate the surfaces in order to enable separation of the bulk from the surface components.

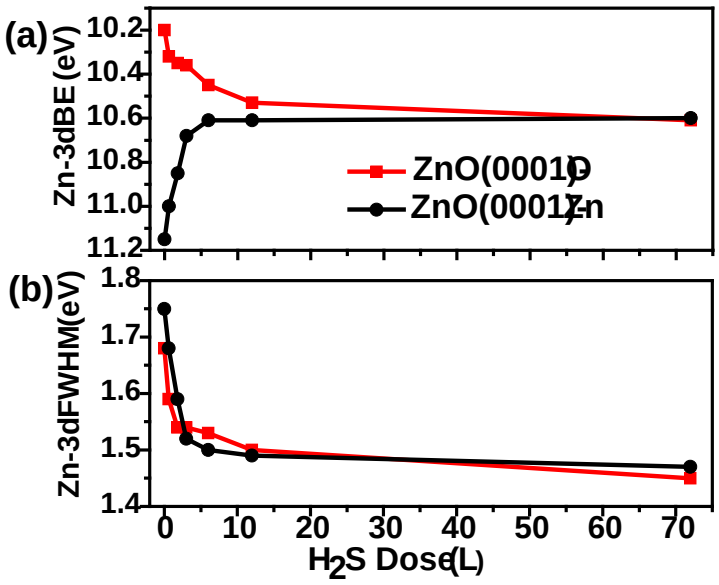

Figure 3.5: The change in the binding energy due to band bending (a) and the FWHM (b) of the Zn-3*d* peak with increasing H_2S exposure for both the Zn-terminated and the O-terminated surfaces are shown, respectively.

For the ZnO(0001)-Zn surface, the Zn-3*d*, O-1*s*, S-2*p* core levels and the valence band were monitored for increasing H_2S exposure at 600 K. At this temperature a sulfide adlayer is formed that also induces an upward surface band bending, i.e., a shift of the core levels to lower binding energy. This shift of the binding energy of the Zn-3*d* core level as a function of H_2S exposure is shown in Figure 3.5(a). The resulting surface band alignment between surface sulfide and the substrate is described in section 3.3.2. At the same time the full width at half maximum (FWHM) is becoming narrower with increasing surface sulfur coverage (Figure 3.5(b)). A similar peak narrowing is observed for the O-1*s* peak. This indicates that there is more than one component to describe the peak shape of the clean surface. The O-1*s* and Zn-3*d* peaks for different H_2S exposures are shown in Figure 3.6 and 3.7 respectively.

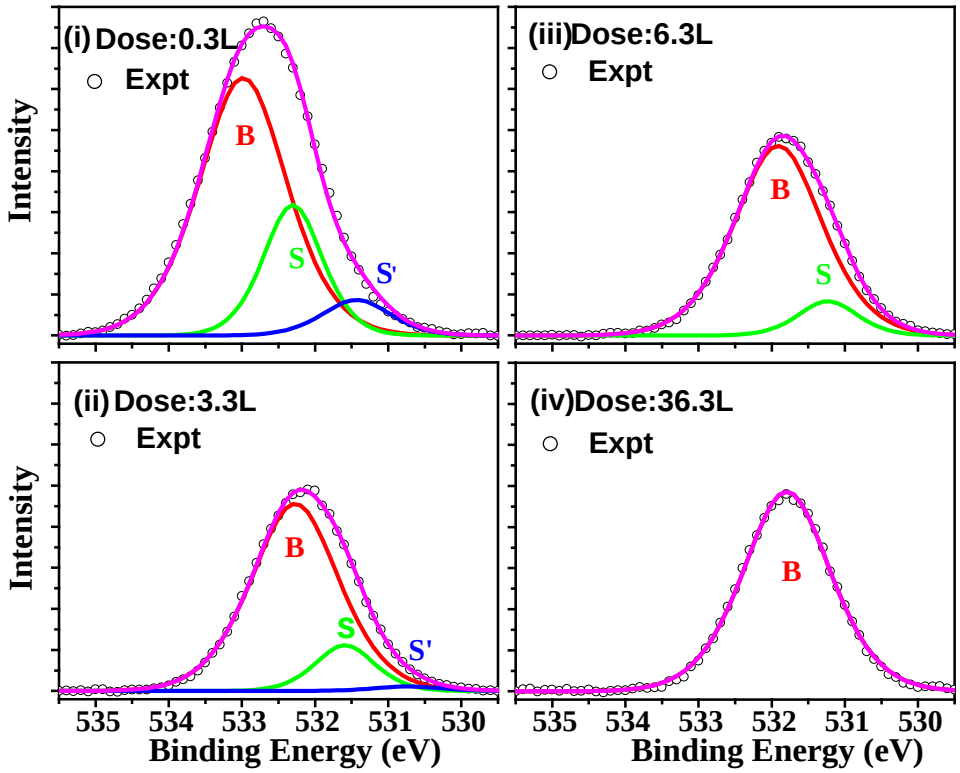

Figure 3.6: Deconvolution of the O-1*s* core level into bulk (B) and surface (S) components for the ZnO (0001)-Zn surface after H_2S exposure. The surface components S and S originate from surface atoms that have different coordination on the terraces (S) and on the steps (S'), respectively.

For the ZnO(000–1)-O surface, a similar peak narrowing of the clean surface is observed for both the Zn-3d (see Figure 3.5(b)) and O-1s peak. The observed core-level position is, however, different compared to the Zn-terminated side. On the clean surface the core levels are shifted to~1 eV lower binding energy compared to the Zn side. The shift in the peak positions is also clearly seen in the valence-band spectra for the two surfaces plotted in Figure 3.8. A relative variation in the binding energy of the bulk components between the two surfaces can only be explained by a shift of the Fermi level for the two surfaces since the two samples are electrically connected. With increasing H_2S exposure the peak position for both sides approach the same value (see Figure

3.5(a)) indicating that the cause for the shift in the Fermi level is only present for the clean surface. In further variance to the properties of the Zn-terminated side, the O-1s peak shows a high binding-energy component that can be assigned to hydroxyls.

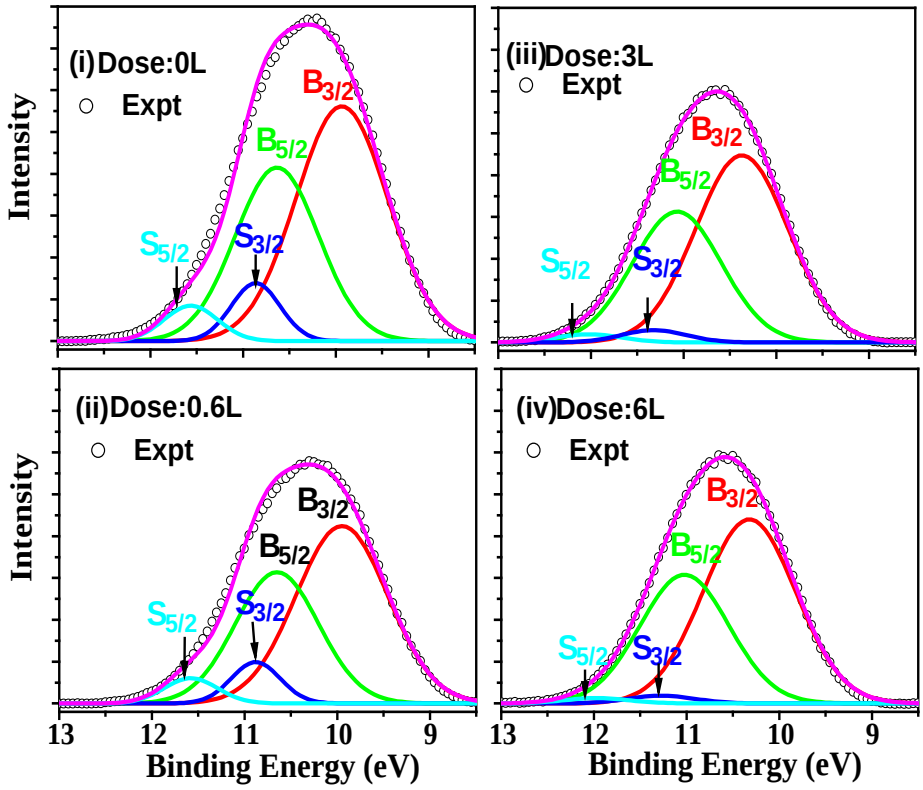

Figure 3.7: Deconvolution of the Zn-3*d* peak into two spin-orbit doublets, one for the bulk ($B_{3/2}$, $B_{5/2}$) and the surface ($S_{3/2}$, $S_{5/2}$) for the ZnO(0001)-Zn surface before and after H_2S exposure.

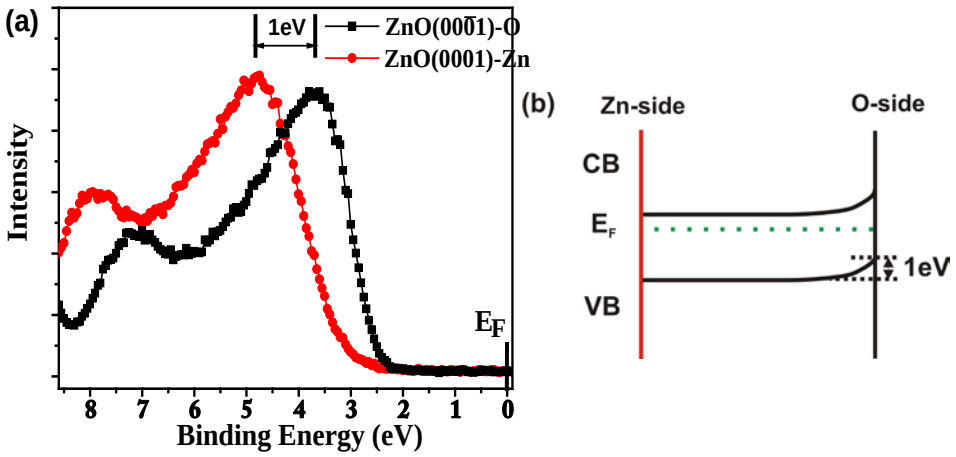

Figure 3.8: Valence band of the clean ZnO (0001)-Zn and ZnO (000–1)-O surfaces, without H_2S exposure (a). The valence-band maximum is shifted by~1 eV closer to the Fermi level for the O side compared to the Zn side. This shift in the Fermi level for the two surfaces is illustrated in (b).

Figure 3.9 shows measurements of the O-1s peak for different sample temperatures. This indicates that hydrogen is present at the surface up to~670 K. Cooling the sample below this temperature results in a rapid reformation of OH. Below 600 K the OH group is increasing due to hydrogen adsorption from the residual gas or hydrogen diffusion from the bulk. The OH peak position for low hydrogen coverage at 600 K and for higher hydrogen coverage does also shift with respect to the main O-1*s* peak. For high OH coverage below 600 K the OH peak is shifted by~2 eV from the main peak to higher binding energy. This value is consistent with values reported previously [26]. For low coverage at above 600 K the OH peak is shifted by close to 2.5 eV. We speculate that this larger chemical shift for lower OH coverage could have one of two possible origins: (i) the chemical shift is coverage dependent; an assertion based on cluster calculations for core-level positions for ZnO(000–1) that showed significant different O-1*s* positions for 2x1 and 1x1 hydrogen covered surface; or (ii) the high-temperature OH species occupy

different sites, e.g., second layer instead of surface [42]. Interestingly, with adsorption of H_2S at 600 K the OH component is disappearing. This can be seen in Figures 3.10 and 3.11, which shows the O-1*s* and Zn-3*d* peaks of the ZnO(000–1)-O for different sulfur concentration.

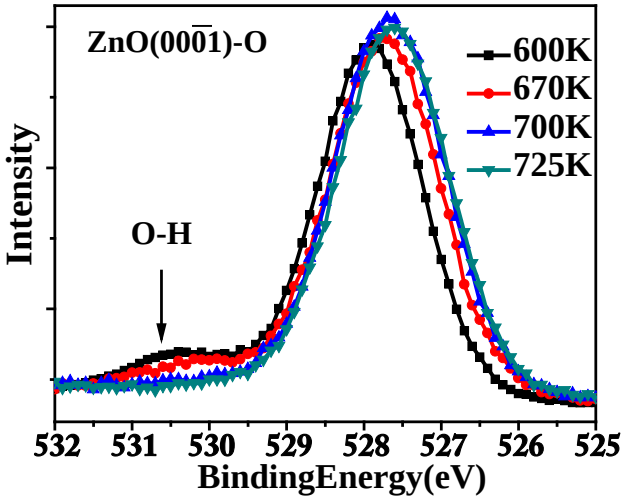

Figure 3.9: O-1*s* core level acquired at different sample temperature on the ZnO(000–1)-O surface. The shift of the high binding-energy component, assigned to OH is indicated.

3.3.1.1 Peak shape analysis

Peak shapes of semiconducting oxide surfaces are not well described theoretically. To obtain an analytical estimate of the peak shape we fitted the bulk component to a mixed Gaussian/Lorentzian line shape. We obtained a best fit for a 50% Gaussian and 50% Lorentzian for the O-1*s* and 90% Gaussian and 10% Lorentzian for the Zn-3*d* peaks. These line shapes were kept constant throughout the subsequent fitting procedures for the different components. Prior to peak fitting a Shirley background was subtracted to compensate for the secondary electron background. Two possible origins for the observed peak broadening for the clean surfaces have been considered: (i) Final

state effects; i.e., due to the adsorbate induced band bending the surface charge-carrier concentration and consequently the screening of core holes by conduction electrons is affected. This would result in a variation in the screened and unscreened portion of the photoelectron intensity. We show below that this process cannot explain the peak broadening. (ii) Initial state effects; in ionic lattices, surface atoms have a lower Madelung energy relative to the bulk position. This causes a shift of the photoemission line of the surface atoms compared to the bulk. The Madelung energy in a lattice causes a shift of the photoemission line for cations (anions) to lower (higher) binding energy compared to a free ion, this effect is reduced at the surface and consequently a shift of the surface component to higher and lower binding energies relative to the bulk component for cations and anions, respectively, is observed [43].

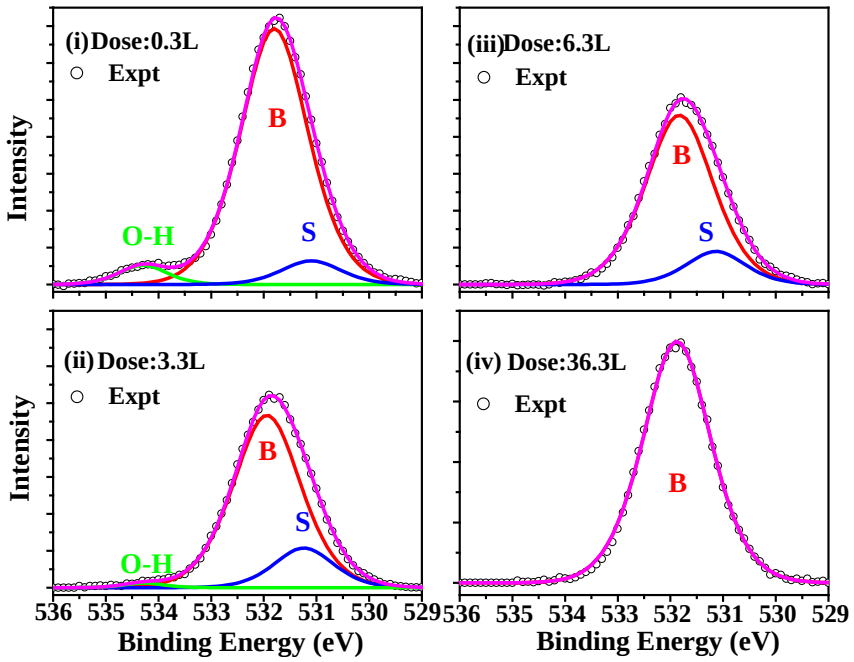

Figure 3.10: Deconvolution of the O-1*s* peak into bulk (B) and surface (S) components for the ZnO (000–1)-O surface after H_2S exposure.

First we discuss the possibility of final-state effects. Egdell and co-workers have demonstrated for Sn doped In_2O_3 and Sb doped SnO_2 that final-state effects can contribute significantly to the core-level line shapes [44, 45]. These materials are closely related to ZnO because all these materials exhibit a free-electron *s*-like conduction band that gives rise to high conductivity. Because of these similarities one may expect that plasmon losses also could contribute to the observed peak broadening in ZnO. The plasmon loss intensity is expected to scale with $\sqrt[3]{n}$, where n is the charge-carrier concentration, and the plasmon loss energy should be proportional to the $\sqrt{n}$.

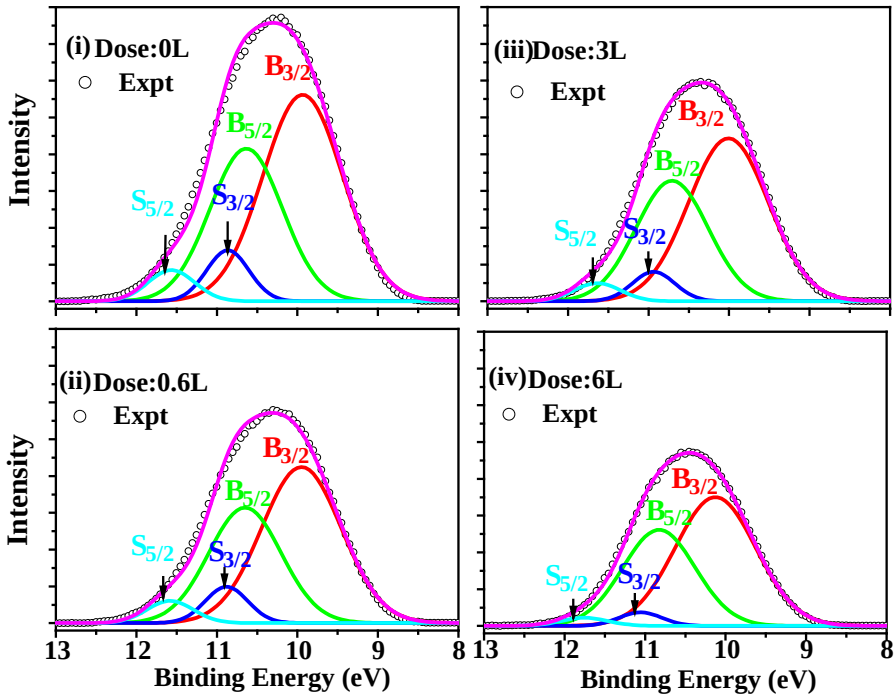

Figure 3.11: Deconvolution of the Zn-3*d* peak into two spin-orbit doublet, one for the bulk ($B_{3/2}$, $B_{5/2}$) and the surface ($S_{3/2}$, $S_{5/2}$) for the ZnO$(000\bar{1})$-O surface before and after H_2S exposure.

Since the charge-carrier contribution depends exponentially on the separation between Fermi level and conduction band minimum, a strong variation in charge carrier

concentration is expected for the observed band bending of~0.5 eV with increasing H_2S exposure for the ZnO(0001)-Zn surface (see Figure 3.5(a)). Thus the band bending enables us to estimate the variation in the charge-carrier concentration *n* and consequently the expected variation in the intensity and energy position of the screened component. Low amounts of H_2S adsorption resulted already in a large band bending. Consequently, because of an exponential dependence of the charge-carrier concentration, a strong change in the screened component would be expected. Attempts to deconvolute the Zn-3*d* and O-1*s* peaks into screened and unscreened components did, however, not satisfy such a strong dependence of the intensity of the screened component on the band bending. This failure of the intensity ratios between screened and unscreened component to reproduce the expected dependence on the amount of band bending already indicates that plasmon losses on these nominally undoped ZnO single crystals do not play a significant role for explaining the peak shape. This conjecture can be made even more convincingly for the ZnO (000–1)-O surface. Here we observe the opposite trend for the Fermi-level position with H_2S exposure, i.e., the Fermi level lies close to the center of the band gap for the clean surface (see below for an explanation for this unexpected observation) and shifts closer to the conduction band with H_2S exposure (see Figure 3.5(a)). Thus stronger plasmon losses would be expected for the sulfur covered surface compared to the clean surface. This is opposite to the observed larger peak broadening for the clean surface. Consequently we can confidently exclude the possibility that final-state effects contribute significantly to the line shape of undoped ZnO.

Now we show that the varying Madelung energies at the surface explain the observed peak broadening for the clean surfaces. Surface effects in core-level

photoemission of ionic crystals are well documented for GaAs, ZnSe, and other compound semiconductors [46, 47]. Removing the vacuum termination of the substrate by an adsorbate is reducing this surface effect [48]. Consequently, the observed peak narrowing with increased sulfur coverage for both surfaces can be explained by a suppression of the surface component. Sulfur uptake measured from the S-2*p* peak intensity and scanning tunneling microscopy (STM) measurements of sulfidized ZnO surfaces indicate a two-dimensional–layer growth and therefore sulfur is an ideal adsorbate to cover the surface. The intensity ratio of the surface relative to the bulk component depends on the inelastic mean-free path of the photoemitted electrons. The data shown above were acquired with soft x rays with photon energies of 150 and 630 eV forthe Zn-3*d* and O-1*s* peaks, i.e., with kinetic energies of~125 eV for the photoelectrons. This is the energy range of highest surface sensitivity with a mean-free electron path between 6 and 8 Å, depending on the estimate [49]. A mean-free path of 8 Å translates into an expected surface to bulk ratios of 0.3, for the clean ZnO surfaces. Additional uncertainties may arise due photoelectron diffraction effects. At these low kinetic electron energies elastic backscattered electron may cause interferences that can modulate the photoelectron intensity. From multiple electron-scattering calculations we estimate that this could cause a maximum variation in the surface to bulk ratio of a factor of 2 [49]. Nevertheless, the contribution of the surface layer to the photoemission spectrum is considerable and thus the peak broadening could originate from a surface component [50].

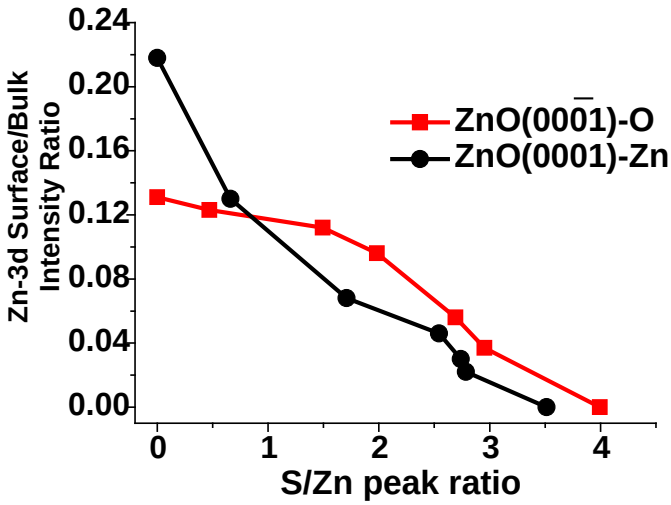

Figure 3.12: Intensity ratio of the surface component to the bulk component for the Zn-3*d* peak as function of the S or Zn peak ratio.

In principle chemical shifts due to sulfur adsorption at the interface between the surface sulfide and the ZnO substrate could also cause a broadening upon surface sulfidation. However, since we observe the opposite trend, i.e., a peak narrowing with increasing sulfide formation, we conclude that chemical shifts due to Zn-S formation are smaller compared to changes in the surface Madelung energy. Thus the observed narrowing is treated solely as a result of removing the surface component and consequently we use the sulfur covered surface as a measurement of the bulk component of the core-level peaks. This bulk peak shape then enables us to deconvolute the peaks of the clean (or only partially sulfur covered) samples into their bulk and surface components. The results of this peak deconvolution procedure are shown in Figures 3.9 and 3.10 for the two polar surfaces.

The Zn-3*d* peak was not resolved in its 5/2 and 3/2 multiplets. For the fitting procedure these two components were, however, taken into account. The spin-orbit split and the 3/2 to 5/2 peak ratios were constrained to 0.7 eV and a ratio of 2:3, respectively, while the FWHM of the components were kept free. The FWHM of the bulk component was determined from fitting the Zn-3*d* peak at highest sulfur exposure as mentioned above. In subsequent fitting procedure this FWHM value was kept constant. Freely adjustable fitting parameters were the peak positions of the bulk and surface components in order to accommodate band bending. A test for the fitting procedure is that the intensity ratio between the surface and bulk components is expected to decrease for a strictly two-dimensional coverage of the surface by sulfur. Figure 33 shows the intensity ratio of the surface and bulk component of the Zn-3*d* peak as a function of the S-2*p*/Zn-3*d* peak ratio. A monotonous decrease in the surface component is observed for both polar surfaces, indicating a layer growth in agreement with our STM observations [2].

From the peak deconvolution we observe a shift of the Zn-3*d* surface component of 0.95 eV for the ZnO (0001)-Zn and 0.93 eV for the ZnO(000–1)-O surface relative to the bulk position. This surface shift compares favorable for reported surface components due to the reduced Madelung energy on related materials, such as ZnSe, for which a shift of 0.9 eV has been reported [47]. The deconvolution of the O-1*s* peak followed similar procedures as for the Zn-3*d* peaks. However, it was not always possible to obtain satisfying fits with only two components. For the ZnO(000–1)-O side we have to take the aforementioned hydroxyl oxygen peak into account, while on the ZnO(0001)-Zn side the O-1*s* peak needed to be fit by two lower binding-energy peaks relative to the bulk component. This may indicate the presence of surface oxygen sites with different

Madelung energy, i.e., surface sites with different coordination. The intensities of the different peak components (normalized to the full peak area) and the peak positions relative to the bulk components are summarized in Table I for the two surfaces for varying H_2S exposure. It may be also worth mentioning that the observed shifts of the surface components to higher binding energy for the cation (Zn) and lower binding energy for the anion (O) is the expected direction for the surface component due to a reduced Madelung energy at ionic surfaces. Therefore the reduced Madelung energy at the surface causes the observed peak broadening for clean ZnO surfaces.

The surface structure of the ZnO(0001)-Zn surface prepared in UHV has been thoroughly analyzed by scanning probe techniques [23, 25]. These measurements resulted in the conclusion that this polar surface is stabilized by a~1/4 of a monolayer Zn-deficient surface. This Zn deficiency is established by formation of a high density of step edges that have an O termination. This implies that there are two differently coordinated O sites at the surface. O atoms at step edges have less Zn-cation neighbors, which will result in a larger shift of the Madelung energy relative to terrace and bulk O sites. Consequently, the observed two surface components in the O-1*s* peak for the clean ZnO(0001)-Zn surface is assigned to step and terrace sites. The ratio of the photoelectron intensities of these two peaks of~ 0.3 corroborates such an assignment since it is close to the factor of 1/4 deduced from simple electrostatic stabilization arguments of polar surfaces [43].

TABLE I: Results of the deconvolution of the surface and the bulk components of O-1s peak-binding energy (BE), full width at half maximum (FWHM), component intensities normalized to the peak area and the intensity ratio of the surface to bulk component.

Surface	**H_2S Dose (L)**	**Components**	**BE (eV)**	**FWHM (eV)**	**Area**	$\frac{\mathbf{I(S+S')}}{\mathbf{I(B)}}$
ZnO(0001)	0.3	Bulk Comp.(B)	552.985	1.41	0.69	0.45
		1st Surface Comp.(S)	552.305	0.95	0.23	
		2nd Surface Comp.(S')	551.435	1.09	0.07	
	3.3	Bulk Comp.(B)	552.273	1.41	0.84	0.18
		1st Surface Comp.(S)	551.593	0.95	0.14	
		2nd Surface Comp(S')	550.727	1.09	0.02	
	6.3	Bulk Comp.(B)	551.911	1.41	0.89	0.12
		Surface Comp.(S)	551.232	0.95	0.11	
	36.3	Bulk Comp.(B)	551.795	1.41	1.00	0
ZnO(000-1)	0.3	Bulk Component(B)	531.821	1.49	0.84	0.19
		Surface Component(S)	531.161	1.36	0.11	
		Hydroxyl(OH)	534.283	1.10	0.05	
	3.3	Bulk Component(B)	531.974	1.49	0.76	0.30
		Surface Component(S)	531.314	1.36	0.22	
		Hydroxyl(OH)	534.276	0.93	0.01	
	6.3	Bulk Component(B)	531.854	1.49	0.81	0.23
		Surface Component(S)	531.854	1.36	0.19	
	36.3	Bulk Component(B)	531.878	1.50	1.00	0

The fact that differently coordinated surface ions have distinctively different Madelung energies and therefore should exhibit different photoemission lines is well established. However, usually surfaces do not exhibit a large number of under-coordinated defect sites. The ZnO (0001)-Zn surface is different than most other surfaces because the stability requirement of this polar surface forces it to create a well defined

step edge density. Other surfaces with known step edge densities and structure may, however, be formed by other means, such as formation of vicinal surfaces. In all these cases the differentiation of step edge atoms from terrace sites would enable us to perform site specific studies. For example, adsorption at step edges should be differentiable from adsorption on terrace sites by monitoring the shifted surface components. In our measurements sulfur adsorption causes a more rapid decrease in the surface component assigned to step edges compared to terrace sites. This is consistent with our STM studies that showed that at 600 K that sulfide islands nucleate a step edges but that they form 2D islands thus covering both step edges and terraces.

The stabilization mechanism for the ZnO(000–1)-O polar surface is not well understood. On our samples we always observed OH below sample temperatures of 670 K. The amount of OH increased at lower temperatures. At 600 K the O-1*s* peak intensity associated with hydroxyls did not change significantly with time, suggesting an equilibrium situation. Contamination of the surface with hydrogen lowers the electrostatic energy due to the bulk dipole moments and thus lowers the surface energy. Our observation agrees with previously made assertions that preparation of a hydrogen free ZnO(000–1)-O surface is extremely difficult [28]. At the moment we cannot distinguish if the hydrogen is diffusing out of the bulk (hydrogen is a known bulk impurity in ZnO) or is adsorbed from the residual gas in the UHV chamber.

It is tempting to use the surface sensitivity of soft x-ray photoemission to compare the oxygen and zinc composition of the surface for the two polar surfaces in order to decide if the polar surfaces are stabilized by ion deficiencies. Unfortunately,

photoelectron diffraction effects on single-crystal surfaces can influence the measured photoelectron intensity significantly, which makes accurate determination of the surface composition difficult. For instance, using the peak areas normalized by the photon flux, we measure an about 8% more intense Zn-3*d* peak on the ZnO(0001)-Zn side compared to the ZnO(000–1)-O side. This appears to contradict the known stabilization mechanism of the ZnO(0001)-Zn surface by formation of Zn-deficient surface with˜1/4 ML Zn missing. Multiple electron-scattering calculations are, however, in agreement with a stronger intensity of surface Zn atoms for the ZnO(0001)-Zn side compared to the ZnO(000– 1)-O surface for the kinetic energies of the photoelectrons used in this study and thus this apparent discrepancy can be explained by diffraction effects. Similar measurements for the O-1*s* signal show an about 3% stronger signal on the O side compared to the Zn side. Although this does not indicate any O deficiency on the O side, photoelectron diffraction effects can offset compositional variations at the surface. Consequently our measurements do not allow an unambiguous determination of the oxygen concentration of then ZnO(000–1)-O surface. More detailed measurements of photoelectron diffraction at different photon energies and emission angles would be necessary to resolve the issue of O composition.

The Fermi-level position for the O and Zn sides is quite different for the two polar surfaces, but approaches the same value for S-covered surfaces (see Figure 3.5(a)). For the Zn-side we measure the valence-band maximum about 3.2 eV below the Fermi edge, i.e., at a position expected for *n*-type ZnO. Thus the Zn-terminated surface does not show any significant variation from the Fermi level position in the bulk. The O side, on the other hand exhibits a shift of the Fermi level by˜1.2 eV closer to the center of the band

gap. Such shifts occur due to electrostatic band bending. Electrostatic shifts in binding energies are common for charged molecules adsorbed at the surfaces or formation of interfaces. For the O side the only adsorbate present is hydrogen. Hydrogen, a positively charged adsorbate, always induces a downward band bending (shift of the Fermi level closer to the conduction band), i.e., the opposite from what is observed. Furthermore, a complete removal of hydrogen at 650–700 K as shown in Figure 3.9 does not change the position of the Fermi level significantly. Consequently a different mechanism than surface adsorbates is responsible for the Fermi-level shift at the O side.

The obvious explanation comes from the electrostatic potential that builds up at a polar surface if the bulk dipole is not (or only partially) compensated by any other charge transfer mechanism. This implies that under our experimental conditions there are not enough oxygen vacancies or ionic impurity charges to completely compensate for the electrostatic potential buildup due to the internal dipoles. The downward shift of the Fermi level at the surface in this *n*-type material will result in a positive space-charge region which will contribute to lowering the electrostatic potential at the surface. Our observed Fermi-level shift to about midgap position does not allow for a depletion of valence-band electrons and thus charge redistribution as described in Figure 3.3 will not occur. Therefore, unless there exist higher lying surface states that are emptied by pushing the Fermi level to midgap the only charges are from ionized donors that have to exist to make the sample *n* type. However, there are unlikely to be enough donors to provide a large enough positive surface charge (even if it extends over several tens of nanometers into the bulk) to stabilize the surface. Therefore at this point it seems unlikely that the shift of the Fermi level to the midgap is the only stabilization mechanism at

elevated temperatures. Nevertheless, our observation is significant since it provides the first experimental evidence that the O side is not completely stabilized by O vacancies or hydrogen at above 600 K. The fact that this shift of the Fermi level is only observed at elevated temperatures, where the hydrogen is desorbed suggests that hydrogen adsorption stabilizes the surface at lower temperatures and possibly is the reason why this shift has not been observed previously. For the Zn side the removal of ¼ Zn atoms stabilizes the surface and thus no electrostatic shift of the Fermi level is observed at all temperatures.

It is likely that hydrogen is strongly adsorbed on the ZnO(000–1)-O surface because it stabilizes the polar surface. Thus one may speculate that if a different stabilization mechanism is provided, the hydrogen interaction with the surface is weakened. This hypothesis could explain the following observation: Dissociative adsorption of H_2S provides more hydrogen to the surface, however, as can be seen from the O-1*s* spectra (Figure 3.9); the OH shoulder is rapidly decreasing and vanishes completely after exposure of 3.3L H_2S, corresponding to a sulfur coverage of 0.5 ML. Consequently, although there are still plenty of O sites for hydrogen to adsorb, sulfur coadsorption at the surface lowers the desorption temperature of hydrogen. Therefore we propose that for ZnO(000–1)-O hydrogen adsorption is the most likely source for stabilization under regular conditions, but this stabilization mechanism may be influenced by coadsorbates. Consequently coadsorbates may strongly influence the chemical properties of the surface.

3.3.2 Surface Functionalization of ZnO with Monolayer of ZnS

We have studied the interface properties of ZnO modified with a (sub) monolayer of ZnS. The morphology of ZnS films on ZnO is crucial for interpretation of the fundamental electronic properties. Therefore we discuss the surface morphology as found from STM studies first, followed by the electronic structure characterization derived from photoemission studies.

STM studies indicate that ZnS grows by nucleation and growth of 2D islands, of monolayer height (~2.5 Å). After exposure to 3-6 L H_2S a dense network of meandering islands is formed. STM images of ZnO surface for low H_2S exposure and for saturation H_2S dose is shown in Figure 3.13, panels a and b, respectively. For such films the S-$2p^{3/2}$ core level is detected at a binding energy (BE) of 162.3 eV for low S-coverage and at 162.2 eV for a saturation dose. This BE is consistent with sulfide formation. However, the value is about 0.4 eV higher than that reported for bulk ZnS (161.8 eV) [51]. Although the atomic scale structure of the sulfide film cannot be unambiguously deduced from our STM studies, some islands exhibit hexagonal symmetry. Therefore, it is reasonable to assume that ZnS adopts the wurtzite structure of the ZnO substrate and an epitaxial relationship between substrate and film is established. The much larger lattice constant of wurtzite-ZnS (a = 3.82 Å; c = 6.26 Å) compared to ZnO (a = 3.25 Å; c = 5.21 Å) implies that a complete ZnS monolayer would be under considerable compressive stress. Therefore the formation of the meandering island morphology is likely to be a strain relieve-mechanism of the film. The large strain, a complete ZnS film would have, implies an increase in the S-chemical potential with ZnS coverage and thus

provides a reason for the saturation of the sulfur uptake before completion of the monolayer.

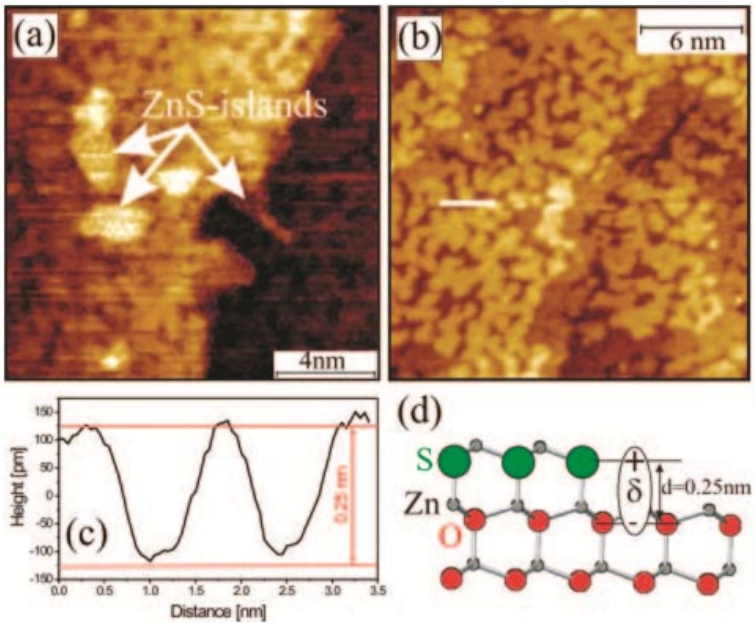

Figure 3.13: STM images of sulfur induced surface structure for (a) 0.6 L H_2S and (b) 3 L H_2S exposure. The cross-section indicated in (b) is shown in (c). A ball-and-stick model of the surface structure is shown in (d) with the surface dipole moment indicated.

In order to assess the influence of the submonolayer film on the fundamental surface properties and thus the photocatalytic properties the alterations of the electronic structure needs to be analyzed. Photoemission has been used to measure the electronic interface properties between ZnO and (sub) monolayer ZnS films. Experiments were performed for increasing H_2S exposure. The results of these measurements are summarized in Figure 3.14. One graph shows the S-2p/Zn-3s peak ratios, which indicates that initially the surface coverage increases rapidly. At 6L H_2S a saturation of the surface phase is reached, subsequent increase in the S-2p intensity is slow. This behavior is in

agreement with the STM studies that indicate a 2D island growth mode of ZnS. A similar behavior has also been reported for the ZnO($11\bar{2}0$) surface [52].

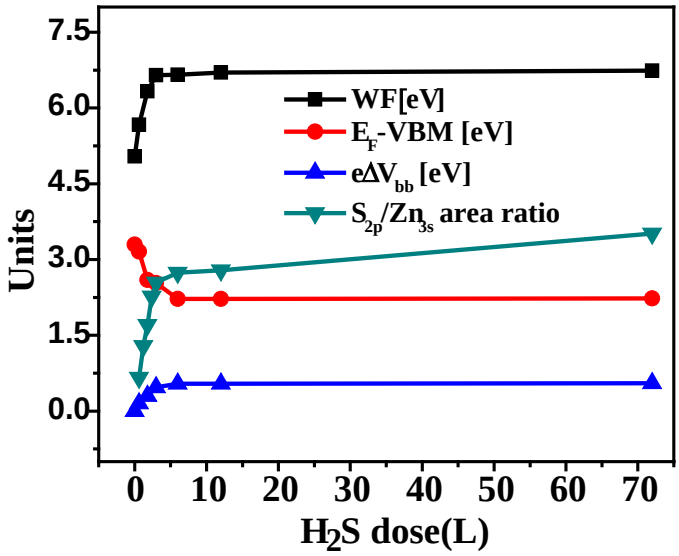

Figure 3.14: Summary of the changes in the work function, valence band maximum (relative to the Fermi level), band bending in the substrate, and the S2p/Zn3s peak ratios as a function of H_2S exposure are shown. All properties saturate between 3 and 6 L H_2S exposure.

The core level peak positions for O-1s, Zn-3s, and 3d have been used for evaluating the band bending induced in the ZnO substrate by sulfur exposure. Figure 3.16(a) shows for example the Zn-3d core level position for different S-exposures. A shift of 0.55 eV to lower binding energies with increasing S-exposure is observed. This core level shift also saturates at 3-6 L exposure. A similar shift has been measured for the O-1s core level. These shifts can be attributed to an electrostatic upward band bending due to surface charge transfer. The valence band was monitored with photon energy of 150 eV and this is shown in Figure 3.15(b). In addition to a shift to lower binding energies of the valence band maximum (VBM) due to upward band bending, a new state is formed

on top of the valence band in the band gap of ZnO. This state is due to the ZnS layer at the surface. This ZnS state can be clearer appreciated in difference spectra. In these spectra the spectrum of the clean ZnO surface has been shifted by the amount of band bending and subtracted from the spectra after H_2S exposures. The top of the ZnS states are observed at

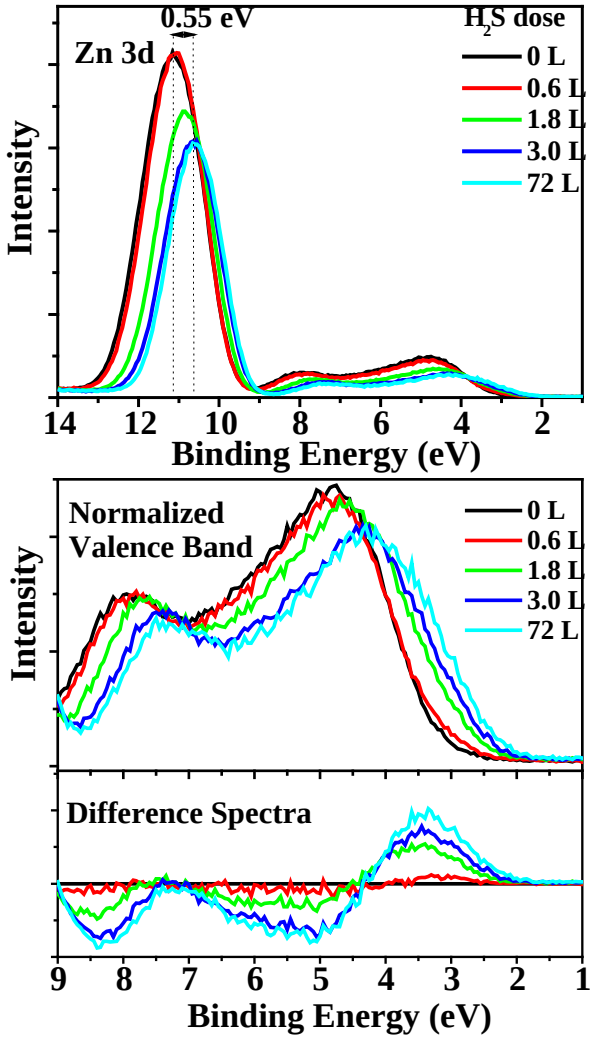

Figure 3.15: Valence and Zn-3d shallow core level photoemission spectra for different H_2S exposures. The band bending induced shift in the Zn-3d core level can be observed in (a). The change in the valence band is shown in (b). The difference spectra are calculated by subtraction of the spectrum of the clean surface after shifting it to compensate for band bending effects.

2.1-2.2 eV below the Fermi level. Interestingly, the onset of this state does not shift with S-coverage, indicating that the electronic properties of the growing ZnS film does not change significantly with coverage. This is contrary to what one would expect for a strained film.

The measurement of the work function indicates a large increase upon formation of the ZnS layer (see Figure 3.15(b)). For the clean ZnO (0001)-Zn surface we obtain a value of 5.0 eV (literature values for ZnO surfaces vary between 3.7 and 6 eV) this value increases by 1.7 to 6.7 eV upon formation of the ZnS layer [53]. This increase in work function has two contributions: (i) band bending, and (ii) surface dipole moment. After subtracting the upward band bending (0.55 eV) we arrive at a dipole induced increase in the work function of 1.15 eV. This indicates a surface dipole layer with the positive side toward the vacuum. A likely origin of this strong change lies in the larger electronegativity of O compared to S. Therefore in a layer model of ZnS on top of the ZnO substrate, as is shown in Figure 32(d), charges from the ZnS surface are transferred to the ZnO substrate. Such a charge transfer is substantiated by the chemical shift of S-2p core level position to higher BE compared to the reported bulk ZnS value. Assuming a structure as indicated in Figure 32(d) we can estimate the dipole moment per surface S-atom to δ = 0.25 D, or a corresponding charge transfer of 0.02 e^- per S-atom.

By combining all the above measurements and using 3.4 eV for the ZnO band gap, the interface band diagram can be derived. This is shown in Figure 3.16. Due to electronic hybridization of the monolayer ZnS film with the ZnO substrate photoexcitation from the ZnS surface states to the ZnO conduction band are possible.

Thus an effective band gap narrowing from 3.4 to 2.8 eV is observed at the interface. A similar band gap narrowing has been observed for S-doped ZnO and may also be responsible for the reported green light photoluminescence in S-doped ZnO nanomaterials [54, 55].

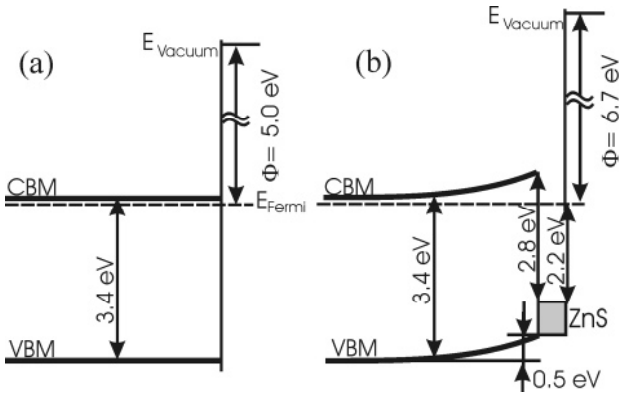

Figure 3.16: Schematic diagram of the surface band structure of (a) the clean ZnO-(0001) surface (b) after formation of ZnS surface layer on ZnO.

A staggered band alignment between ZnO and ZnS was also recently predicted by DFT calculations [56]. However, our observed effective band gap of 2.7-2.8 eV is much larger than the predicted (1.82 eV) value. This is partially because a significant narrowing of the fundamental band gap in ZnO was predicted due to ZnS induced lattice strain. In our experimental studies of (sub) monolayer ZnS films we do not see any shift of the ZnS states with increasing coverage as one would expect if the strain in the film were to play an important role in the interface electronic structure. Therefore we propose that the formation of ZnS-island morphology provides an efficient strain relieve mechanism for pseudomorphic ZnS layers.

Apart from reducing the photoexcitation threshold to lower photon energy the electronic structure has several other implications for the use of this material for photochemical applications. The band bending at the surface will facilitate the electronhole separation. Holes, on the other hand, will be trapped in the ZnS adlayer states that have a lower BE than the top of the ZnO valence band. Here the holes become available for charge transfer to a donor molecule in the gas phase or solution. The increase in work function will shift the redox potential of these adsorbed donor molecules to more negative values, i.e., to lower binding energies relative to the VBM. This will increase the thermodynamic driving force for charge transfer from donor molecules to holes trapped in the ZnS layer. All these alterations of the surface properties taken together will enhance hole mediated photo catalytic reactions at the ZnS modified surface compared to the clean ZnO surface.

3.5 Conclusion

The two polar surfaces of ZnO were investigated by soft x-ray photoemission spectroscopy. Surface components due to variation in the Madelung energy were identified in photoemission core-level spectra. Sulfur adsorption was used to passivate the surfaces in order to separate the bulk from the surface components. For the ZnO(0001)-Zn surface the observed photoemission peaks were consistent with a Zn deficient surface, exhibiting a high density of O-terminated step edges. The ZnO$(000\bar{1})$-O surface is very reactive toward hydrogen adsorption and only above 650 K a hydrogen free surface was observed. For hydrogen-free and small hydrogen coverage an electrostatic shift of the Fermi-level toward the band-gap center was observed. This

indicates an incomplete compensation of the internal electrostatic potential by surface oxygen vacancies or charged adsorbates. Coadsorption of sulfur lowered the desorption temperature for hydrogen indicating the possibility to tune the chemical properties of these polar surfaces by dopants.

We show by photoemission spectroscopy that modification of ZnO with submonolayer films of ZnS, two materials with band gaps larger than 3.4 eV, results in an effective surface band gap narrowing to 2.8 eV. This reduces the photoexcitation threshold energy and thus potentially enhances the solar energy conversion capabilities of such a heterostructure photocatalysts. Furthermore, the characterization of the space charge region and work function of ZnS modified ZnO indicate improved surface properties for enhancing photocatalytic activity.

3.6 References

1. Lahiri, J., S. Senanayake, and M. Batzill, *Soft x-ray photoemission of clean and sulfur-covered polar ZnO surfaces: A view of the stabilization of polar oxide surfaces.* Physical Review B, 2008. **78**(15): p. 10.

2. Lahiri, J. and M. Batzill, *Surface functionalization of ZnO photocatalysts with monolayer ZnS.* Journal of Physical Chemistry C, 2008. **112**(11): p. 4304-4307.

3. Jagadish, C. and S.J. Pearton, *Zinc oxide bulk, thin films and nanostructures : processing, properties and applications*. 2006, Amsterdam ; London: Elsevier. ix, 589 p.

4. Avrutin, V., et al., *Bulk ZnO: Current Status, Challenges, and Prospects.* Proceedings of the Ieee, 2010. **98**(7): p. 1339-1350.

5. Janotti, A. and C.G. Van de Walle, *Fundamentals of zinc oxide as a semiconductor.* Reports on Progress in Physics, 2009. **72**(12): p. 126501-.

6. Ozgur, U., et al., *A comprehensive review of ZnO materials and devices.* Journal of Applied Physics, 2005. **98**(4): p. 103.

7. Klingshirn, C., et al., *ZnO rediscovered - once again!?* Superlattices and Microstructures, 2005. **38**(4-6): p. 209-222.

8. Ozgur, U., D. Hofstetter, and H. Morkoc, *ZnO Devices and Applications: A Review of Current Status and Future Prospects.* Proceedings of the Ieee. **98**(7): p. 1255-1268.

9. Klingshirn, C., *ZnO: From basics towards applications.* Physica Status Solidi B-Basic Solid State Physics, 2007. **244**(9): p. 3027-3073.

10. Klingshirn, C., *ZnO: Material, physics and applications.* Chemphyschem, 2007. **8**(6): p. 782-803.

11. Diebold, U., L.V. Koplitz, and O. Dulub, *Atomic-scale properties of low-index ZnO surfaces.* Applied Surface Science, 2004. **237**(1-4): p. 336-342.

12. Phillips, J.C., *Covalent-ionic and covalent-metallic transitions of tetrahedrally coordinated $A^N B^{8-N}$ crystals under pressure* Physical Review Letters, 1971. **27**(18): p. 1197-&.

13. Bates, C.H., R. Roy, and W.B. White, *New high-pressure polymorph of zinc oxide.* Science, 1962. **137**(3534): p. 993-&.

14. Vogel, D., P. Kruger, and J. Pollmann, *Ab-initio electronic-structure calculations for II-VI semiconductors using self interaction corrected pseudopotentials.* Physical Review B, 1995. **52**(20): p. 14316-14319.

15. Makino, T., et al., *Band gap engineering based on MgxZn1-xO and CdyZn1-yO ternary alloy films.* Applied Physics Letters, 2001. **78**(9): p. 1237-1239.

16. Norton, D.P., et al., *ZnO: growth, doping & processing.* Materials Today, 2004. **7**(6): p. 34-40.

17. Zhang, S.B., S.H. Wei, and A. Zunger, *Intrinsic n-type versus p-type doping asymmetry and the defect physics of ZnO.* Physical Review B, 2001. **63**(7): p. 075205.

18. Reynolds, D.C., et al., *Neutral-donor-bound-exciton complexes in ZnO crystals.* Physical Review B, 1998. **57**(19): p. 12151-12155.

19. Nyberg, M., et al., *Hydrogen dissociation on reconstructed ZnO surfaces.* Journal of Physical Chemistry, 1996. **100**(21): p. 9054-9063.

20. Chevtchenko, S.A., et al., *Comparative study of the (0001) and 000(1)over-bar surfaces of ZnO.* Applied Physics Letters, 2006. **89**(18): p. 3.

21. Akhter, S., K. Lui, and H.H. Kung, *Comparison of the chemical properties of the zinc-polar, the oxygen-polar, and the nonpolar surfaces of zinc oxide.* The Journal of Physical Chemistry, 1985. **89**(10): p. 1958-1964.

22. Mariano, A.N. and R.E. Hanneman, *Cryattalographic polarity of ZnO crystals* Journal of Applied Physics, 1963. **34**(2): p. 384-&.

23. Dulub, O., U. Diebold, and G. Kresse, *Novel stabilization mechanism on polar surfaces: ZnO(0001)-Zn.* Physical Review Letters, 2003. **90**(1): p. 4.

24. Meyer, B., *First-principles study of the polar O-terminated ZnO surface in thermodynamic equilibrium with oxygen and hydrogen.* Physical Review B, 2004. **69**(4): p. 10.

25. Dulub, O., L.A. Boatner, and U. Diebold, *STM study of the geometric and electronic structure of ZnO(0001)-Zn, (000(1)over-bar)-O, (10(1)over-bar0), and (11(2)over-bar0) surfaces.* Surface Science, 2002. **519**(3): p. 201-217.

26. Woll, C., *The chemistry and physics of zinc oxide surfaces.* Progress in Surface Science, 2007. **82**(2-3): p. 55-120.

27. Kunat, M., et al., *Stability of the polar surfaces of ZnO: A reinvestigation using He-atom scattering.* Physical Review B, 2002. **66**(8): p. 3.

28. Kunat, M., U. Burghaus, and C. Woll, *Adsorption of hydrogen on the polar O-ZnO surface: a molecular beam study.* Physical Chemistry Chemical Physics, 2003. **5**(21): p. 4962-4967.

29. Duke, C.B. and A.R. Lubinsky, *Calculations of low-energy electron diffraction intensities from the polar faces of ZnO.* Surface Science, 1975. **50**(2): p. 605-614.

30. Overbury, S.H., et al., *Ion scattering study of the Zn and oxygen-terminated basal plane surfaces of ZnO.* Surface Science, 1998. **410**(1): p. 106-122.

31. Chang, S.-C. and P. Mark, *The crystallography of the polar (0001) Zn and (000-1)O surfaces of zinc oxide.* Surface Science, 1974. **46**(1): p. 293-300.

32. Sambi, M., et al., *An angle-scanned photoelectron diffraction study on the surface relaxation of ZnO (0001).* Surface Science, 1994. **319**(1-2): p. 149-156.

33. Galeotti, M., et al., *Structure of the ZnO(000) surface studied by X-ray photoelectron diffraction.* Chemical Physics Letters, 1994. **222**(4): p. 349-352.

34. Gopel, W., et al., *Angle-resolved photoemission from polar and non-polar zinc oxide surfaces.* Physical Review B, 1982. **26**(6): p. 3144-3150.

35. Girard, R.T., et al., *Electronic structure of ZnO(0001) studied by angle-resolved photoelectron spectroscopy.* Surface Science, 1997. **373**(2-3): p. 409-417.

36. Jedrecy, N., M. Sauvage-Simkin, and R. Pinchaux, *The hexagonal polar ZnO(0001)-(1 x 1) surfaces: structural features as stemming from X-ray diffraction.* Applied Surface Science, 2000. **162**: p. 69-73.

37. Wander, A. and N.M. Harrison, *The stability of polar oxide surfaces: The interaction of H[sub 2]O with ZnO(0001) and ZnO(0001-bar).* The Journal of Chemical Physics, 2001. **115**(5): p. 2312-2316.

38. Kresse, G., O. Dulub, and U. Diebold, *Competing stabilization mechanism for the polar ZnO(0001)-Zn surface.* Physical Review B, 2003. **68**(24): p. 15.

39. Becker, T., et al., *Interaction of hydrogen with metal oxides: the case of the polar ZnO(0 0 0 1) surface.* Surface Science, 2001. **486**(3): p. L502-L506.

40. Meyer, B. and D. Marx, *Density-functional study of the structure and stability of ZnO surfaces.* Physical Review B, 2003. **67**(3): p. 11.

41. Lindsay, R., et al., *ZnO(000(1)over-bar)-O surface structure: hydrogen-free (1x1) termination.* Surface Science, 2004. **565**(2-3): p. L283-L287.

42. Kotsis, K. and V. Staemmler, *Ab initio calculations of the O1s XPS spectra of ZnO and Zn oxo compounds.* Physical Chemistry Chemical Physics, 2006. **8**(13): p. 1490-1498.

43. Noguera, C., F. Finocchi, and J. Goniakowski, *First principles studies of complex oxide surfaces and interfaces.* Journal of Physics-Condensed Matter, 2004. **16**(26): p. S2509-S2537.

44. Egdell, R.G., T.J. Walker, and G. Beamson, *The screening response of a dilute electron gas in core level photoemission from Sb-doped SnO2.* Journal of Electron Spectroscopy and Related Phenomena, 2003. **128**(1): p. 59-66.

45. Christou, V., et al., *High resolution x-ray photoemission study of plasma oxidation of indium-tin-oxide thin film surfaces.* Journal of Applied Physics, 2000. **88**(9): p. 5180-5187.

46. Laukkanen, P., et al., *Electronic and structural properties of GaAs(100)(2x4) and InAs(100)(2x4) surfaces studied by core-level photoemission and scanning tunneling microscopy.* Physical Review B, 2005. **72**(4): p. 9.

47. Evans, D.A., et al., *Metal overlayers on the MBE-grown ZnSe(001) surface.* Applied Surface Science, 1996. **104**: p. 240-247.

48. Wilke, W.G., et al., *Surface Core level shifts on InP(110)- experiments and madelung energy calculations.* Physical Review B, 1989. **40**(14): p. 9824-9828.

49. Vos, M., S.G. Anderson, and J.H. Weaver, *Inelastic mean free paths for electrons at disordered interfaces.* Physical Review B, 1989. **39**(5): p. 3274-3278.

50. de Abajo, F.J.G., M.A. Van Hove, and C.S. Fadley, *Multiple scattering of electrons in solids and molecules: A cluster-model approach.* Physical Review B, 2001. **63**(7): p. 16.

51. Rodriguez, J.A., et al., *Chemical properties of Zn/S/Mo(110) and Co/S/Mo(110) surfaces: Reaction with hydrogen and formation of hydrogen sulfide.* Journal of Physical Chemistry, 1996. **100**(34): p. 14476-14484.

52. Bech, M., et al., *Copper nucleation on ZnO(11(2)over-bar0) in the presence of sulphur.* Surface Science, 2006. **600**(17): p. 3375-3381.

53. Jacobi, K., G. Zwicker, and A. Gutmann, *Work function, electron affinity and band bending of zinc oxide surfaces.* Surface Science, 1984. **141**(1): p. 109-125.

54. Yoo, Y.Z., et al., *S doping in ZnO film by supplying ZnS species with pulsed-laser-deposition method.* Applied Physics Letters, 2002. **81**(20): p. 3798-3800.

55. Zhou, P.L., et al., *Simple air oxidation synthesis and optical properties of S-doped ZnO microspheres.* Materials Letters, 2007. **61**(18): p. 3870-3872.

56. Schrier, J., D.O. Demchenko, and L.W. Wang, *Optical properties of ZnO/ZnS and ZnO/ZnTe heterostructures for photovoltaic applications.* Nano Letters, 2007. **7**(8): p. 2377-2382.

4. STUDY OF NICKEL GRAPHENE INTERFACES

This chapter is divided in five sections. The first section gives a brief introduction to the properties of graphene and methods for its fabrication. The second one gives an introduction to graphene on transition metal substrates. The third section discusses carbon phases on Ni surfaces, especially the Ni(111) substrate. The fourth section we present my results and discussion of my research on nickel-graphene interfaces. This section is further subdivided in four subsections (a) Growth and stability of graphene on Ni(111) surfaces (b) growth of graphene from surface carbide using STM (c) Growth and stability of Ni clusters deposited on graphene/Ni(111) substrate (d) One dimensional extended defect in graphene/Ni(111) substrate. In the final section we discuss the conclusions.

4.1 Introduction

Carbon plays a dominant role in chemistry and forms the basis of all organic chemistry. Elemental carbon exists in many allotropes: three-dimensional crystals (diamond, graphite), two dimensional graphene, one-dimensional nanotubes and zero-dimensional fullerenes. Graphene is a layer of sp^2 bonded carbon atoms arranged in a hexagonal lattice. It is the building block for other graphitic materials; it can be stacked to form 3D graphite, it can be rolled to form 1D nanotubes and wrapped to form 0D fullerenes (sp^2 bonded C atoms arranged in hexagons and pentagons). Graphene had been studied theoretically for long time and was predicted to have exciting electronic properties with the electrons behaving as massless Dirac fermions. However, graphene

was also predicted to be unstable in a free state, because at finite temperatures thermal fluctuations would destroy any long-range correlation in one or two dimensions [1-4]. In 2004 a group of physicists from Manchester University, led by A. Geim and K. Novoselov found a way to extract a single layer of atoms from graphite [5]. They developed a technique called “micromechanical cleavage” to extract single sheets of atoms from three dimensional crystals of graphite, which is made of layers of graphene weakly bound together by van-der- Waals forces. Then simultaneous but independent observation of the quantum Hall effect from Andre Geim´s and Philipp Kim´s groups confirmed that the charge carriers in graphene are indeed massless Dirac fermions [6, 7]. The experimental isolation of free standing monolayer graphene and its novel transport properties led to an explosion of interest in graphene. There have been several reviews on graphene [1, 8, 9]. Next we will briefly discuss some of graphene’s exotic properties.

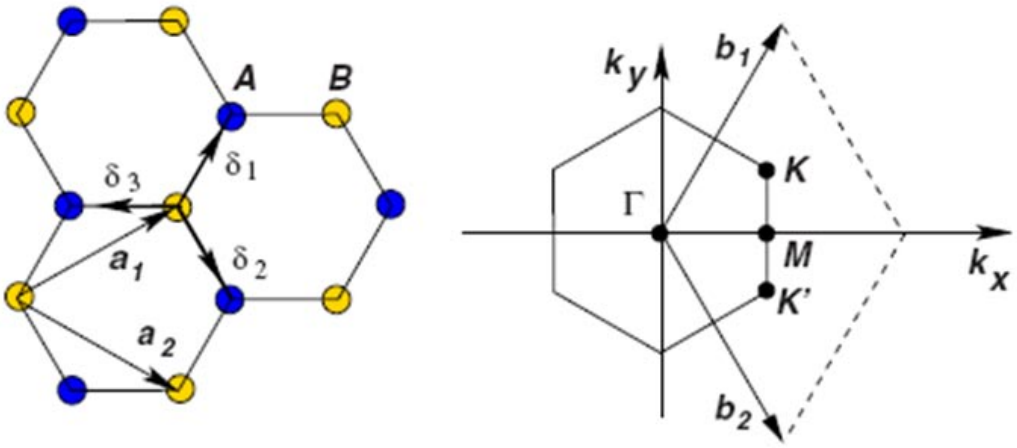

Figure 4.1: Honeycomb lattice and its Brillouin zone. Left: lattice structure of graphene, made out of two interpenetrating triangular lattices (a_1 and a_2 are the lattice unit vectors, and δ i, i=1,2,3 are the nearest-neighbor vectors).Right: corresponding Brillouin zone. The Dirac cones are located at the K and K' points. Figure is taken from Ref[8].

4.1.1 Graphene atomic and electronic properties

Graphene is made out of carbon atoms arranged in a hexagonal structure, as shown in Figure 4.1 [8]. The structure can be seen as a hexagonal lattice with a basis of two atoms per unit cell. The lattice vectors can be written as

$$a_1 = \frac{a}{2}\left(3, \sqrt{3}\right), a_2 = \frac{a}{2}(3, -\sqrt{3}) \quad (1)$$

where a=1.42 Å is the carbon-carbon distance . The reciprocal-lattice vectors are given by

$$b_1 = \frac{2\pi}{a}\left(1, \sqrt{3}\right), b_2 = \frac{2\pi}{a}(1, -\sqrt{3}) \quad (2)$$

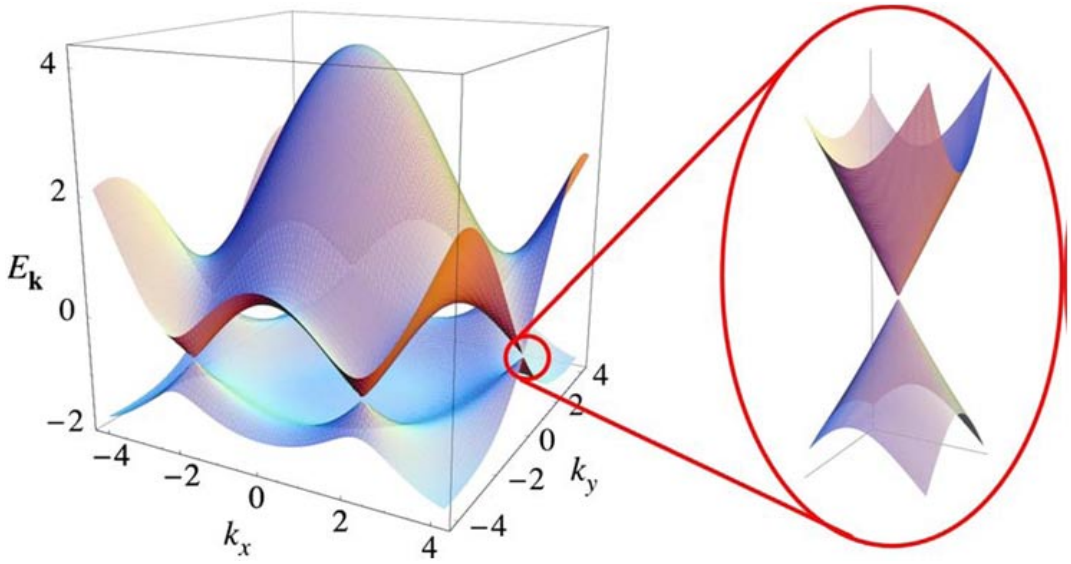

Figure 4.2: Band structure of graphene in the first Brillouin zone. The lower and upper bands represent π and π* bands respectively. The zoom section shows the linear bands dispersion of the π bands at the K point. Figure is taken from Ref[8].

Of particular importance for the physics of graphene are the two points *K* and *K´* at the corners of the graphene Brillouin zone (BZ). The electronic dispersion around these six points is observed to be isotropic and linear in momentum, given by

$$\varepsilon(q) = \pm v_F q \quad (3)$$

Where q is the momentum and v_F is the Fermi velocity. This equation resembles the energy of Dirac electrons given by

$$\varepsilon(q) = \pm\sqrt{m^2c^4 + c^2q^2} \quad (4)$$

where m=0 and c= v_F. In this sense the electrons near the K points in graphene behave as massless Dirac particles and therefore the K points are also named Dirac points as the electrons can be described by the Dirac equation for relativistic particles. Most of the interesting properties of graphene are related to linear band dispersion at the *K*-point on the edge of the Brillouin zone. An immediate consequence of this massless Dirac-like dispersion is a cyclotron mass that has a square root dependence on the electronic density given as

$$m^* = (\sqrt{\pi}/v_F)\sqrt{n} \quad (5)$$

Where n is the electron density and v_F is the Fermi velocity. In a traditional two-dimensional system the cyclotron mass is constant, independent of the electron density. Another interesting effect characteristic of Dirac electrons is the Klein paradox. This effect refers to the possibility that massless Dirac electrons can propagate through a potential barrier with probability one. The experimental demonstration of Klein tunneling was recently achieved [10]. For a detailed review on this see Ref [11].

The electronic band structure is also responsible for different phenomena occurring in electrical measurements in graphene. These are the minimum conductivity, classical and quantum Hall effect and phase coherent phenomena, namely weak localization and universal conductance fluctuations [6]. Half- integer quantum Hall effect is based on the regular quantum hall effect with a non-zero Berry's phase [6]. This non-zero Berry's phase is the proof for the actual existence of Dirac type charge carriers. In

addition to these exotic properties of graphene that arise from its special electronic structure, graphene has also attracted a lot of attention from the application side. Being only a single atomic layer thick graphene is the ultimate nano-material. Prospects of large 'wafers' of graphene has opened speculations of using it to write structures and devices in it. Unlike its 'cousin', the carbon nanotube, the perceived advantage is that no elaborate techniques need to be designed to position these nanomaterials but instead graphene wafers can be patterned with similar lithography methods that are so extremely successful in microelectronics industry today. While the fabrication of microelectronics devices in graphene is still a long way off, concrete applications such as transparent electrodes for touch screen applications are very close to commercial use [12]. In the following we describe some materials science aspects that have enabled the fast development of graphene and that are the motivation of our studies.

4.1.2 Graphene synthesis methods

Graphene can be synthesized by different methods. The most common methods of graphene synthesis are (1) micromechanical cleavage, (2) thermal decomposition of SiC, (3) chemical methods, (4) segregation of carbon, and (5) decomposition of hydrocarbons. Each method has its own advantages and disadvantages. Here we will briefly describe each method.

4.1.2.1 Micromechanical cleavage

This method is often referred to as a scotch-tape technique, which relies on the weak van der Waals force between graphite layers. Novoselov et al. isolated graphene flakes from a commercially available highly oriented pyrolytic graphite (HOPG) [5].

They prepared many 5 μm deep mesas by dry etching in oxygen plasma. This structure was then put on a photoresist and baked, to stick the mesas to the photoresist. Then, a scotch tape was used repeatedly to peel off layers from the graphite sheet. Thin flakes, attached to the photoresist, were released in acetone. These flakes were transferred to a Si substrate, and were found to have single- to few layer graphene sheets. Therefore exfoliation is basically a repeated peeling process. Exfoliated graphene shows superior electronic and transport properties compared to all other synthesis methods. However, this method is not practical for large scale manufacturing.

4.1.2.2 Thermal decomposition of SiC

The growth of graphene on silicon carbide (SiC) surfaces by high temperature annealing in vacuum has been proposed as a route for large-scale production of graphene-based devices [2, 13, 14]. Thermal decomposition of SiC has an advantage that SiC substrates are insulating, so transfer to another insulator is not required. Therefore it is more likely they can be integrated with the existing microelectronic technologies. However, graphene synthesized on silicon carbide is not very uniform and of high quality. SiC has two polar faces, corresponding to a Si terminated face (0001) or a C terminated face (000-1). The graphene growth mechanism is quite different on either face. On the Si-terminated (0001) basal plane, vacuum annealing leads to small graphene domains typically 30-100 nm in diameter, whereas on the C-terminated (000-1) face, larger domains (200 nm) of multilayered, rotationally disordered graphene have been produced [15]. However it is difficult to control graphene thickness with this method. Recent experiments of synthesizing graphene ex situ (i.e. non ultrahigh-vacuum conditions) have shown promising results in controlling film thickness [16]. Another

major disadvantage of this method is the high cost of production for SiC wafers, their limited size compared to silicon wafers, and the high processing temperatures well above current CMOS limits. Graphene obtained on SiC single crystals has good mobility, but this material may be limited to devices on SiC only, since transfer to other substrates such as SiO_2/Si has not been demonstrated yet and might be difficult [17]. For more information on epitaxial graphene on SiC see Ref [18-20].

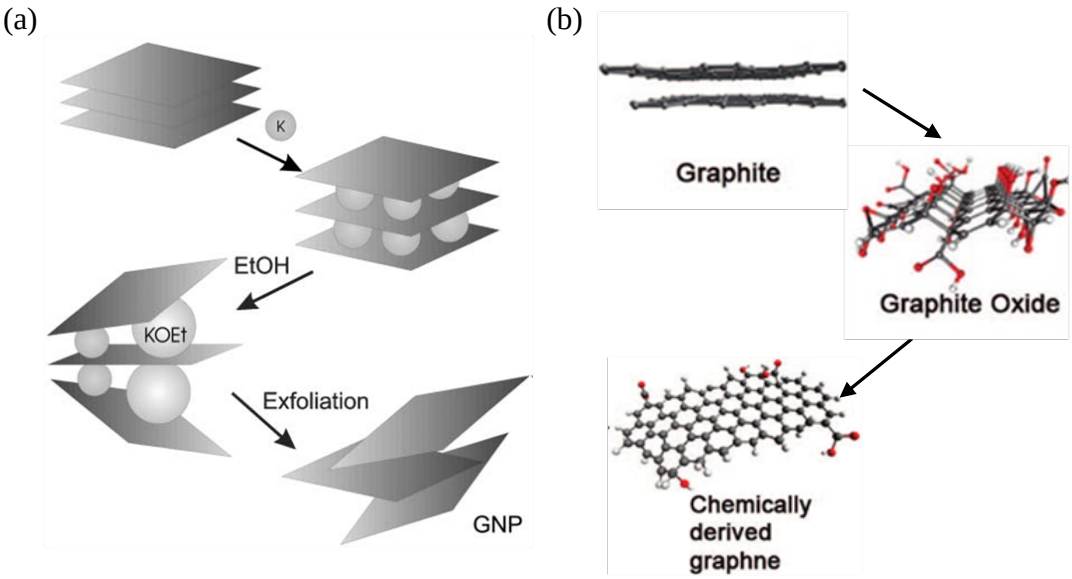

Figure 4.3: (a) Schematic diagram showing the intercalation and exfoliation process to produce graphite nanoplatelets (GNP). (b) Schematic diagram showing the conversion process from graphite to chemically derived graphene. Figures are taken from Ref [1].

4.1.2.3 Chemical methods

Graphene can be synthesized by chemical means from graphite intercalation compounds and colloidal suspensions made from graphite, derivatives of graphite (such as graphite oxide) [1, 21]. Viculis et al. showed that thin graphite nanoplatelets can be formed by separating the graphite layers through intercalation with alkali metals followed by exfoliation with aqueous solvents [22]. They used potassium metal to intercalate a

pure graphite sheet and then exfoliate it with ethanol to form dispersion of C sheets (see Figure 4.3(a)). During sonication, the exfoliated nano-carbon sheets or graphitic nanoplatelets are formed.

In 2006, Ruoff and his coworkers demonstrated a solution-based process for producing single-layer graphene by chemical modification of graphite to produce a water dispersible graphite oxide [23]. This method uses 'oxidation–exfoliation–reduction' approach as shown in Figure 4.3(b) [24]. The graphene basal planes in graphite are first decorated with covalently bonded oxygen functional groups. This oxygenated graphite or graphite oxide is hydrophilic and water intercalates between the graphene oxide sheets. It readily exfoliates into single graphene oxide sheets through addition of mechanical energy (i.e. sonication) and dispersed as individuals sheets in aqueous solutions. These oxide sheets can then be reduced by thermal annealing or by chemical reducing agents. The advantage of this method is its low-cost and massive scalability. A disadvantage of this method is it also creates a large number of defects during the reduction step.

4.1.2.4 Segregation of carbon

Epitaxial graphene on transition metal and transition metal carbides have been known since long time [25-29]. Graphene layers on metals have been prepared by surface segregation of carbon-the samples are first doped with carbon (by keeping the sample in a CO atmosphere or in contact with graphite powder at elevated temperatures), then annealed to high temperatures which produce carbon segregation to the surface on cooling. If the concentration of bulk carbon is high enough then a single layer of graphene can nucleate and grow from the carbon segregating from the bulk during cooling. Higher concentration of bulk carbon can result in additional carbon being

expelled or precipitated from the bulk during cooling giving rise to multilayer graphene. It has been shown that controlled growth of monolayer of graphite can be achieved on metal substrates held at high temperatures with equilibrium segregation process [30, 31]. However non equilibrium carbon precipitation during cooling can give rise to multiple layers of graphene. For metals with high solubility of carbon (like Fe, Ni) multiple layers of graphene are formed easily than compared to metals with low solubility (like Pt, Ir). Multiple layers of graphene formed by precipitation of carbon can be suppressed by using a optimum cooling rate or using thin metal films as substrate [32].

Graphene on Ni is usually grown by dissolution of carbon in the bulk at ~ 1000°C then followed by segregation to the surface [33]. The amount of carbon doping in Ni sample depends on the solubility of carbon in nickel, which can be determined from Ni-C phase diagram [34]. In the equilibrium state, the carbon solubility in nickel at a eutectic temperature of 1319°C is ~2.7 at %. Recently Saenger et. el. showed that graphitic carbon is produced both during heating and cooling of amorphous C/Ni bilayers [35]. Their x-ray diffraction (XRD) measurements showed graphitic carbon formation beginning during heating at temperatures T of 640–730 °C where carbon solubility in Ni is still low. Therefore they concluded that graphitization occurs by direct metal-induced crystallization, rather than by a dissolution/precipitation mechanism in which C is dissolved during heating and expelled from solution upon cooling.

4.1.2.5 Thermal decomposition of hydrocarbons

Graphene on metal substrates can also be synthesized by decomposition of hydrocarbons. The hydrocarbon molecules are either adsorbed at room temperature, after which the samples are annealed to decompose the molecules and desorb the hydrogen, or

the molecules are directly adsorbed on the hot samples where it decomposes and hydrogen desorbs. The surface of the metal acts as a complete dehydrogenation catalyst, so the reaction stops after a monolayer of graphene is formed. For the decomposition method mostly ethylene is used, but propene, methane, acetylene, CO, and larger hydrocarbon molecules are also used. For the thermal decomposition method quality of the graphene film depends on the temperature of the substrate and the amount of hydrocarbon exposure. For this method to be operational transition metal catalysts with small carbon solubility are used so that the carbon remains at the surface. Typical materials for which this self-limiting graphene-monolayer growth applies are Cu and Ir. For metals with high solubility (like Ni) however this method cannot be fully separated from the carbon segregation method. While Ni is a good dehydrogenation catalyst the produced carbon diffuses easily into the bulk. Therefore there is no self-limiting graphene formation, but rather carbon dissolved in the bulk re-segregates to the surface when graphene grows (see our discussion in section 4.3.2.)

Most applications require graphene on an insulating substrate and so graphene grown on a metal must be transferred to another appropriate substrate or processed in some other way. In this case, etching of the underlying metal substrates allows the graphene films to be transferred to other substrates. Etching of Cu, Ni and Ru is relatively straightforward however wet etching of Ir is extremely difficult. Most of the methods of transferring graphene films on insulating substrates have used disposable PMMA or PDMS films [36, 37]. Recently Bae et al. reported the roll-to-roll production of predominantly monolayer 30-inch graphene films grown by high pressure CVD onto flexible copper substrates [12]. Their method has three essential steps: (i) adhesion of

polymer supports to the graphene on the copper foil; (ii) etching of the copper layers; and (iii) release of the graphene layers and transfer onto a target substrate.

4.2 Epitaxial graphene on metal substrates

Epitaxial graphene was first observed on Pt single crystal substrates in the 1960's [38-40]. During sample preparation carbon impurities segregate from the bulk to the surface, forming graphitic layers which consist of few layer or monolayer graphene. The recent explosion of research in graphene has led to resurgence of interest in graphene on metal substrates. Graphene on metals is a viable route of growing large areas of high quality graphene with few defects. Graphene layers on metal surfaces have been prepared by two methods, by segregation of bulk-dissolved carbon to the surface, and by surface decomposition of carbon-containing molecules (discussed in section 4.1).

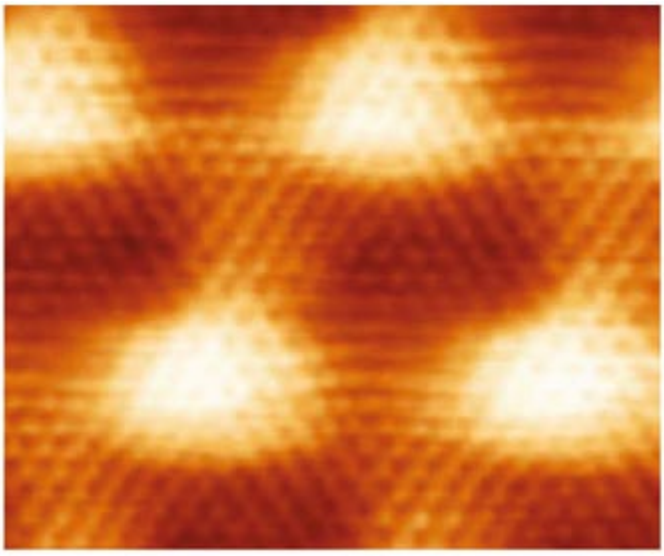

Figure 4.4: Atomically resolved STM image of the Moiré structure of graphene on Ru(0001).Figure is taken from Ref[35].

Graphene has been studied the most on Pt(111), Ir(111), Ru(0001), and Ni(111) substrates [29]. Moiré patterns are observed on most of the metal substrates due to large lattice mismatch between graphene and fcc or hcp metal substrates. Ni(111) and Co(0001) are exceptions where they form (1x1) structures because of small lattice mismatch of less than 2% [41, 42]. The rotation of two hexagonal lattices with close lattice match gives rise to a hexagonal superstructure or Moiré patterns. STM images of the Moiré structures of the hexagonal systems display typical patterns with large unit cells. A typical STM image of a Moiré pattern on Ru(0001) substrate is shown in Figure 4.5.

The graphene/metal interfaces are also considered a model system to investigate interaction between graphene π-bands and the metal bands. This is relevant for making contacts between graphene and metal electrodes. The charge transfer between graphene and the metal substrate modify the band structure of graphene by opening a band gap. Thus epitaxial graphene grown on metal surfaces is doped either with electrons or holes. The amount of doping or charge transfer depends on the difference between metal and graphene work functions. The interaction between graphene and the metallic substrate depends on the type of substrate. The interaction of graphene with metals can be subdivided into strong and weak interaction. The stronger the interaction between graphene and the metallic substrate, the larger is the charge transfer. The characteristic electronic structure of graphene is significantly altered by chemisorption on Co, Ni, and Pd, but is preserved by weak adsorption on Al, Cu, Ag, Au, and Pt. In case of chemisorption graphene is strongly bonded to the surface, so it is closer to the metallic

surface. The separation between graphene layers in a graphite crystal 3.35 Å while the separation between graphene and the Ni(111) substrate is 2.11Å.

Ni is widely used as a graphene substrate material due to its excellent lattice match and ease of etching for transfer to other substrates. For these reasons we also chose Ni as the material for our studies. Before we describe our results, I briefly review previous experimental results of graphene on Ni substrates.

4.3. Carbon on Ni surfaces

The interaction of carbon with Ni surfaces is extremely important for catalysis applications. In both the steam reforming of methane and the CO methanation reaction, different carbon phases have been identified on the Ni-based dispersed catalysts [43-47]. Carbon on metal surfaces can exist in several states or surface phases, i.e., adsorbed atoms, surface carbide, graphene and graphite [48]. The carbon phases can be distinguished on the basis of their line shape in Auger electron spectroscopy and energy electron loss spectroscopy [49-51]. Surface carbon can experience phase transformations, passing from one phase to another. In the methanation reaction, *carbidic* carbon forms at temperatures < 600 K and is the active carbon species participating in the catalytic process. At temperatures beyond 700 K, *graphitic* carbon forms which results in a loss of reactivity to hydrogen and therefore leads to a poisoning of the catalyst. The carbon nickel system has been studied by many groups. Some of them prepared carbon on transition metal surfaces by segregation of carbon from bulk while others used decomposition of hydrocarbons or carbon monoxide. I will briefly discuss some surface science studies of carbon nickel system prepared by both methods.

The segregation and precipitation behavior of carbon-saturated Ni-crystals has been thoroughly studied by Blakely and co-workers more than 30 years ago [52-54]. Shelton et. al. carried out some experimental studies of carbon segregation on the Ni(111) surface containing 0.3 atomic % carbon [53]. They doped Ni sample with carbon by holding the sample in a quartz capsule filled with graphite powder at high temperatures. Three phases of carbon were observed on Ni(111) saturated with carbon. At high temperatures T > 1180K carbon was present in a dilute phase as chemisorbed atoms with very low coverage (Phase A). Cooling the crystal below T<1180K results in segregation of carbon atoms as monolayer of graphene (MG) to the surface (Phase B). This surface layer is identified as an equilibrium segregated phase. Cooling further below T<1065K causes carbon precipitation and formation of multilayer graphitic carbon (Phase C). An abrupt reversible transition occurs from Phase A and Phase B and the transition temperature is a function of carbon doping level and is ~ 1000K for a crystal containing ~ 0.15 atomic % carbon [52]. Eizenberg and Blakely also studied carbon segregation behavior on surfaces vicinal to (111) and on the (311) and (110) planes [30]. Here also they observed an abrupt segregation of a graphitic monolayer similar to the Ni(111) surface. For the (100) and (210) monolayer graphite condensation was observed but the high temperatures carbon was characterized by carbidic lineshape in AES spectra. Hamilton and Blakely also investigated carbon segregation behavior on Pt, Pd and Co single crystal surfaces [31]. For Pd(l00), Pd(111) and Co(0001), they observed carbon segregation with evidence for a surface phase transition of the type previously reported for Ni(111). The surface segregation and precipitation mechanism of epitaxial graphite layers on carbon doped Ni(111) were also investigated by XPS by Fujita and Yoshihara

[55]. They also verified the three phases of carbon present in Ni(111) as shown by Blakely et. al.

Interaction of hydrocarbons and CO with low index Ni surfaces has been studied with different techniques [56-66]. Goodman and co-workers used Auger analysis to identify two types of carbon species after the reactions of carbon monoxide and ethylene on Ni(100) at 600 K [64]. Rosei et al. measured the structure of graphitic carbon on Ni(111) by surface extended energy loss fine structure (SEELFS) [49]. They also studied the electronic property of carbidic and graphitic overlayers on Ni(111) using photoemission, energy loss and ionization loss spectroscopic techniques [67]. Nakamura and his coworkers investigated carbide formation on Ni(111) using CO and C_2H_4 as the carbon source, by STM, AES and LEED [56, 57]. They showed that the growth mode of carbide islands on Ni(111) was different depending on whether CO or C_2H_4 was used-carbide growth started at step edges (terrace sites) on Ni(1 1 1) for CO (C_2H_4). Usachov et. al. investigated structure of graphene on the Ni(111), (110), (755),and (771) single-crystal surfaces with STM [68]. Laegsgaard and his coworkers investigated 'clock reconstruction' induced by surface carbide formation on Ni(110) and Ni(111) by scanning tunneling microscopy (STM) [59, 61, 62]. They showed that on both surfaces carbide phase is formed with 0.2–0.6 ML carbon coverage. For higher coverages the graphitic phase was stable. In summary, ordered carbon species on Ni are characterized as either carbidic or graphitic, with the carbidic form being the catalytically active species. On all the surfaces of Ni the carbides were prepared at an intermediate temperature between 400 and 700 K; the graphitized surfaces were obtained by heating the carbide layers to 700 K and above.

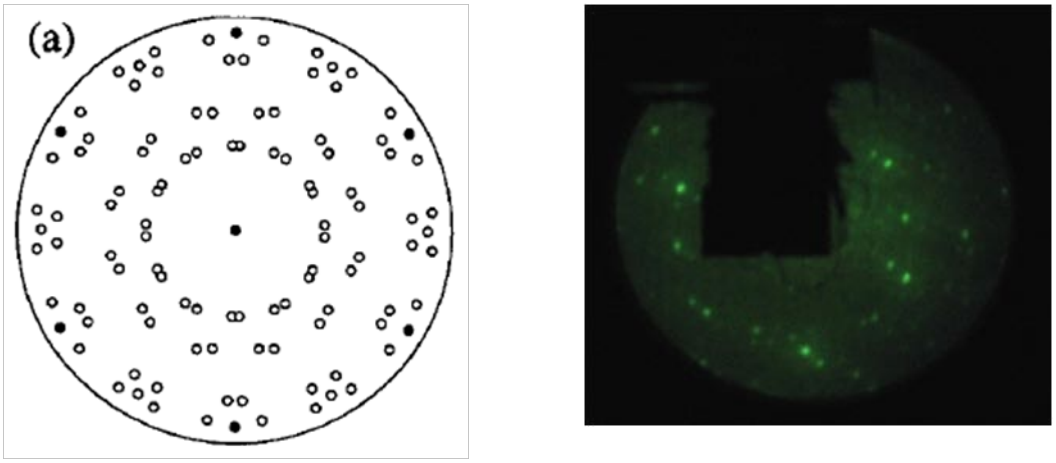

Figure 4.5: (a) Schematic LEED pattern at primary energy 50 eV from the carbidic phase on Ni(111). The pattern is generated by the nearly quadratic ~ 5 x 5 $Å^2$ surface mesh. Filled and open circles are Integer and Fractional order spots respectively. Figure is taken from Ref[55]. (b) LEED pattern of carbide taken with primary energy of 62 eV.

4.3.1 Carbide on Ni(111)

Carbide on Ni(111) has a very complicated structure. A schematic LEED pattern for the surface carbide on Ni(111) is shown in Figure 4.5(a). The main features of this a LEED pattern are 12 groups of five spots, situated close to a circle through the lowest integer order beams. This pattern is characteristic of the carbidic phase on Ni(111) and indicates that six rotational domain of the carbidic phase are present on the surface. McCarroll et al. produced the carbidic phase by exposure to ethylene (C_2H_4) and concluded that the diffraction pattern can be explained by assuming that the surface had transformed into a slightly distorted ~ 5 x 5 $Å^2$ square structure with a coincidence cell given by $\begin{vmatrix} 7 & 2 \\ 2 & 7 \end{vmatrix}$ in matrix notation or $\sqrt{39}R16.1^o \times \sqrt{39}\bar{R}16.1^o$, where $\bar{R}$ denotes

rotation in the opposite sense to R [69]. Hirano et al. and Nakamura et.al studied the catalytic activity of Ni(100) and Ni(111) surfaces for the methanation reaction of CO [70, 71]. They accidentally obtained a single-domain carbide on a Ni(111) surface by the segregation of carbon which allowed them to deduce the structure of the carbide overlayer on the Ni(111) surface which was the same as proposed by McCarroll. They showed that the carbide overlayer on Ni(111) has exactly the same arrangement of carbon atoms as that of the (2 × 2)p4g structure on the Ni(100) surface. The reconstruction of Ni(100) on formation of carbide is also known as clock reconstruction. Similarly the Ni(111) surface undergoes reconstruction into a Ni(100) type surface with the density of Ni atoms in the topmost layer reduced by ~10%. A schematic diagram of the clock reconstruction of carbide on Ni(111) is shown in 4.7(a). Ni atoms rotated clockwise and anti-clockwise by ~ 15 ° around the C atoms which form a quadratic mesh. As shown in Figure 4.7(b), this mesh is tilted by ~ 3 ° relative to a close-packed (110) direction in the underlying substrate. The coincidence cell $\begin{vmatrix} 7 & 2 \\ 2 & 7 \end{vmatrix}$, is almost square, with side lengths of ~15.5 Å and with angles of ±16.1 ° to close-packed (110) directions in the Ni(111) layer underneath.

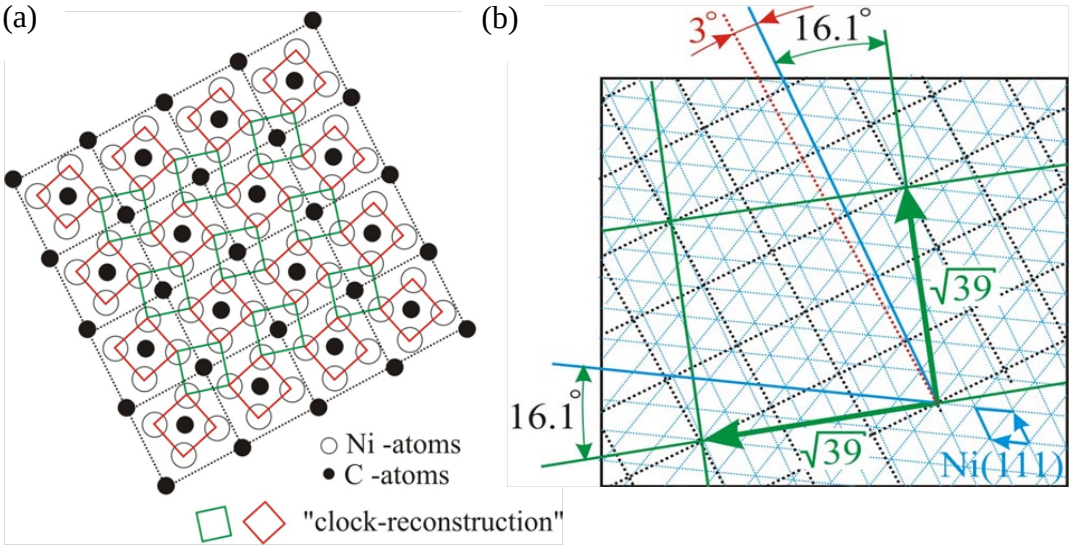

Figure 4.6: (a) A schematic model of the clock reconstructed carbide structure on Ni(111) surface with squares of Ni atoms rotated clockwise and anti-clockwise by ~ 15 ° around the C atoms which form a quadratic mesh. A c(2 x 2) cell of the carbon atoms is shown as well. (b) The (√39 R16.1° ×√39 Rbar16.1°) unit cell relative to the Ni(111) unit cell. This large unit-cell, indicated in green, is a consequence of the coincidence structure of a quasi-square Ni_2C lattice (black dashed lines) with the hexagonal Ni(111) substrate (blue lines).one axis of the Ni_2C clock-structure is rotated by 3° relative to the <1-10> direction of the Ni(111) substrate.

4.3.2 Graphene on Ni(111)

Nickel has an fcc structure with lattice constant 3.51 Å .The lattice misfit between Ni(111) and graphene is less than 2%. Carbon can adsorb on top site, bridge site or the two inequivalent hollow sites, the fcc site and hcp site (directly above Ni atoms in the second and third substrate layers, respectively). Three possible adsorption geometries are possible, which will give rise to a (1x1) LEED pattern. In the first model (Figure 4.7(a)), all carbon atoms are located at the three-fold hollow sites. In the second model (Figure 4.7(b)), one carbon is located at the on-top site of the topmost Ni atoms, while another exists at the hcp hollow site. In the last model (Figure 4.7(c)), two carbon atoms of the unit cell are situated either at the on-top site or at the fcc hollow site. There has been

some debate regarding which of these structures is the most energetically stable.

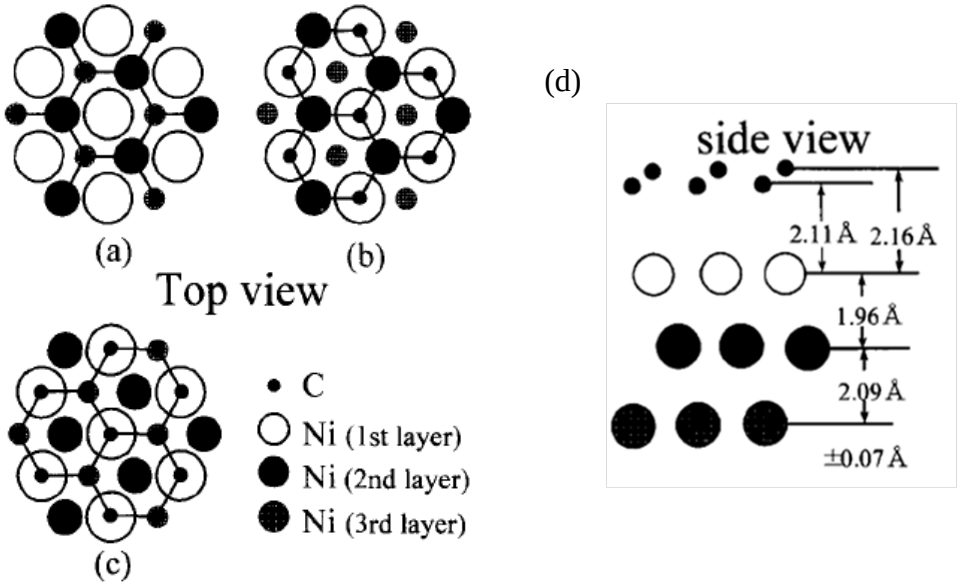

Figure 4.7: Top view of different adsorption geometries of graphene on Ni (111) (a) hcp-fcc, (b) top-hcp and (c) top-fcc. (d) Side view of graphene nickel interface for top-fcc model. Figures are taken from Ref[66].

From SEELFS experiments Rosei et. al concluded that the carbon atoms occupy the hollow sites (fcc and hcp) and calculated carbon-Ni distance of graphene/Ni(111) to be 2.8 Å, which is smaller than the interplanar distance in graphite [49]. Klink at. al. concluded from STM measurements that carbon atoms in graphene on Ni(111) occupy fcc and hcp hollow sites [60]. Gamo et. al, on the other hand, concluded from LEED I-V analysis that the most stable structure of graphene is with half the carbon atoms on top site and the other half on fcc hollow site [72]. They calculated the MG-Ni distance between the first layer to be 2.11 Å (see Figure 4.7(d)). This was confirmed by Li^{+}-Impact Collision Ion Scattering Spectroscopy (ICISS) measurements for Graphene/ Ni(111) surface by Kawanowa et al.[73]. They show that the C atoms are located on top

and fcc hollow sites, and the spacing between MG and Ni is 0.21nm. The atomic and electronic structure of the MG/Ni(111) interface was calculated by Bertoni et al. using density functional theory [74]. They found the most stable structure is where carbon atoms are on top and fcc hollow sites, in agreement with LEED I-V and ICISS experimental conclusions. They also found that the electronic structure of the graphene layer is strongly modified by interaction with the substrate and the magnetic moment of the surface nickel atoms is lowered in the presence of the graphene layer. DFT calculations by other groups have also shown the stable structure to be on top-fcc and the distance between C-Ni to be ~ 0.21 nm [75, 76]. Recent DFT analysis though have concluded that a bridge/top configuration was the most stable structure for graphene on Ni(111) [77].

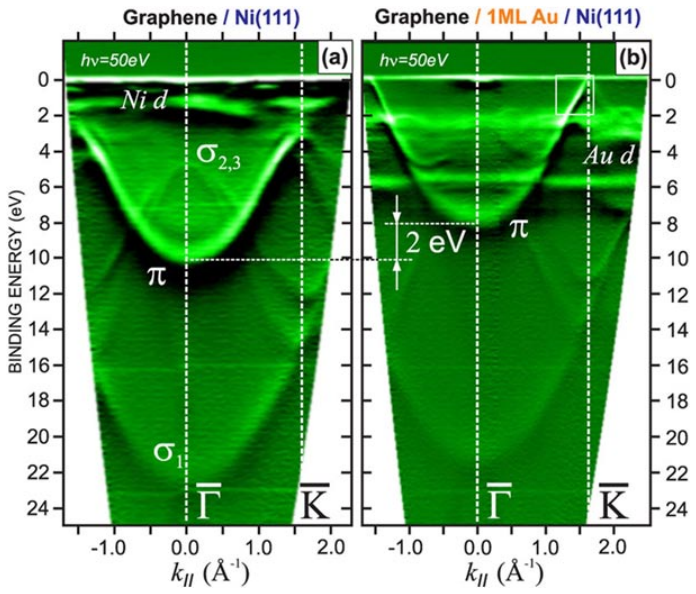

Figure 4.8: Electronic structure of graphene on Ni(111) along $\overline{\Gamma K}$ (a) before and (b) after intercalation with 1 ML Au leading to a 2 eV shift and the closing of the gap at $\overline{K}$.Figure is taken from Ref[73].

Graphene grown epitaxially on Ni(111) has an electronic structure quite different to free standing graphene. The p_z orbitals of graphene hybridize with the Ni 3d orbitals, as both of them are perpendicular to the surface. As a result some charge is shifted from the 3d band into the empty π^* states of graphene, causing an energy shift of the π bands. The σ bands are less affected because of the geometry of the orbitals and their energy position with respect to the Ni 3d band. This charge transfer from Ni 3*d* and C $2p_z$ orbitals create a surface dipole with its negative side facing the vacuum. The π band of the adsorbed graphene is shifted upward to lower binding energy (i.e. the orbitals shift closer to the Fermi level) by more than 2 eV [78]. The σ bands are also downshifted, but by less than1 eV. The opening of the band gap can also be explained from symmetry arguments. The two carbon atoms of the graphene unit cell are located at nonequivalent positions on the Ni(111) substrate, one on top of nickel atom and the other in the hollow site, which removes the symmetry of the sublattices, thus creating a band gap.

4.4 Results and Discussion

In this section we discuss our results on graphene research. The results and discussions section are divided into four subsections. In the first subsection we discuss the growth and stability of graphene on Ni(111) substrate. In the second we present the results of graphene growth from surface carbide phase on Ni(111) substrate using STM measurements. In the third subsection we discuss the results of our investigations on the effect of annealing Ni clusters deposited on MG/Ni(111). In the fourth subsection we discuss our observation of novel extended line defect on MG/Ni(111). Finally we summarize the results of these experiments.

4.4.1 Growth and stability of graphene on Ni(111) substrate

Growth of graphene on Ni(111) under UHV conditions has been studied before [66, 67, 72, 79-82]. Exposing a clean Ni(111) surface to hydrocarbons either yields a surface carbide or graphene. The surface-carbide phase forms upon thermal decomposition of hydrocarbons at low temperatures while graphene generally forms at higher temperatures between 500- 700 °C. Recent time-dependent x-ray photoemission (XPS) studies showed that graphene grows on a clean Ni(111) surface, i.e. in the absence of a carbide (25). Here we re-examine these growth scenarios with specific focus on the interplay between carbide and graphene growth on Ni(111) surface. We find that graphene is thermodynamically favored surface termination of Ni below 650 °C. At higher temperatures, carbon is dissolved into the bulk forming a clean Ni(111) surface. At temperatures below 480 °C surface carbide growth dominates over formation of graphene. However, once the carbide is destabilized graphene may grow below 480 °C as well. We also demonstrate that the formation of this ordered surface-carbide substantially influences the graphene formation and thus makes nickel a special case compared to other graphene forming transition metals that do not exhibit a similar surface carbide phase.

Carbide or graphene surfaces were formed by exposing the Ni(111) surface by decomposition of ethylene in an ultrahigh vacuum (UHV) chamber. At a sample temperature below 480 °C, surface carbide is formed. This carbide is identified by LEED as well as by Auger electron spectroscopy (AES). AES was used to discriminate between graphene and a surface carbide layer. This is possible because the carbon KVV AES line has very characteristic and distinct shapes for both sp^2 hybridized carbon and carbidic

carbon [43, 83-87](see section 2.3). Figure 4.9 shows this C-KVV line for the surface carbide and a graphene monolayer. In addition to the distinct line shapes for the different carbon species, their intensity also reflects the difference in carbon concentrations in carbide and graphene monolayers. For graphene there are two carbon atoms per Ni-atom, i.e. a graphene layer has the equivalent of 2 monolayers (ML) of carbon, where 1 ML corresponds to the number of Ni-atoms in a Ni(111) plane. In contrast, the surface carbide phase contains only 0.5 ML of carbon.

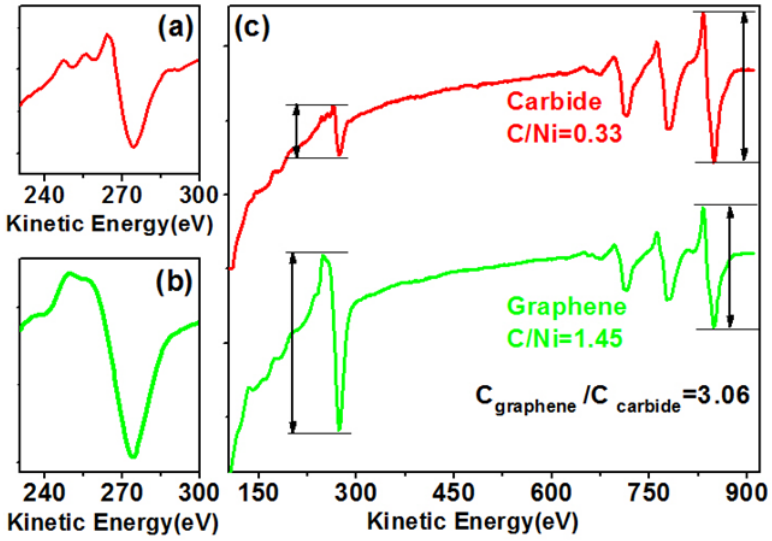

Figure 4.9: Auger electron spectra of monolayer carbide and monolayer graphene on a Ni(111) surface. (a) and (b) show the carbon-KVV Auger peak for carbide and graphene, respectively. (c) shows the carbon peak intensity in relation to the Ni-LMM peaks for carbide and graphene.

Above 480 °C the phase stability temperature for the surface carbide is reached and the carbide dissolves, forming a clean Ni(111) surface. Keeping the sample above 480 °C in vacuum eventually results in the nucleation and growth of graphene on pure Ni. This nucleation and growth process can be monitored by AES as shown in Figure

4.10(a), which shows the time sequence of Auger spectra during annealing to 480 °C in UHV of a sample initially exhibiting a surface carbide phase. Upon annealing, the carbide Auger signal almost immediately disappeared forming a clean Ni(111) surface. After some time delay a carbon signal reappears. However, the reemerging carbon signal is from sp^2 carbon. This carbon signal increases slowly with time and eventually saturates as a complete monolayer of graphene was formed. Figure 4.10(b) shows the intensity evolution of this carbon signal as a function of time. The absence of carbide signal during the growth indicates that graphene grows on clean Ni(111) in agreement with a recent XPS study [88].

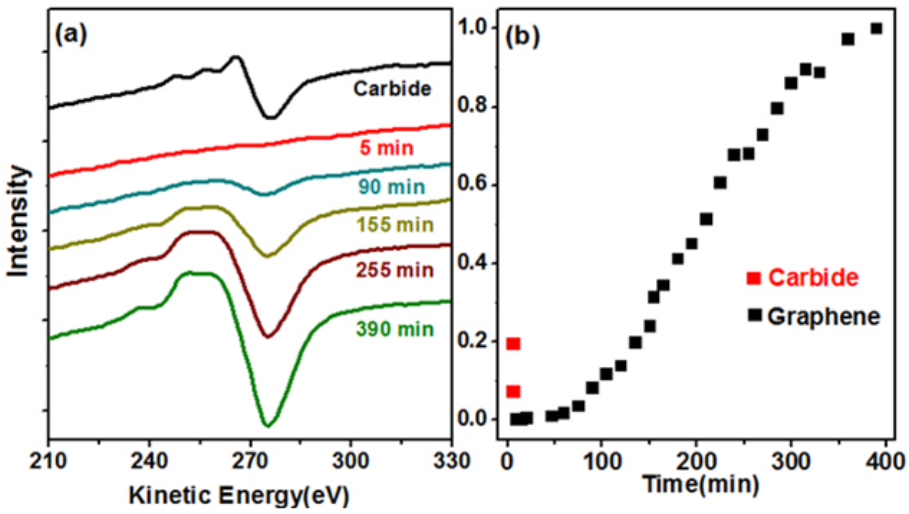

Figure 4.10: Time evolution of the carbon peak after annealing of a carbide-covered surface to 480 °C. (a) shows the C-KVV peak for the carbide and for different time periods after raising the temperature to 480 °C. In (b) the change in the peak intensity is plotted versus time. After raising the temperature the carbide C-KVV peak disappears almost immediately and graphene is formed after some time period after ~400 min the entire surface is covered by monolayer graphene.

The carbon peak intensity in AES is proportional to the area covered by graphene and therefore the change in intensity indicates the graphene growth rate. It is evident that

initially the growth rate increases, suggesting that the growth rate scales with the circumference of the graphene grains. In other words, the growth rate is determined by the attachment of carbon to the graphene and not by the rate of carbon segregation to the surface. This is in agreement with studies on other transition metal surfaces that indicate a significant barrier for carbon attachment to graphene sheets on top of the metal [89, 90]. Thus in a temperature range of 480 °C to ~ 700 °C graphene grows on Ni in a similar growth mode as on other transition metals.

Annealing the sample continuously at 400 °C in vacuum after carbide formation can result in one of two scenarios that are difficult to control. Either the carbide remains stable for hours or graphene nucleates and then grows slowly with time. The time evolution of the AES signal for the second scenario is shown in Fig. 4.13. This AES signal is a superpositioning of carbide and graphene signals. To identify the percentage of the carbide converted into graphene, a pure graphene AES spectrum is mixed with a pure carbide AES spectrum. The weights of the two spectra are varied to closely match the experimental data. This deconvolution of the carbon peak into graphene and carbide signals indicates that the graphene content increases at the expense of carbide. This means that the graphene phase grows by consuming the surface carbide. The fact that certain carbide samples remain stable for a long time (exceeding the time of the experiment, i.e. longer than 2h) may indicate that either there is not enough carbon in the sample to form graphene or the carbide layer suppresses graphene formation. The latter would also explain why samples exposed to hydrocarbons at 400°C for longer periods do not transform into graphene.

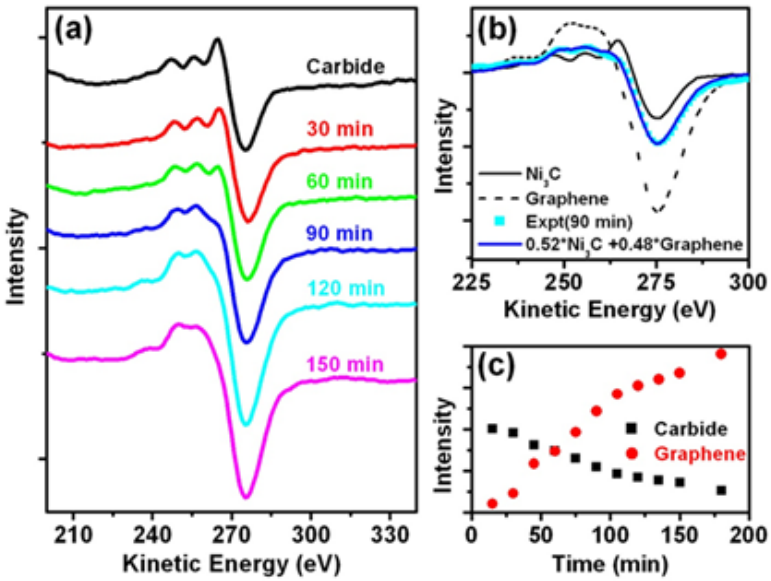

Figure 4.11: Transformation of a carbide into graphene at 400 °C. (a) Change of the C-KVV Auger signal as for different annealing times. An example of peak deconvolution into a carbide and graphene components is shown in (b) for the C-KVV peak after 90 min annealing. The black-solid curve is from a pure carbide, the dashed line is pure graphene, the square symbols show the experimental data and the dark blue line is a mixture of 52% carbide and 48% graphene signal. This mixture gives a good fit to the experimental data. The variation of the carbide and graphene contribution to the total signal is shown in (c) as a function of annealing time.

To test whether the presence of carbide results in a barrier for graphene's nucleation, an experiment has been designed to deliberately destabilize the surface carbide. The carbon-nickel bond is fairly strong which facilitates the carbide formation. Adding another element that does not form strong bonds with carbon, but interacts strongly with Ni atoms of the carbide should destabilize the surface carbide. A good candidate is copper, because it interacts weakly with carbon. In addition, it is known that Cu interacts strongly with Ni in the bulk, forming an isomorphous Cu-Ni alloy with a complete liquid and solid solubility of its constituents [91]. However, due to the lower

surface energy of copper compared to nickel, Cu stays at the surface at moderate temperatures [92]. Therefore, in order to explore the potential of Cu to destabilize the

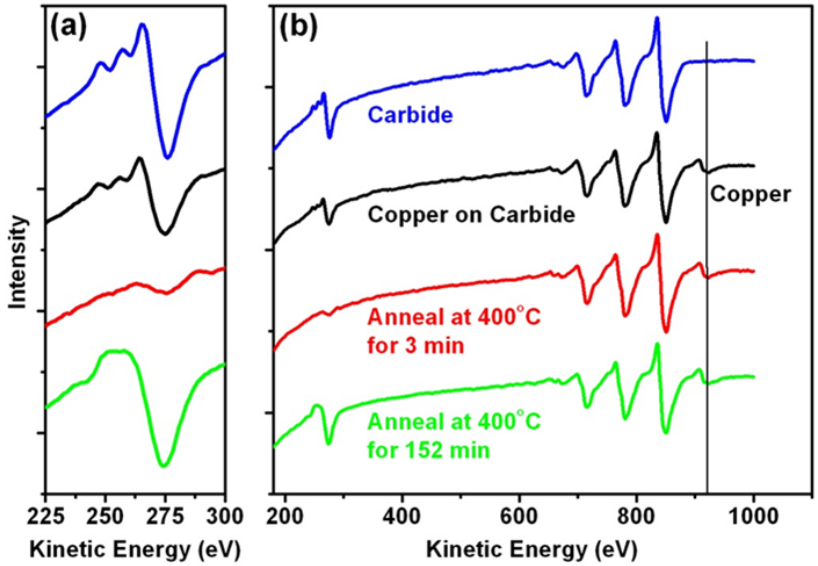

Figure 4.12: Destabilization of surface carbide by alloying with Cu. C-KVV Auger peak (a) and full Auger spectrum (b) for (i) surface carbide (blue), (ii) after deposition of ~0.3 ML Cu at room temperature (black), (iii) annealing at 400 °C for 3min (red), and after 152 min (green). It is apparent that after annealing to 400 °C the carbide peak disappears and graphene is slowly formed.

carbide phase, sub-monolayer amounts (0.25 ML) of copper were deposited onto a surface Ni_2C. The stability of the nickel carbide was tested prior to copper deposition and it was found to be stable at least for 90 min at 400 °C. After copper deposition at room temperature, the surface carbide phase was still present. However, annealing to 400 °C immediately caused a disappearance of the carbon signal, indicating the destabilization of the carbide by Cu and diffusion of the carbon into the bulk. After some time delay carbon re-emerged at the surface in the form of graphene and the C-AES signal grew with time. The time sequences of the carbon AES-signal is shown in Fig. 4.14. The graphene growth in the presence of copper is very similar to the growth on pure Ni at temperatures

above 480 °C in the sense that in both cases pure graphene phase is grown without any co-existent carbide phase. Furthermore, the experiment with copper deposition demonstrates that the system had sufficient carbon content dissolved in the bulk to support graphene growth. The fact that the sample containing surface carbide was not converted into graphene, but such conversion took place as soon as the carbide was destabilized by copper, reveals the role of the carbide layer as an inhibitor for graphene's nucleation.

The existence of two carbon containing thermodynamic equilibrium phases on Ni, carbide and graphene, makes Ni unique compared to other transition metals. These two phases differ in their carbon content and phase stability temperature. The surface Ni_2C phase has carbon concentration of 0.5 ML compared to 2ML for graphene. Furthermore, the surface carbide has a lower phase stability temperature and dissolves into the bulk at ~460 °C, while monolayer graphene is stable up to ~650 °C on Ni(111), before carbon dissolves into the bulk. The higher thermal stability of graphene suggests that it has a lower formation energy compared to the carbide surface phase. Also once graphene is formed it is stable never converts into a carbide below 650 °C.

If graphene is favored why does the surface carbide form at all? For a low carbon concentration the surface carbide is the thermodynamic equilibrium phase. To form the lower-energy graphene phase more carbon needs to be added to the surface layer. Furthermore, it appears that the carbide forms very rapidly while the graphene growth is rather slow, indicating a large kinetic barrier for graphene growth. Therefore, exposing the surface to carbon at the temperature, at which the carbide is stable, the carbide phase forms first. This carbide phase is a line-phase, i.e. it has a fixed carbon concentration,

within the carbon-Ni surface phase diagram. As a consequence, it is difficult to add carbon to this phase, because for an ordered line-phase small changes from its ideal composition increase its free-energy, which makes any compositional variations highly unfavorable. For the atomic-thick carbide-phase avoiding a change in its composition is easy because the Ni-bulk can ‘soak-up’ any excess carbon. Consequently, since an increased carbon density is the prerequisite for nucleating the carbon-denser graphene, the presence of the carbide phase at the surface suppresses graphene formation. The evidence for the suppression of graphene nucleation in the presence of a surface carbide comes from several experimental observations: (i) Graphene is not formed if the sample is exposed at 400 °C to ethylene and only a surface carbide is formed, (ii) some of the surface carbides once formed are stable in vacuum at 400 °C for hours, (iii) if the surface carbide is destabilized by sub-monolayer copper deposition, graphene can nucleate and grow, indicating that there has been enough carbon in the sample to form graphene, but the carbide had prevented its formation.

The fact that we sometimes observe a conversion of carbide into graphene at 400 °C, is not inconsistent with the scenario of carbide suppressing graphene nucleation. This is because local inhomogeneities exist within a macroscopic sample, which may act as nucleation sites for graphene. Therefore it appears that the carbide only suppresses nucleation of graphene but does not prevent its growth once nucleated. The growth of nucleated graphene in the presence of carbide is supported by the observation of carbide conversion into graphene as shown for example in Figure 4.17 and this is also further studied in the next subsection.

At above 480 °C, i.e. at a temperature where the carbide is dissolved, graphene can nucleate on the bare Ni-surface, similar to graphene growth on many of the other transition metal surfaces. If the carbide is destabilized, either by heating the sample above the carbide phase stability temperature or chemically by copper addition, the carbon atoms from the carbide phase first dissolve into the bulk and then later reappear to form graphene. The fast disappearance of carbidic carbon and the slow graphene growth indicates that the carbon diffusion is much faster than the graphene growth process. Information about the graphene growth rate can also be obtained from the AES peak intensity which is a direct measure of the portion of the surface covered with graphene. The variation of the peak intensity as a function of time, shown in Figure 4.10, indicates that the growth rate is strongly non-linear. This is in agreement with the assertion that the graphene growth rate is not limited by the carbon diffusion to the surface, because for a diffusion limited growth one would expect the growth rate to be linear with time. Instead, the carbon attachment to the growing graphene appears to be the rate limiting process. Large barriers for carbon attachment have also been reported for graphene growing on other transition metal surfaces [89, 90]. In these reports the attachment barrier for carbon atoms to the edges of the graphene sheet was associated with the strong bonding of carbon ad-atoms to the transition metal substrate compared to the relative weak interaction of the graphene sheet with the substrate. This may also contribute to the growth barrier for graphene on Ni(111). In addition, DFT calculations done by our collaborators indicate that the edge carbon atoms of the graphene form strong bonds with Ni substrate. Therefore, in order to add the carbon atoms to the edge, the strong carbon-nickel bonds have to be broken which also contributes to the kinetic growth barrier. Such

a barrier for carbon attachment suggests that the growth rate increases as the total number of edge atoms in the graphene island increase. This means that as the graphene islands grow and their circumference increases, the carbon attachment rate increases resulting in an accelerated growth. This is observed in the AES peak intensity plots shown in Fig. 4.10(b) for less than 150 min, i.e. during the initial growth stages. For longer growth times, i.e. at higher graphene coverage, when the graphene grains coalesce, the growth rate decreases again and eventually growth stops as the monolayer is completed. It appears that the growth rate for graphene as measured in AES differs for different sample preparation conditions. Therefore, it seems tempting to use this data to extract information on growth barriers. Unfortunately, this is not possible because the key information on the nucleation density is not available in these AES data.

4.4.2 Graphene formation on Ni(111) by transformation of a surface carbide

In the previous subsection we have seen by AES that the ordered surface carbide on Ni(111) can be transformed into graphene. This process is different for graphene formation on other transition metal substrates that do not exhibit surface carbide phase, or graphene growth on Ni above 480C where the carbide is unstable. Since the transformation of carbide into graphene is unique to nickel we investigate this process further with the goal of gaining fundamental insight of how this growth process of graphene differs from the growth on other transition metal surfaces.

Here, we describe scanning tunneling microscopy (STM) investigations on a Ni(111) single crystal that give atomic-level insight in phase-coexistence of the Ni-carbide surface phase (see section 4.3.1) and graphene under certain experimental

conditions. We show that the surface confined carbide phase lies in the same surface layer as the forming graphene sheet. Furthermore, these two phases match perfectly at their boundary forming a coincidence structure that facilitates the transformation process.

(a) (b)

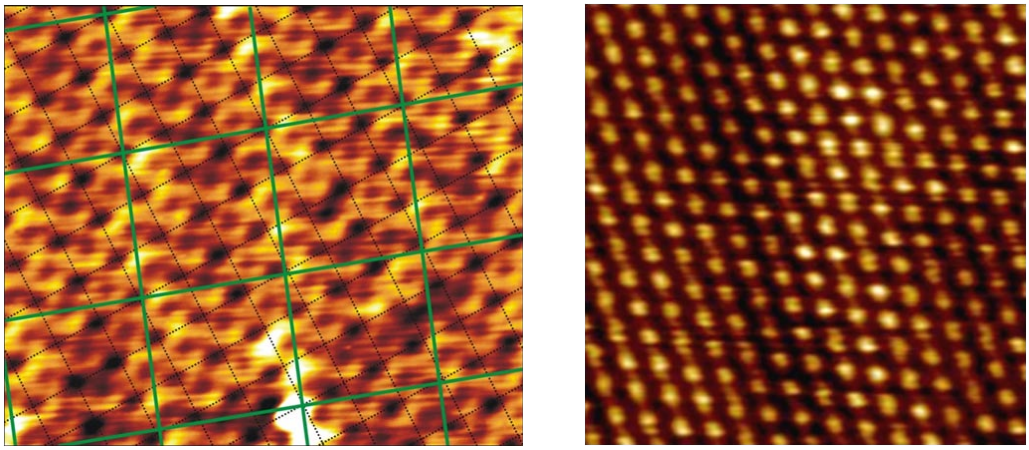

Figure 4.13: (a) STM image of Ni_2C.In STM the carbon atoms are imaged dark allowing for an identification of the quasi-square Ni_2C sub-lattice (black dashed lines). The large co-incidence unit cell between the Ni_2C and the Ni(111) substrate is indicated by the green lines.(b) STM image of graphene on Ni(111).

In order to obtain atomic-scale information on the carbide transformation into graphene, STM is used to characterize samples that exhibit a partially converted carbide layer, i.e. a carbide-graphene phase co-existence. STM images of the Ni_2C phase show the quasi-square clock-reconstruction introduced in section 4.3.1, can be seen in Figure 4.11. In these images the location of carbon atoms are imaged as dark as previously reported [60]. Figure 4.12(a) shows the structural complexity of surfaces that have been prepared to exhibit both graphene and carbide phases. All domains present at these surfaces can be identified as either carbide or graphene. In contrast to graphene grown above 480 °C, i.e. in the absence of carbide, areas are observed with the graphene lattice

rotated relative to the Ni(111) substrate. This rotation is apparent in STM images by the formation of a Moiré pattern. The rotation of two hexagonal lattices with close lattice match gives rise to a hexagonal superstructure. From the known lattice constants and the periodicity of the Moiré superstructure of 2.7-3 nm, measured in STM, the rotational angle between the two lattices is obtained as ~3°. Moiré patterns of graphene-layers on metal surfaces have been observed for many materials (see section 4.2) [29, 93-95]. Usually this is a consequence of the lattice mismatch between graphene and the substrate lattice. For Ni(111) the lattice mismatch is very small and no Moiré pattern is expected, nor has it been observed for high temperature growth conditions. Therefore, this Moiré pattern is not a feature of an equilibrium structure but rather an indication of the specific growth mechanism by the conversion of a surface carbide as discussed below.

In high resolution STM images as shown in Figure 4.12(c) the boundary between the graphene and the carbide phases is clearly seen. The excellent match at the 1D boundary indicates the close geometrical lattice relationship between graphene and the surface carbide phase. Importantly, the STM imaging clearly demonstrates that the graphene and carbide co-exist in the same atomic plane. This is in stark contrast to the growth of graphene above 460 °C or on other transition metal surfaces where the graphene sheet grows *on top* of the metal exposing 'free' graphene edges[89, 94].

Figure 4.12(d) shows a detailed view of the domain boundary between a carbide phase and a graphene layer. The phase boundary shows an excellent lattice-match between the two phases, with the hexagonal graphene lattice and the square carbide lattice clearly discernable in the two phases. The fact that the two lattices join 'seamlessly' at the boundary indicates the formation of a coincidence lattice. A close

match of the lattices in heterostructures reduces the interface energy and this is widely exploited in epitaxial thin film growth. In contrast to thin films, where the interface is two-dimensional, the interface between two 2D materials, like graphene and surface nickel carbide, is a one dimensional line. Therefore this study shows that similar principles that dominate growth of three dimensional materials may also apply for atomic-layer thin 2D materials.

Further evidence that the coincidence structure between graphene and the carbide phase defines the growth of graphene comes from the observed Moiré pattern. The ~ 3° rotation angle between the graphene and the Ni(111) substrate that causes the Moiré pattern is identical to the rotation of the surface nickel carbide layer as indicated in Figure 4.6(b). Therefore, the Moiré pattern is a consequence of the graphene layer adopting the same rotation angle as the nickel carbide phase. This is explained if graphene nucleates within the carbide phase and minimizes its (in-plane) phase-boundary energy by adopting a coincidence structure with the carbide.

The discovery of two distinct growth regimes of graphene on Ni(111) surfaces indicates the complexity of this process. The formation of a surface confined carbide and the possible coincidence lattice between the carbide and the graphene are special properties of Ni indicating that there may not be a ‘universal’ growth mechanism for graphitic nanomaterials. Understanding this diversity will enable a better control of growth of materials with desired properties. In addition to understanding the growth of graphene the formation of a one dimensional interface between carbide and graphene has implications for making contacts to graphene and for tuning graphene properties. Especially doping and introduction of ferromagnetism in graphene-nanoribbons by

decoration of the edges of graphene with metals is being discussed theoretically. The graphene/ carbide interface described here offers an approach to experimentally placing Ni-atoms at the boundary of a graphene sheet.

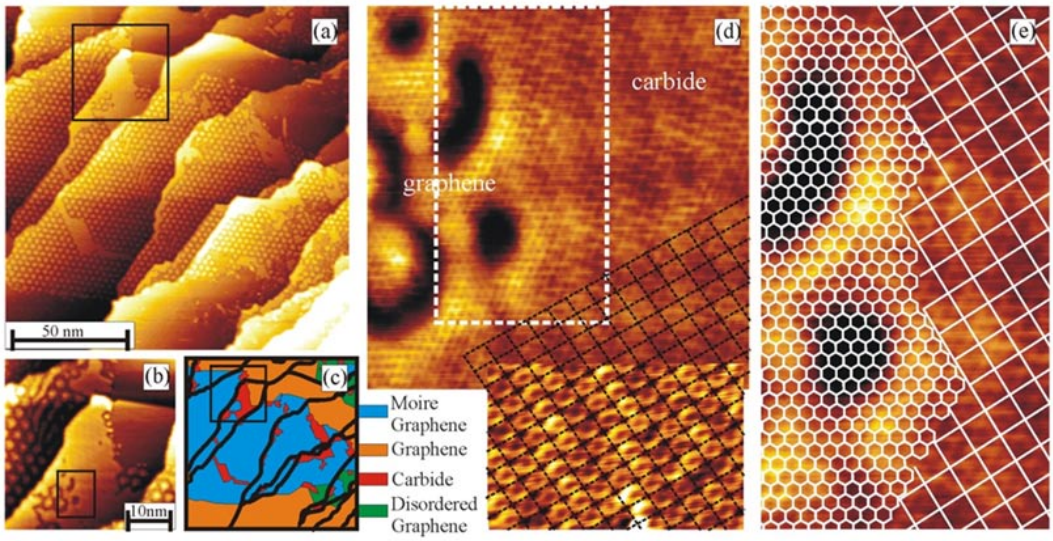

Figure 4.14: STM of a coexistence of carbide and graphene phases. (a) Large scale image showing regions of graphene and carbide as indicated in (c). Large areas of the sample are covered with a graphene Moiré pattern formed by rotation of the two hexagonal lattices of the graphene layer and the Ni(111) surface by 3°. The area highlighted by the square in (a) is shown in (b). A further zoom of the domain boundary region between graphene and carbide highlighted in (b) is shown in (d). On the left side of (d) the hexagonal structure of the graphene domain can be identified while the right side shows the quasi-square structure of the carbide. The domain boundary between the two phases is in the same atomic plane and smooth, i.e. without any defect pattern. This smooth interface indicates that the two phases form a one-dimensional co-incidence structure at the interface. A superpositioning of the carbide and graphene lattices is indicated in (e).

4.4.2 Growth and stability of Ni deposited on graphene/Ni(111)

To further investigate the Ni/graphene interactions we vapor-deposited Ni on top of a graphene sheet supported on a Ni(111) substrate. This results in Ni-cluster formation on top of the graphene and formation of local Ni/graphene/Ni sandwich structures. The Ni

cluster growth was monitored by AES and STM. Upon annealing local carbide grains are produced. The temperature range and kinetics of this carbide formation process temperature dependent AES and CO-TPD studies have been performed.

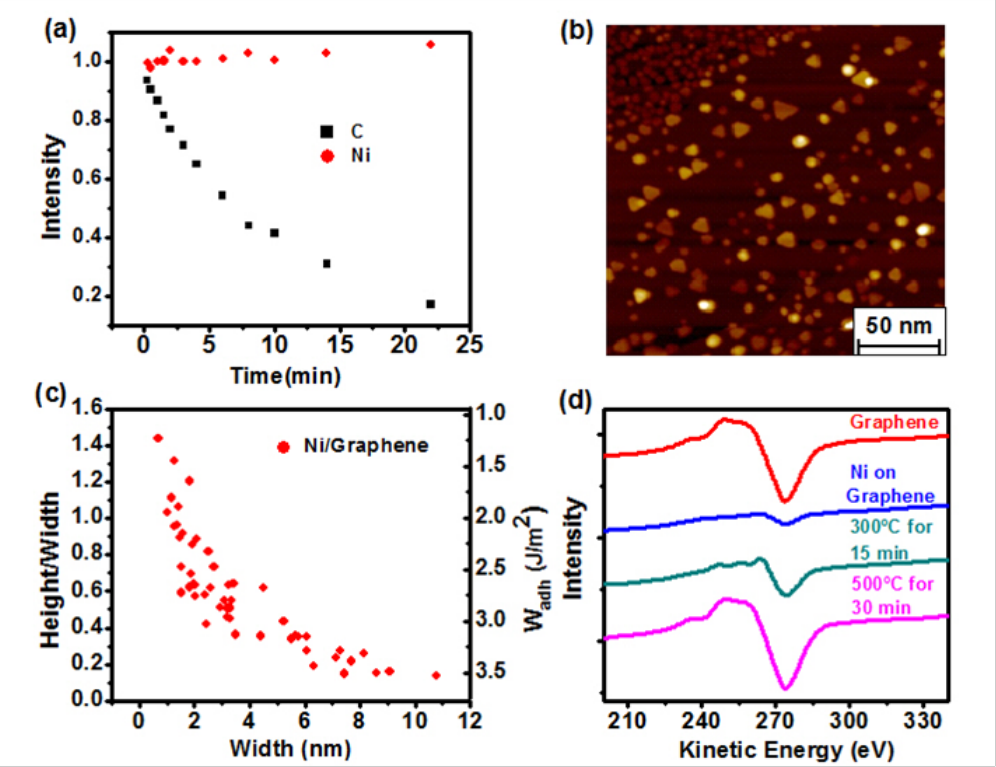

Figure 4.15: Ni deposition on Ni(111) supported graphene. (a) Auger peak intensity of C-KVV and Ni-LMM as a function of deposition time. The slow gradual change in the slope of the C-KVV intensity indicates cluster growth. (b) STM images of Ni-deposits on graphene at room temperature. 3D Ni-clusters with well defined (111) facets are formed. The height/width ratio of these clusters is plotted against the cluster width in (c). This ratio corresponds to the work of adhesion. An increase in the work adhesion with cluster width is observed that seems to saturate ~3.5 J/m^2. C-KVV Auger peaks are shown in (d). The pristine graphene peak is shown in red, after deposition of Ni at room temperature the graphene peak is attenuated (blue). Annealing to 300 °C for 15 min results in a (partial) transformation of the graphene into carbide (green). Prolonged annealing at 300 °C (30 min) reforms the graphene peak (magenta).

Auger electron intensities for the Ni-LMM and C-KVV peaks as a function of Ni-deposition are shown in Fig. 4.15 (a). The carbon signal displays a continuous attenuation with increasing Ni deposition. However, the attenuation is non-linear indicating that the deposited Ni does not grow in a layer-by-layer fashion but instead forms clusters at the surface. The cluster growth can be directly observed in STM measurements shown in Fig. 4.15 (b). Ni deposits form 3D clusters with well-defined (111) facets at room temperature. Figure 4.16(a) shows a high resolution image of ~ 0.5 monolayer (ML) equivalent of Ni deposit, where 1 ML is taken as the number of Ni atoms in a Ni(111) plane. The Ni clusters have well defined crystallographic shapes with a clearly defined crystallographic orientation relative to the graphene substrate, similar to observations on other metal supported graphene samples [96]. We do not observe any preferential nucleation of the Ni at step edges but observe alignment of Ni clusters into chains suggesting preferential nucleation at defect sites in the graphene.

Using an approach developed by Hansen et al.[97], the work of adhesion (WoA) of the clusters to graphene can be determined from the measurements of the width of the top facet and the height of the clusters via the following relationship:

$$W_{adh} = 2\gamma_{111} - \frac{H}{W}\left(-\frac{3}{\sqrt{2}} + \sqrt{3}\gamma_{110} + \sqrt{\frac{3}{2}}\gamma_{100}\right) \quad (7)$$

Here " and " are the height and width of the clusters and γ_{111}, γ_{110} and γ_{100} are the surface free energies of the (111), (110), and (100) facets of the nickel crystal. The values for the surface energies are taken from Ref [98]. The height and width of the top facet are two quantities easily determined from the STM images. The work of adhesion is plotted as a function of cluster width in Fig. 4.17(c). It is apparent that small clusters

exhibit a smaller work of adhesion compared to large clusters. A similar behavior has been reported for metal clusters supported on metal oxides [99, 100]. In the limit for large clusters we find a significant work of adhesion of 3.5 J/m^2.

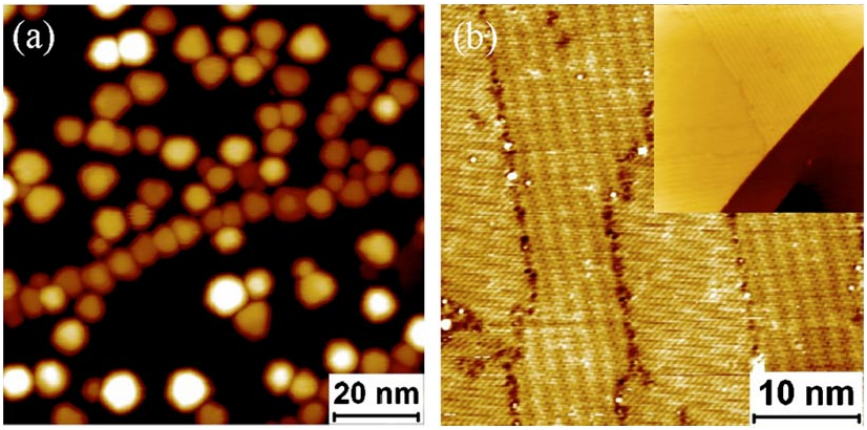

Figure 4.16: Scanning tunneling microscopy images of (a) Ni deposition at room temperature, showing 3D Ni cluster formation, and (b) several domains of an ordered surface carbide formed after annealing the Ni clusters in (a) to 380 °C for 30 min. The inset in (b) shows a 30x30 nm^2 STM image of a region that exhibits a coexistence of a carbide and graphene phase on the top-terrace. The monoatomic step edge visible in the image serves as a scale bar to indicate that the graphene and carbide are in the same atomic layer.

Annealing of the deposited Ni clusters causes the transformation of the surface structure. Figure 4.15(d) shows the change of the Auger signal for ~2ML Ni deposited on graphene/Ni(111) after annealing at different temperatures. Inspection of C-KVV peak shape indicates the formation of carbide upon annealing. It shows carbide formation after annealing the sample at 300 °C for 15 min which converts into graphene after annealing to higher temperatures. In STM we observe that annealing of the Ni deposit on graphene causes some coalescence of the Ni clusters but mainly a reduction in the total Ni coverage. This indicates a loss of surface Ni by diffusion into the substrate. Inspection of the surface structure by high resolution STM indicates that the graphene sheet has been

partially destroyed and large areas of a surface-carbide have formed (see Figure 4.16(b)). Ni(111) is known to form a well defined, ordered surface carbide phase that is confined to the topmost atomic layer, that can be easily discriminated in STM images [60]. This carbide is planar, i.e., the graphene and carbide are in the same surface layer.

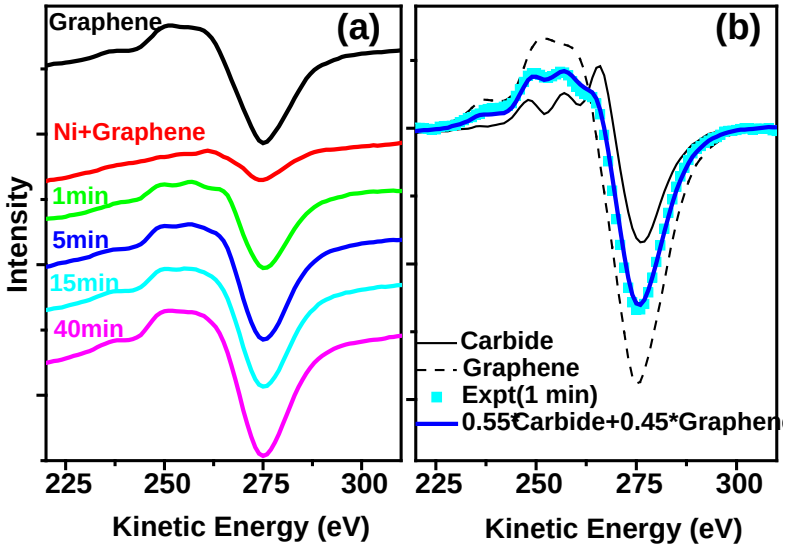

Figure 4.17: Carbon-KVV Auger line for graphene layer upon Ni deposition. (a) shows the clean graphene film and after room temperature deposition of Ni. The Carbon Auger line shape and intensity changes after annealing at 300 °C for different time intervals. In (b) the experimental line for 1 min annealing is fitted by matching the pure carbide and pure graphene line shape to the experimental data. The best fit is obtained for 55% carbide and 45% graphene character.

To investigate the destabilization of graphene upon Ni deposition further we investigate the evolution of the C-KVV AES at constant temperature with time. Figure 4.17 shows a series of carbon-KVV AES spectra taken at different time intervals after deposition of ~5 ML Ni and annealing of the sample to 300 °C. Analysis of the peak shape allows identification of carbide formation. Mixing of reference spectra for pure surface nickel carbide and pure graphene allows an estimate of the percentage of surface carbide formation. Figure 4.17(b) shows that the C-KVV peak after 1 min annealing

contains 55% carbide and 45% graphene character. For longer annealing times the surface converts back into graphene and after 15 min there is only graphene present at the surface.

Experimentally, we observe that annealing of the Ni-deposits to above 200 °C results in partial conversion of the graphene into carbide followed by reforming of graphene after annealing either to higher temperatures or at the same temperature but during long annealing periods. From a thermodynamics standpoint, Ni-clusters on top of graphene are not energetically favorable, because the pure Ni-surface has a high surface energy compared to Ni covered by graphene. Therefore, the lowering of the free energy of the system by transferring of Ni atoms from the clusters on top of graphene to the Ni substrate provides a driving force for this process. Similar thermodynamic arguments hold for other metals deposited on Ni supported graphene and the intercalation of different elements, such as Cu, Au, and Ag deposited on Ni-supported graphene have been observed in several experiments [79, 81]. Our measurements show carbide formation as an intermediate state for the Ni-intercalation process. This implies that Ni-deposits can merge with the substrate via diffusion through a carbide layer. For Ni deposits, our DFT calculations support the destabilization of the graphene. For other elements, namely Cu, the DFT results, do not indicate the same destabilization of the graphene and therefore the intercalation process for Cu may be different from that of Ni. Consequently there may not exist a universal mechanism of metal intercalation on Ni-supported graphene. Therefore, the intercalation of metals other than Ni might proceed through a different mechanism which requires further experimental and theoretical investigations.

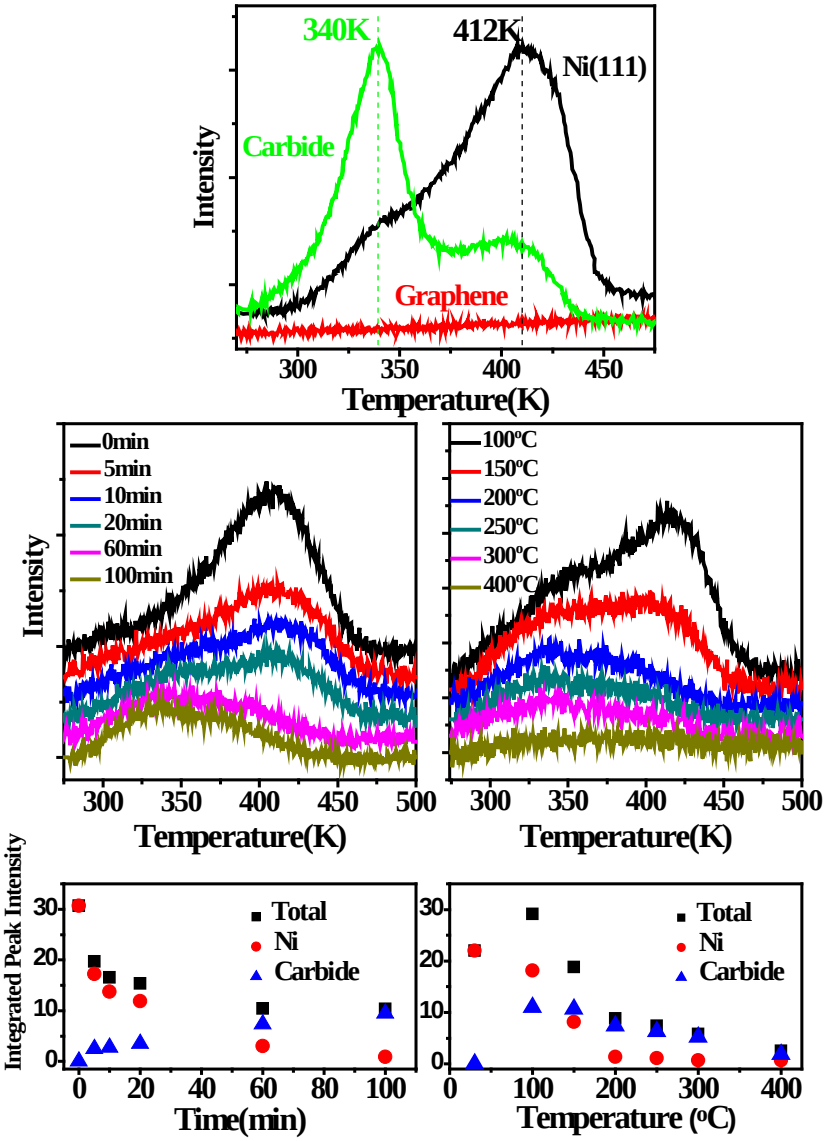

Figure 4.18: CO-thermal desorption studies for determination of carbide formation. (a) shows thermal desorption traces of CO from pure Ni(111), surface carbide, and graphene surface phases. (b) shows CO desorption from a Ni deposit on graphene annealed at 200 °C for different time periods. The change in the desorption traces with annealing period indicate a transition from pure Ni clusters to carbide. The deconvolution of the desorption traces in components due to CO desorbing from Ni and carbide is shown in (c). (d) shows CO desorption from samples annealed for 1 h at different temperatures. The contributions for CO desorbing from a carbide and pure Ni to the total CO desorption trace are shown in (e).

The separation of the graphene and carbide contribution in the carbon KVV AES line is difficult for low carbide concentrations. To detect small amounts of carbide, we developed the CO titration method. In addition to enable detecting smaller amounts of carbide, this method is also only sensitive to the topmost surface layer and thus is even more surface sensitive than AES. Furthermore, it enables to determine if Ni is present in the surface layer as pure Ni or as Ni carbide. The characteristic desorption traces from reference samples for the different surface phases are shown in Figure 4.18(a). Figure 4.18(b) shows a set of TPD spectra taken for 1 ML Ni deposits after annealing at 200 °C for different time periods from 5 to 100 min. Figure 4.18(c) shows TPD spectra for samples annealed for 1 hr at different temperatures. The spectra contain contributions from both CO desorption from pure Ni clusters at the surface as well as from Ni carbide. The contribution from the pure Ni can be subtracted since the desorption-peak maxima for pure Ni and Ni carbide are well separated. The remaining intensity can be assigned to CO desorbing from the surface carbide. This shows that at 200 °C the Ni deposit converts completely into carbide. With increasing annealing time the amount of pure Ni decreases as the amount of carbide increases until after 100 min Ni is only present as carbide at the surface (see Figure 4.18(b)). Measurements at different temperatures (Figure 4.18(c)) show that already at 100 °C some carbide is formed however even after 100 min annealing there is still a significant amount of pure Ni clusters at the surface. Annealing to 200 °C is needed for the surface Ni clusters to disappear; however, carbide is still present at the surface. Annealing to above 400 °C is required to reform a graphene sheet. It is interesting to compare the sensitivity of the CO-TPD method with AES. It is difficult to extract information on the presence of carbide from the AES spectra after annealing a

300 °C for longer than 6 min (see Figure 4.17) while the CO titration experiments still detects the presence of carbide even after 100 min.

Thus we find that a single layer of graphene supported on Ni(111) is stable up to ~ 950 K, but if it is sandwiched between two Ni-layers it becomes unstable and decomposes into a Ni-carbide at low temperatures (500K) already. This allows Ni deposited on top of graphene to diffuse through the carbide layer which subsequently reforms the graphene sheet. Therefore, the formation of the carbide explains the phenomena of metal intercalation on Ni-supported graphene. The (in)stability of graphene also has implications for making electrical contacts to graphene and for potential applications of graphene as spin-filters. We may also use this approach of local modification of metal-supported graphene that converts graphene into carbide as a patterning method. This carbide formed can then be chemically etched together with the metal substrate to obtain a freestanding, patterned graphene sheet.

4.4.4 An extended defect in graphene as a metallic wire

The honeycomb arrangement of atoms in graphene is the favored structure of sp^2 carbon. Point defects can be introduced through the formation of vacancies or di-vacancies, followed by atomic rearrangements to produce Stone–Wales defects consisting of pentagons and heptagons [101-103]. Hypothetical one-dimensional defect structures embedded in graphene and carbon nanotubes have been suggested from computer modeling [104, 105]. The observation of two-dimensional grain boundaries in highly ordered pyrolytic graphite (HOPG) support the formation of such reconstructed carbon

structures [106]. So far, however, no one-dimensional defect has been experimentally observed in graphene, and no approach has been reported for their controlled formation.

One-dimensional defects can be formed by a translation of two half-lattices relative to one another by a translation vector $1/3(\mathbf{a_1} + \mathbf{a_2})$, where $\mathbf{a_1}$ and $\mathbf{a_2}$ are the unit cell vectors of graphene, with the resulting dislocation line occurring along the $\mathbf{a_1}$–$\mathbf{a_2}$ direction, as shown in Figure 4.19(a). The two domains can be joined at their boundary so that every carbon has threefold coordination, forming a one-dimensional topological defect consisting of a pair of pentagons and one octagon periodically repeated along the dislocation line. In this new structure, all the carbon atoms show C–C bond lengths and angles that are reasonable for sp^2 hybridization. Density functional theory (DFT) calculations have been used to verify the stability of the defect structure and provide the fully relaxed geometry shown in Figure 4.19(b).

The energy cost for the formation of extended defects in covalently bonded materials is high. This makes the spontaneous formation of such a one-dimensional defect during the growth of graphene highly unlikely. A new approach for the synthesis of such extended defects is therefore required. The formation of this defect involves two graphene sheets that are precisely translated relative to each other and joined along a common defect line. The small magnitude of the necessary translation vector of less than the unit cell vector requires a scaffold that can hold two growing graphene sheets in registry to each other with atomic precision. Such a scaffold can only be a two-dimensional atomic lattice for which graphene has a close epitaxial relationship, such as Ni(111).Graphene grows on Ni(111) with half of the carbon atoms situated on top of nickel atoms and the other half at threefold hollow sites [72]. Two non-equivalent

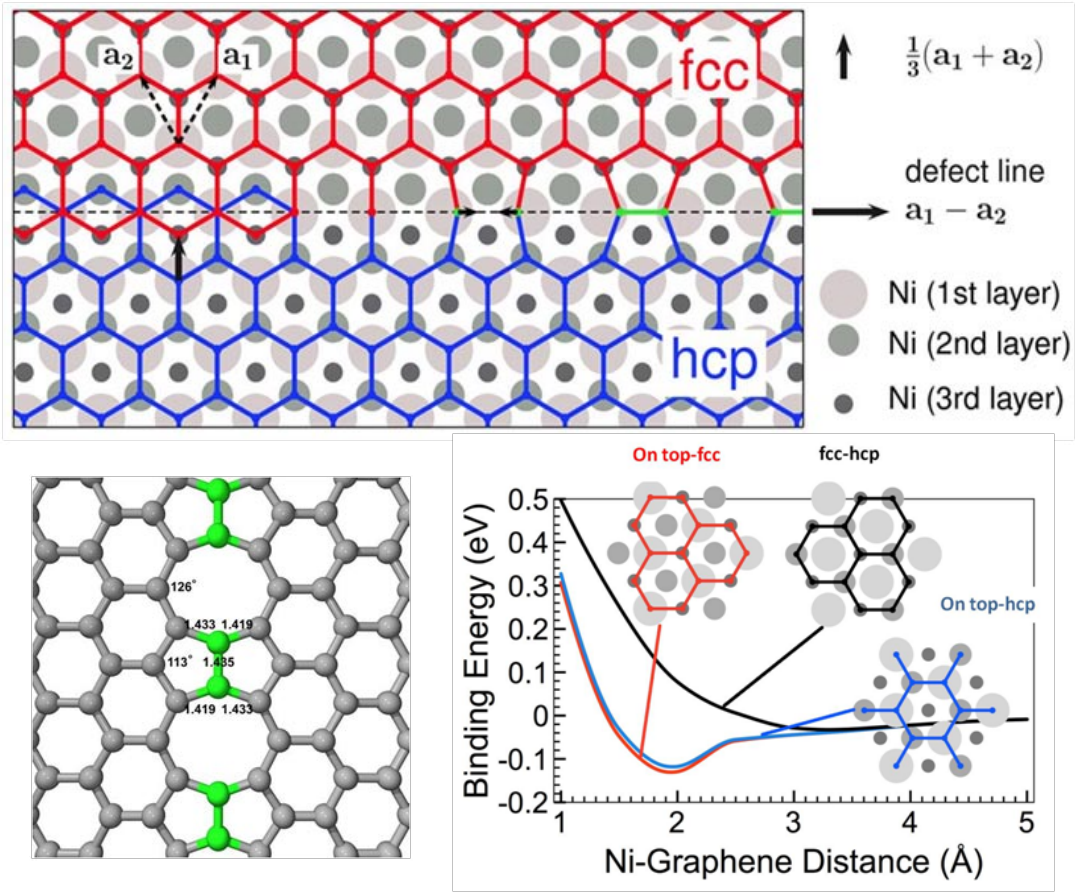

Figure 4.19: Structural model and schematic formation of an extended one-dimensional defect in graphene. a–c, Two graphene half-lattices, with unit cell vectors $\mathbf{a_1}$ and $\mathbf{a_2}$ (dashed arrows), are translated by a fractional unit cell vector $1/3(\mathbf{a_1}+\mathbf{a_2})$, indicated by the vertical vector (solid arrow) (a). The two half-lattices can be joined along the $\mathbf{a_2}-\mathbf{a_2}$ direction, indicated by the horizontal vector, without any unsaturated dangling bonds, by restructuring the graphene lattice. The domain boundary can be constructed as shown, by joining two carbon atoms, indicated by the two arrows, along the domain boundary line. This reconstructed domain boundary forms a periodic structure consisting of octagonal and pentagonal carbon rings. The underlying Ni(111) structure illustrates how the extended defect is formed by anchoring two graphene sheets to a Ni(111) substrate at slightly different adsorption sites. If one graphene domain has every second carbon atom located over a fcc-hollow site (red) and the other domain over a hcp-hollow site (blue), then the two domains are translated by $1/3(\mathbf{a_1}+\mathbf{a_2})$ relative to one another. The calculated adsorption energies for these two domains are very similar, but both are lower in energy than a third possible adsorption configuration with all carbon atoms on hollow sites, as shown in c. The DFT relaxed geometry of the defect structure, including bond lengths (in Å) and bond angles, is shown in b.

threefold hollow sites exist on Ni(111), termed fcc (face-centred cubic) and hcp (hexagonal close-packed) sites. The carbon atoms in a graphene sheet on Ni(111) can occupy one of these two sites. A translation of $1/3(\mathbf{a_1} + \mathbf{a_2})$ changes the adsorption geometry of the graphene lattice from fcc to hcp. The growth of two domains with slightly different adsorption geometries on Ni(111) therefore fulfils the necessary conditions for the formation of the extended one-dimensional defect, as shown in Figure 4.19. To assess the possibility of creating the fcc and hcp domains of graphene on Ni(111), the adsorption energy was calculated for the two adsorption geometries. DFT calculations show that the fcc-hollow site is favoured over the hcp-hollow site by only~ 12 meV $atom^{-1}$. This energy difference is small compared with the 100 meV $atom^{-1}$ lower binding energy for graphene with all carbon atoms adsorbed at threefold hollow sites (see Figure 4.19(c)). This suggests that the simultaneous presence of both fcc and hcp configurations is possible for graphene grown on Ni(111).

A systematic search of single-layer graphene samples grown on Ni(111) was carried out using scanning tunnelling microscopy (STM) to identify the formation of the anticipated domain boundaries between the fcc and hcp domains of the graphene. This revealed that, in addition to the fcc and hcp stacking of the graphene/Ni(111), a number of other different orientations of the graphene relative to the nickel substrate could be realized. For example, Figure 4.20(a) shows a Moire´ structure for a small domain, indicating a rotation of the graphene layer relative to the Ni(111) substrate. This observation confirms that the adsorption energy between nickel and graphene is relatively weak and, consequently, different adsorption geometries are possible. STM images also revealed areas with ridges that were~0.5 Å tall in the graphene layer (see Figure 20(b,c)).

Closer atomic scale examination showed that these ridges separate the sought fcc and hcp domains. Apparently, the local delamination of graphene from the Ni(111) substrate and its slight bulging away from the substrate allows matching of the fcc and hcp graphene/Ni(111) stackings by a continuous sheet of graphene without the formation of the topological defect (see Figure 20(d)).

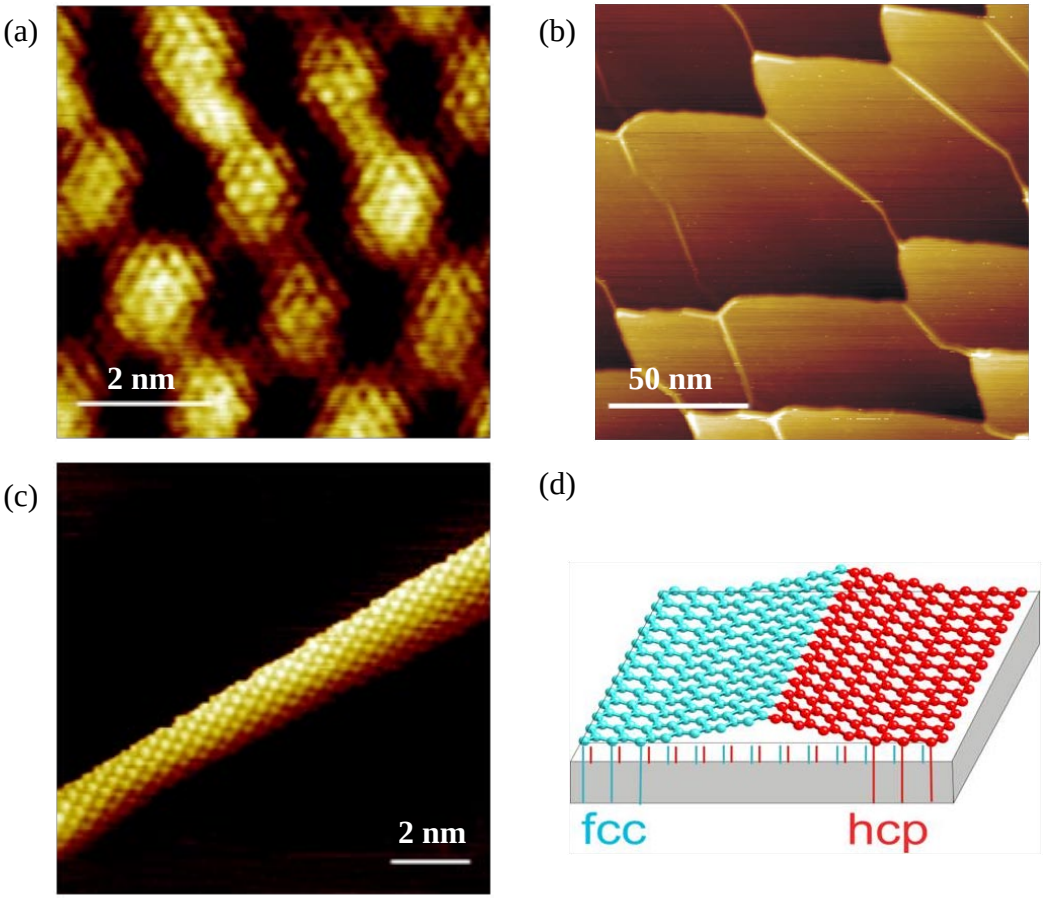

Figure 4.20: STM images of graphene on Ni(111). (a) Graphene lattice rotated relative to the Ni(111) substrate, showing a Moire´ structure and demonstrating the weak adsorption of graphene on Ni(111).(b) (c) Ridge structure separating the fcc and hcp domains of the graphene/Ni(111) interface. (d) Schematic of how the ridge structure in the graphene sheet accommodates the mismatch between the two domains. The red and blue lines indicate the registry of the graphene lattice with the hcp and fcc lattice sites, respectively.

To form extended topological defect lines, as shown in Figure 4.19, both the fractional translation vector and the direction of the dislocation line must be fulfilled simultaneously. In most crystallographic directions there is no low-energy topological defect joining the translated graphene lattices. Therefore, the delamination process is the common means of joining the carbon–carbon bonds and lowering the energy. However, in the special case of the boundary aligned along the ($\mathbf{a_1}$–$\mathbf{a_2}$) direction of the graphene lattice, a planar periodic defect structure was formed in our experiments, in agreement with the prediction shown in Figure 4.19. The STM image in Figure 4.21(a) shows a transition from the 'ripple' domain boundary to an extended topological line defect, thus confirming that both structures are boundaries of the same fcc and hcp domains. A period of twice the unit cell vector of graphene along the defect line has been measured by STM. The atomic locations identified from the STM image (Figure 4.21(b)) indicate that the defect is composed of one octagon and a pair of pentagons. In atomically resolved STM images of graphene on Ni(111), only three atoms, rather than all six atoms, in the honeycomb structure are visible. Such second-atom imaging is expected because of the two different adsorption sites of the carbon atoms on the nickel substrate. If the carbon atoms situated on top of the nickel atoms were imaged in STM, there would be no differences between the STM images of the hcp and fcc domains on either side of the line defect. Instead, we clearly observe the sublattices on the two sides of the defect line translated by 1/3($\mathbf{a_1}$ + $\mathbf{a_2}$) relative to one another. Therefore, we only image the carbon atoms located over three-fold hollow sites.

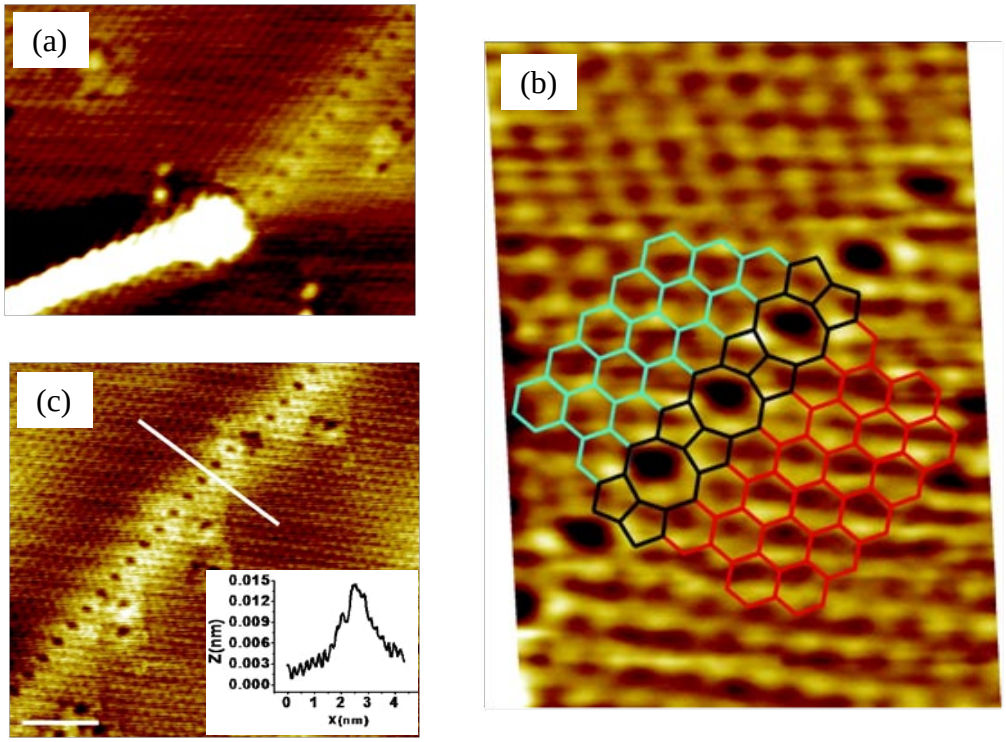

Figure 4.21: STM images of extended one-dimensional defects in graphene. (a) Transition from a ridge domain boundary to an extended one-dimensional defect line. (b) Defect structure and superimposed defect model. (c) Line defect with image profile in the direction perpendicular to the wire (inset). The brighter area surrounding the defect originates from the states with wavefunctions localized at the defect, and decays exponentially away from the defect core.

Localized electronic states in extended one-dimensional defects have been previously investigated as a potential way of self-doping graphene [8]. In addition, the metallic character of the electronic structure of sp^2-hybridized carbon systems due to the presense of 5- and 7-member rings has been shown in ref. 21. The calculated band structure and density of states (DOS) of the newly discovered extended topological defect are shown in Figure 4.22. The DOS shows the characteristic $1/\sqrt{E}$ singularities at the band extrema, which is considered to be the true signature of a one-dimensional character of the electronic structure, as has been observed for carbon nanotubes and graphene

nanoribbons (GNR) [8, 107, 108]. It shows an almost flat band, similar to that of zig-zag-edged GNR. This results in a spike in the DOS at the Fermi level. However, in contrast to zigzag-edged GNR, for which the flat band extends within $2\pi/3<|k|<\pi$ of the Brillouin zone, the flat band of the one-dimensional topological defect is located in the centre of the Briliouin zone. The electronic states from the band close to the Fermi level produce a local doping in a narrow stripe along the line defect, thus creating a perfect one-dimensional metallic wire embedded in the perfect graphene sheet. The STM images, taken with a bias voltage of 100 mV, probed the local DOS close to the Fermi level. This allowed us to explore the spatial distribution of the wavefunctions associated with the line defect. The STM image shown in Figure 4.21(c) shows the brightest contrast along the defect line. The profile across the defect line (inset of Figure 4.21(c)) shows the decaying contrast away from the defect. The decay length of the contrast variation observed in STM is~0.8 nm, which is similar in magnitude to that reported for metallic edge states of graphene flakes, thus producing an estimate for the width of the metallic wire [109]. The controlled formation of extended one-dimensional defects in graphene is of great significance for developing graphene-based electronics. Single-layer graphene sheets containing line defects can be detached from the nickel substrate by chemically dissolving the nickel support, and can then be transferred to insulating substrates to perform transport measurements [110]. This opens up the exciting possibility of the fabrication of all-carbon electronic devices with one-dimensional extended defects that can be used as metallic wire interconnects or elements of device structures. Furthermore, the well-defined atomic structure of the nanowire embedded in an atomically perfect graphene sheet can help to address practically one of the challenges of nanoelectronics—

the formation of well controlled contacts at the atomic level. This is urgently needed for the development of molecular electronics and single-molecule sensors [111]. Finally, the octagonal holes within the extended defect structures may also extend the applications of graphene as a membrane material for selective diffusion of atoms or small molecules through otherwise impermeable graphene membranes [112].

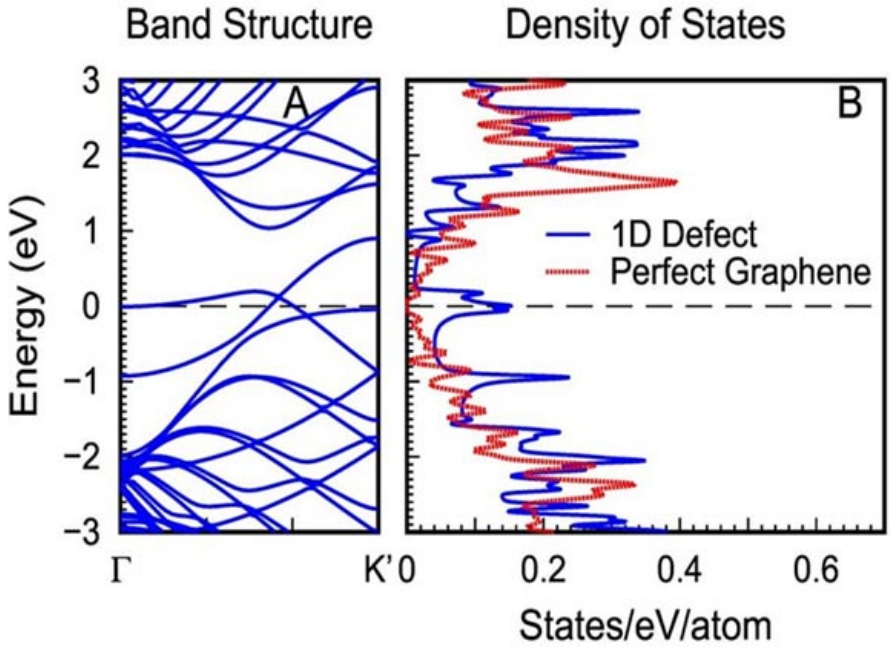

Figure 4.22: Electronic structure of the extended one-dimensional defect.(a) Band structure, showing a flat band close to the Fermi level in the first half of the Brillouin zone. (b) Density of states of perfect graphene (red) and the one-dimensional extended defect (blue), illustrating the metallic character of the wire.The latter shows $1/\sqrt{E}$ singularities at the band structure extrema, characteristic of truly one-dimensional systems.

4.5 Conclusion

We have studied graphene growth on Ni(111) using STM and AES. We found that graphene grows on pure Ni(111) surface in the absence of a carbide at temperatures between 480 °C and 650 °C. Below 480 °C graphene growth competes with formation of

Ni_2C surface carbide. This Ni_2C phase suppresses nucleation of graphene. Destabilization of the surface carbide by adding Cu to the surface layer facilitates the nucleation and growth of graphene at temperatures below 480 °C. Our atomic level STM studies also show that a Ni-carbide *surface* phase and graphene can coexist. We show that the carbide phase lies in the same surface layer and the two phases match perfectly at their boundary forming a 2D-coincidence lattice that facilitates the transformation of surface carbide into graphene upon annealing to ~ 900K. Furthermore, the carbide phase imposes the orientation of the graphene layer relative to the Ni(111)-substrate, confirming the importance of the carbide phase in the formation of the graphene layer. These atomic resolved STM studies are the first direct evidence that the graphene sheet is evolving from surface carbide. Similar mechanisms may also be relevant for the growth of carbon nanotubes.

The stability of Ni clusters on graphene/Ni(111) interface is studied by Auger electron spectroscopy (AES), temperature programmed desorption (TPD) of CO-probe molecules and STM. We find that a single layer of graphene supported on Ni(111) is stable up to ~ 950 K, but if it is sandwiched between two Ni-layers it becomes unstable and decomposes into a Ni-carbide at low temperatures (500K) already. This allows Ni deposited on top of graphene to diffuse through the carbide layer which subsequently reforms the graphene sheet. Therefore, the formation of the carbide explains the phenomena of metal intercalation on Ni-supported graphene. The (in)stability of graphene also has implications for making electrical contacts to graphene and for potential applications of graphene as spin-filters.

We have studied the atomic structures of defects produced in graphene using Scanning Tunneling Microscopy (STM). We have discovered for the first time extended line defects in graphene. These 1D structures are the consequence of domain boundaries between graphene-sheets occupying different registry relative to the nickel substrate. Atomic resolution STM showed that the line defect consists of fully sp^2 hybridized carbon arranged in pentagons and octagons. Density functional theory showed that these defects have a high density of electronic states at the Fermi-level. The wavefunctions of these electronic states at the defect decay exponentially into the graphene lattice causing a local doping in the vicinity of the defect. This self-doping effect gives rise to the brighter contrast of the surrounding of the defect in STM images

4.6 References

1. Allen, M.J., V.C. Tung, and R.B. Kaner, *Honeycomb Carbon: A Review of Graphene.* Chemical Reviews, 2010. **110**(1): p. 132-145.

2. Geim, A.K. and K.S. Novoselov, *The rise of graphene.* Nature Materials, 2007. **6**(3): p. 183-191.

3. Geim, A.K. and A.H. MacDonald, *Graphene: Exploring carbon flatland.* Physics Today, 2007. **60**(8): p. 35-41.

4. Geim, A.K., *Graphene: Status and Prospects.* Science, 2009. **324**(5934): p. 1530-1534.

5. Novoselov, K.S., et al., *Electric field effect in atomically thin carbon films.* Science, 2004. **306**(5296): p. 666-669.

6. Zhang, Y.B., et al., *Experimental observation of the quantum Hall effect and Berry's phase in graphene.* Nature, 2005. **438**(7065): p. 201-204.

7. Novoselov, K.S., et al., *Two-dimensional gas of massless Dirac fermions in graphene.* Nature, 2005. **438**(7065): p. 197-200.

8. Castro Neto, A.H., et al., *The electronic properties of graphene.* Reviews of Modern Physics, 2009. **81**(1): p. 109-162.

9. Novoselov, K.S., et al., *Electronic properties of graphene.* Physica Status Solidi B-Basic Solid State Physics, 2007. **244**(11): p. 4106-4111.

10. Stander, N., B. Huard, and D. Goldhaber-Gordon, *Evidence for Klein Tunneling in Graphene p-n Junctions.* Physical Review Letters, 2009. **102**(2): p. 026807.

11. Beenakker, C.W.J., *Colloquium: Andreev reflection and Klein tunneling in graphene.* Reviews of Modern Physics, 2008. **80**(4): p. 1337-1354.

12. Bae, S., et al., *Roll-to-roll production of 30-inch graphene films for transparent electrodes.* Nat Nano. **advance online publication**.

13. Berger, C., et al., *Ultrathin epitaxial graphite: 2D electron gas properties and a route toward graphene-based nanoelectronics.* Journal of Physical Chemistry B, 2004. **108**(52): p. 19912-19916.

14. Berger, C., et al., *Electronic confinement and coherence in patterned epitaxial graphene.* Science, 2006. **312**(5777): p. 1191-1196.

15. Hass, J., et al., *Highly ordered graphene for two dimensional electronics.* Applied Physics Letters, 2006. **89**(14): p. 3.

16. Emtsev, K.V., et al., *Towards wafer-size graphene layers by atmospheric pressure graphitization of silicon carbide.* Nature Materials, 2009. **8**(3): p. 203-207.

17. Li, X.S., et al., *Evolution of Graphene Growth on Ni and Cu by Carbon Isotope Labeling.* Nano Letters, 2009. **9**(12): p. 4268-4272.

18. Hass, J., W.A. de Heer, and E.H. Conrad, *The growth and morphology of epitaxial multilayer graphene.* Journal of Physics-Condensed Matter, 2008. **20**(32): p. 27.

19. Starke, U. and C. Riedl, *Epitaxial graphene on SiC(0001) and SiC(000(1)over-bar): from surface reconstructions to carbon electronics.* Journal of Physics-Condensed Matter, 2009. **21**(13): p. 12.

20. de Heer, W.A., et al., *Epitaxial graphene.* Solid State Communications, 2007. **143**(1-2): p. 92-100.

21. Park, S. and R.S. Ruoff, *Chemical methods for the production of graphenes.* Nature Nanotechnology, 2009. **4**(4): p. 217-224.

22. Viculis, L.M., et al., *Intercalation and exfoliation routes to graphite nanoplatelets.* Journal of Materials Chemistry, 2005. **15**(9): p. 974-978.

23. Stankovich, S., et al., *Synthesis and exfoliation of isocyanate-treated graphene oxide nanoplatelets.* Carbon, 2006. **44**(15): p. 3342-3347.

24. Tung, V.C., et al., *High-throughput solution processing of large-scale graphene.* Nat Nano, 2009. **4**(1): p. 25-29.

25. Aizawa, T., et al., *Bond Softening in monolayer graphite formed on transition-metal carbide surfaces.* Physical Review B, 1990. **42**(18): p. 11469-11478.

26. Nagashima, A., et al., *Electronic-structure of monolayer graphite on some transition-metal carbide surfaces.* Surface Science, 1993. **287**: p. 609-613.

27. Itchkawitz, B.S., et al., *Monolayer Graphite on TaC(111)-Electronic Band Structure.* Surface Science, 1994. **318**(3): p. 395-402.

28. Nagashima, A., et al., *Change in the electronic states of graphite overlayers depending on thickness.* Physical Review B, 1994. **50**(7): p. 4756-4763.

29. J. Wintterlin, M.L.B., *Graphene on metal surfaces*, in *Surf. Sci.* 2009. p. 1841.

30. Eizenberg, M. and J.M. Blakely, *Carbon monolayer phse condensation on Ni(111).* Surface Science, 1979. **82**(1): p. 228-236.

31. Hamilton, J.C. and J.M. Blakely, *Carbon segregation to single-crystal surfaces of Pt,Pd and Co.* Surface Science, 1980. **91**(1): p. 199-217.

32. Yu, Q., et al., *Graphene segregated on Ni surfaces and transferred to insulators.* Applied Physics Letters, 2008. **93**(11): p. 113103.

33. K.S. Kim, Y.Z., H. Jang, S.Y. Lee, J.M. Kim, K.S. Kim, J.H. Ahn, P. Kim, J.Y. Choi, B.H. Hong,, *Large-scale pattern growth of graphene films for stretchable transparent electrodes*, in *Nature*. 2009. p. 706.

34. V.K. Portnoi, A.V.L., S.N. Mudretsova, S.A. Fedotov, *Formation of nickel carbide in the course of eformation treatment of Ni-C mixtures*, in *The Physics of Metals and Metallography*. 2010. p. 153.

35. Saenger, K.L., et al., *In situ x-ray diffraction study of graphitic carbon formed during heating and cooling of amorphous-C/Ni bilayers.* Applied Physics Letters. **96**(15): p. 153105.

36. Reina, A., et al., *Large Area, Few-Layer Graphene Films on Arbitrary Substrates by Chemical Vapor Deposition.* Nano Letters, 2009. **9**(1): p. 30-35.

37. Li, X., et al., *Large-Area Synthesis of High-Quality and Uniform Graphene Films on Copper Foils.* Science, 2009. **324**(5932): p. 1312-1314.

38. Hagstrom, S., H.B. Lyon, and G.A. Somorjai, *Surface Structures on the Clean Platinum (100) Surface.* Physical Review Letters, 1965. **15**(11): p. 491.

39. Lyon, H.B. and G.A. Somorjai, *Low-energy electron diffraction study of clean (100) (111) and (110) faces of platinum.* Journal of Chemical Physics, 1967. **46**(7): p. 2539-&.

40. Morgan, A.E. and G.A. Somorjai, *Low energy electron diffraction studies of gas adsorption on Platinum (100) single crystal surface.* Surface Science, 1968. **12**(3): p. 405-&.

41. Eom, D., et al., *Structure and Electronic Properties of Graphene Nanoislands on Co(0001).* Nano Letters, 2009. **9**(8): p. 2844-2848.

42. Varykhalov, A. and O. Rader, *Graphene grown on Co(0001) films and islands: Electronic structure and its precise magnetization dependence.* Physical Review B, 2009. **80**(3): p. 035437.

43. D. W. Goodman, R.D.K., T. E. Madey, J. T. Yates Jr., *D. W. Goodman, R. D. Kelley, T. E. MaKinetics of the hydrogenation of CO over a single crystal nickel catalyst*, in *J. Catal*. 1980. p. 226-234

44. Houston, J.E., D.E. Peebles, and D.W. Goodman, *Auger line shape studies of carbon species on Rh and Ni surfaces.* Journal of Vacuum Science & Technology A: Vacuum, Surfaces, and Films, 1983. **1**(2): p. 995-999.

45. Rosei, R., et al., *Kinetics of carbidic carbon formation from CO in the 10-6-torr range on Ni(110).* Journal of Catalysis, 1983. **83**(1): p. 19-24.

46. Madden, H.H. and G. Ertl, *Decomposition of carbon monoxide on a (110) nickel surface.* Surface Science, 1973. **35**(1): p. 211-226.

47. Kelley, R.D. and D.W. Goodman, *Catalytic methanation over single crystal nickel and ruthenium: Reaction kinetics on different crystal planes and the correlation of surface carbide concentration with reaction rate.* Surface Science Letters, 1982. **123**(2-3): p. L743-L749.

48. Tontegode, A.Y., *Carbon on transition metal surfaces.* Progress in Surface Science, 1991. **38**(3-4): p. 201-429.

49. Rosei, R., et al., *Structure of graphitic carbon on Ni(111)- a surface extended energy loss fine structure study* Physical Review B, 1983. **28**(2): p. 1161-1164.

50. Papagno, L., et al., *Observation of carbidic and graphitic carbon formation from CO in the 10(-5) Torr range on Ru(101)* Surface Science, 1983. **128**(2-3): p. L209-L212.

51. Riviere, J.P.C.a.J.C., *Auger Spectroscopy of Carbon on Nickel*, in *Surf. Sci.* 1971. p. 609-624.

52. M. Eizenberg, J.M.B., *Carbon monolayer phase condensation on Ni(111)*, in *Surf. Sci.* 1979. p. 228.

53. J.C. Shelton, H.R.P., J.M. Blakely, *Equilibrium segregation of carbon to a nickel (111) surface: A surface phase transition*, in *Surf. Sci.* 1974. p. 493.

54. Eizenberg, M. and J.M. Blakely, *Carbon interaction with nickel surfaces: Monolayer formation and structural stability.* The Journal of Chemical Physics, 1979. **71**(8): p. 3467-3477.

55. Fujita, D. and K. Yoshihara, *Surface precipitation process of epitaxially grown graphite (0001) layers on carbon doped Nickel(111) surface.* Journal of Vacuum Science & Technology a-Vacuum Surfaces and Films, 1994. **12**(4): p. 2134-2139.

56. H. Nakano, J.O., J. Nakamura, *Growth mode of carbide from C2H4 or CO on Ni(111)*, in *Surf. Sci.* 2002. p. 256-260.

57. Nakano, H. and J. Nakamura, *Carbide-induced reconstruction initiated at step edges on Ni(111).* Surface Science, 2001. **482**: p. 341-345.

58. Nakano, H., et al., *Carbon deposition by disproportionation of CO on a Ni(977) surface.* Surface Science, 2000. **454**: p. 295-299.

59. Klink, C., et al., *Interaction of C with Ni(100)-atom resolved studies of the clock reconstruction.* Physical Review Letters, 1993. **71**(26): p. 4350-4353.

60. Klink, C., et al., *An stm study of carbon induced structures on Ni(111)- evidence for a carbidic phase clock reconstruction* Surface Science, 1995. **342**(1-3): p. 250-260.

61. C. Klink, I.S., F. Besenbacher, E. Lægsgaard, *An STM study of carbon-induced structures on Ni(111): evidence for a carbidic-phase clock reconstruction*, in *Surf. Sci.* 1995. p. 250-260.

62. Klink, C., et al., *Carbidic carbon on Ni(110): An STM study.* Surface Science, 1996. **360**(1-3): p. 171-179.

63. Hutson, F.L., et al., *Interpretation of the carbon Auger line-shapes for the adsorption and decomposition of ethylene on Ni(100).* Surface Science, 1991. **248**(1-2): p. 119-133.

64. Koel, B.E., J.M. White, and D.W. Goodman, *The adsorption and decomposition of ethylene on Ni(100).* Chemical Physics Letters, 1982. **88**(2): p. 236-242.

65. McConville, C.F., D.P. Woodruff, and S.D. Kevan, *The electronic structure of graphitic overlayers on Ni[100]*. Surface Science Letters, 1986. **171**(2): p. L447-L453.

66. H. H. Hwu, B.F.a.J.G.C., *Different modification effects of carbidic and graphitic carbon on Ni surfaces*, in *Journal of Catalysis 170–177*. 2004. p. 170–177.

67. R. Rosei, M.D.C., F. Sette, C. Quaresima, A. Savoia and P. Perfetti, *'Electronic structure of carbidic and graphitic carbon on Ni(111)'*, in *Phys. Rev. B*. 1984. p. 3416–3422.

68. Usachov, D., et al., *Experimental and theoretical study of the morphology of commensurate and incommensurate graphene layers on Ni single-crystal surfaces.* Physical Review B, 2008. **78**(8): p. 085403.

69. McCarroll, J.J., T. Edmonds, and R.C. Pitkethly, *Interpretation of a Complex Low Energy Electron Diffraction Pattern: Carbonaceous and Sulphur-containing Structures on Ni(111).* Nature, 1969. **223**(5212): p. 1260-1262.

70. Nakamura, J., et al., *Formation of a hybrid surface of carbide and graphite layers on Ni(100) but no hybrid surface on Ni(111).* Surface Science Letters, 1989. **222**(1): p. L809-L817.

71. Hirano, H. and K.-I. Tanaka, *A reason for the structure-insensitive catalytic activity of Ni(100) and Ni(111) surfaces for the methanation reaction of CO.* Journal of Catalysis, 1992. **133**(2): p. 461-466.

72. Gamo, Y., et al., *Atomic structure of monolayer graphite formed on Ni(111).* Surface Science, 1997. **374**(1-3): p. 61-64.

73. H. Kawanowa, H.O., T. Yazaki, Y. Gotoh and R. Souda, *Structure Analysis of Monolayer Graphite on Ni(111) Surface by Li+-Impact Collision Ion Scattering Spectroscopy*, in *Jap. J. Appl. Phys.* 2002. p. 6149-6152.

74. Bertoni, G., et al., *First-principles calculation of the electronic structure and EELS spectra at the graphene/Ni(III) interface.* Physical Review B, 2005. **71**(7): p. 8.

75. Giovannetti, G., et al., *Doping Graphene with Metal Contacts.* Physical Review Letters, 2008. **101**(2): p. 026803.

76. Karpan, V.M., et al., *Graphite and Graphene as Perfect Spin Filters.* Physical Review Letters, 2007. **99**(17): p. 176602.

77. Fuentes-Cabrera, M., et al., *Bridge structure for the graphene/Ni(111) system: A first principles study.* Physical Review B, 2008. **77**(3): p. 035405.

78. Varykhalov, A., et al., *Electronic and Magnetic Properties of Quasifreestanding Graphene on Ni.* Physical Review Letters, 2008. **101**(15): p. 4.

79. Yu. S. Dedkov, A.M.S., V. K. Adamchuk, S. L. Molodtsov, C. Laubschat, A. Bauer and G. Kaindl, *Intercalation of copper underneath a monolayer of graphite on Ni(111),* in *Phys. Rev. B.* (2001). p. 035405

80. Kawanowa, H., et al., *Structure analysis of monolayer graphite on Ni(111) surface by Li+-impact collision ion scattering spectroscopy.* Japanese Journal of Applied Physics Part 1-Regular Papers Short Notes & Review Papers, 2002. **41**(10): p. 6149-6152.

81. D. Farı´as, K.H.R., A. M. Shikin, V. K. Adamchuk, T. Tanaka and C. Oshima, *Modification of the surface phonon dispersion of a graphite monolayer adsorbed on Ni(111) caused by intercalation of Yb, Cu and Ag,* in *Surf. Sci.* 2000. p. 437–441.

82. A. M. Shikin, G.V.P., V. K. Adamchuk, F. Moresco and K.-H. Rieder, *Surface intercalation of gold underneath a graphite monolayer on Ni(111) studied by angle-resolved photoemission and high-resolution electron-energy-loss spectroscopy*, in *Phys. Rev. B.* (2000). p. 13202–13208.

83. Coad, J.P. and J.C. Riviere, *AUGER SPECTROSCOPY OF CARBON ON NICKEL.* Surface Science, 1971. **25**(3): p. 609-&.

84. A. Amoddeo, L.S.C., E. Colavita, *Carbon Auger lineshapes on Ni(111) surface: evidence for new phases*, in *Journal of Electron Spectroscopy and Related Phenomena*. 1993. p. 263-272.

85. Levenson, S.S.a.L.L., *The formation and decomposition of Nickel Carbide in Evaporated Nickel films on graphite,* in *Surf. Sci.*

86. Levenson, M.A.S.a.L.L., *'Final-state effects in carbon Auger spectra of transition-metal carbides,* in *Phys. Rev. B.* 1977. p. 1365-1369

87. S. Sinharoy, M.A.S.a.L.L.L., *Thermal decomposition of Nickel Carbide thin Films*, in *Surf. Sci.* 1978. p. 710-718.

88. A. Grueneis, K.K., D.V. Vyalikh, *Dynamics of graphene growth on a metal surafce: a time-dependent photoemission study,* in *New J. Phys.* 2009. p. 073050.

89. E. Loginova, N.C.B., P.J. Feibelman, K.F. McCarty, *Evidence for graphene growth by C cluster attachment*, in *New J. Phys.* 2008. p. 093026.

90. E. Loginova, N.C.B., P.J. Feibelman, K.F. McCarty, *Factors influencing graphene growth on metal surfaces*, in *New J. Phys.* 2009. p. 063046.

91. Callister, W.D., *Materials science and engineering : an introduction*. 7th ed. 2007, New York: John Wiley & Sons. xxv, 721, A41, G14, S5, I22 p.

92. H. Koschel, G.H., H.P. Steinruck, *The growth of thin Cu layers on Ni(111) studied by CO titration and photoelectron spectroscopy*, in *Surf. Sci.* 2000. p. 201.

93. N'Diaye, A.T., et al., *Two-dimensional Ir cluster lattice on a graphene moire on Ir(111).* Physical Review Letters, 2006. **97**(21): p. 4.

94. J. Coraux, A.T.N.D., M. Engler, C. Busse, D. Wall, N. Buckanie, F.-J. Meyer zu Heringdorf, R. van Gastel, B. Poelsema, T. Michely, *Growth of graphene on Ir(111)*, in *New J. Phys.* 2009. p. 023006.

95. Sutter, P., et al., *Electronic Structure of Few-Layer Epitaxial Graphene on Ru(0001).* Nano Letters, 2009. **9**(7): p. 2654-2660.

96. Sicot, M., et al., *Nucleation and growth of nickel nanoclusters on graphene Moir[e-acute] on Rh(111).* Applied Physics Letters. **96**(9): p. 093115.

97. K.H. Hansen, T.W., S. Stempel, E. Laegsgaard, M. Baumer, H.-J. Freund, F. Besenbacher, I. Stensgaard, *Palladium Nanocrystals on Al2O3: Structure and Adhesion Energy*, in *Phys. Rev. Lett.* 1999. p. 4120.

98. Hong, S.L., Y.H. Shin, and J. Ihm, *Crystal shape of a nickel particle related to carbon nanotube growth.* Japanese Journal of Applied Physics Part 1-Regular Papers Short Notes & Review Papers, 2002. **41**(10): p. 6142-6144.

99. T. Worren, K.H.H., E. Lægsgaard, F. Besenbacher, I. Stensgaard, *Copper clusters on Al2O3/NiAl(1 1 0) studied with STM*, in *Surf. Sci.* 2001. p. 8.

100. L. Vogel Koplitz, O.D., U. Diebold, *STM study of Copper Growth on ZnO(0001)-Zn and ZnO(0001bar)-O surfaces*, in *J. Phys. Chem. B.* 2003. p. 10583.

101. Hashimoto, A., et al., *Direct evidence for atomic defects in graphene layers.* Nature, 2004. **430**(7002): p. 870-873.

102. Lusk, M.T. and L.D. Carr, *Nanoengineering defect structures on graphene.* Physical Review Letters, 2008. **100**(17): p. 4.

103. Meyer, J.C., et al., *Direct Imaging of Lattice Atoms and Topological Defects in Graphene Membranes.* Nano Letters, 2008. **8**(11): p. 3582-3586.

104. Okada, S., et al., *Ferromagnetic spin ordering on carbon nanotubes with topological line defects.* Physical Review B, 2006. **74**(12): p. 4.

105. Botello-Mendez, A.R., et al., *Spin Polarized Conductance in Hybrid Graphene Nanoribbons Using 5-7 Defects.* Acs Nano, 2009. **3**(11): p. 3606-3612.

106. Simonis, P., et al., *STM study of a grain boundary in graphite.* Surface Science, 2002. **511**(1-3): p. 319-322.

107. White, C.T. and J.W. Mintmire, *Fundamental properties of single-wall carbon nanotubes.* Journal of Physical Chemistry B, 2005. **109**(1): p. 52-65.

108. Charlier, J.C., X. Blase, and S. Roche, *Electronic and transport properties of nanotubes.* Reviews of Modern Physics, 2007. **79**(2): p. 677-732.

109. Ritter, K.A. and J.W. Lyding, *The influence of edge structure on the electronic properties of graphene quantum dots and nanoribbons.* Nature Materials, 2009. **8**(3): p. 235-242.

110. Kim, K.S., et al., *Large-scale pattern growth of graphene films for stretchable transparent electrodes.* Nature, 2009. **457**(7230): p. 706-710.

111. Haick, H. and D. Cahen, *Making contact: Connecting molecules electrically to the macroscopic world.* Progress in Surface Science, 2008. **83**(4): p. 217-261.

112. Bunch, J.S., et al., *Impermeable atomic membranes from graphene sheets.* Nano Letters, 2008. **8**(8): p. 2458-2462.

5. SUMMARY AND OUTLOOK

5.1 Summary

This thesis has focused on characterizing the properties of zinc oxide and nickel/graphene interfaces. Here we briefly summarize our results from previous sections.

5.1.1 ZnO interface

The extreme surface sensitivity of soft x-ray photoemission spectroscopy allowed us a new look on the stabilization mechanisms of the polar ZnO surfaces. The O-1*s* and Zn-3*d* core levels exhibit components that can be assigned to bulk and surface ions. No contributions due to plasmon losses are observed in the core-level spectra. For the ZnO (0001)-Zn surface the stabilization mechanism by formation of Zn vacancies is consistent with the observed peaks. Two surface peaks for O-1*s* are assigned to terrace and step sites. The intensity ratio of these two components is in agreement with 1/4 ML of surface Zn-atoms missing. The identification of these two different sites may enable the study of site directed surface chemistry in the future. Attenuation and/or (chemical) shift of the respective O-1*s* components will enable identification of adsorption at steps or terrace sites. This approach may also have further utility for other oxide surfaces, e.g., vicinal surfaces that exhibit surface sites with different Madelung energy and thus characteristic shifts in the core levels [1].

For the ZnO (000–1)-O surface we showed that hydrogen is easily adsorbed. In the absence of hydrogen at elevated temperature, the Fermi level is shifted toward the center of the band gap. This results in depletion of charge carriers in the surface region and thus can contribute to the stabilization of the polar surface. Since the charge-carrier concentration i.e., a positive space-charge region is small in these intrinsically *n*-type doped samples, the shift of the Fermi level alone may not be enough to generate the charge transfer necessary to stabilize the surface. For more highly doped samples the depletion of conduction band electrons may, however, be an effective stabilization mechanism. Such a proposed charge-transfer mechanism may compete with a lowering of the surface energy by adsorption of hydrogen or other adsorbates and thus would enable a tuning of the chemical surface properties.

Soft x-ray photoemission has also been used to investigate the ZnO/ZnS interface [2]. These studies were motivated by the possibility to enhance visible light activity of ZnO and ZnS photocatalysts by formation of interfaces between these two wide band gap materials. Our studies demonstrate that surface functionalization of photoactive materials with a wide band gap material can indeed result in an effective band gap narrowing at the surface. Other surface properties (work function and band bending) may also assist in increasing the photo activity. For large surface area nanomaterials, this surface modification with ZnS will increase the visible light photo absorption. The concurrent formation of hole trapping states at the surface and a space charge region that facilitates charge separation at the surface make this a promising materials system for demonstrating the potential for increasing visible light activity by combining two UV-active photocatalysts. Optimizing the ZnO/ZnS materials system by, e.g., increasing the

strain in the interface layer or formation of multilayer heterostructures, may shift the photoexcitation threshold to even lower energies. Other material systems that combine wide band gap photocatalysts may exist that show similar favorable interface effects. Thus based on our fundamental materials characterization a new paradigm for designing more active photocatalysts, fundamentally different to surface functionalization by narrow band gap materials or bulk doping, is being suggested.

5.1.2 Nickel Graphene interface

We have conducted a comprehensive investigation of graphene growth on Ni(111) substrates and the stability of Ni/graphene interfaces. We showed that a single graphene layer is the thermodynamically preferred carbon-containing surface phase on Ni(111). However, at low carbon concentration a monolayer-thick surface carbide phase may also form on Ni(111). This carbide phase forms rapidly upon hydrocarbon decomposition on Ni(111) surface and covers the entire surface before nucleation of slowly growing graphene. Once the carbide has formed it suppresses graphene nucleation. We demonstrated that the carbide surface phase can be chemically destabilized by alloying the surface with a non-carbide forming metal such as Cu. Such carbide destabilization results in nucleation of graphene and its growth at the surface by carbon segregation from the bulk. Alternatively, the carbide phase can be thermally destabilized by annealing the Ni sample above 480 °C which also causes the unhindered nucleation of graphene. These studies on the nucleation and growth of graphene on transition metal surfaces contribute towards understanding the growth process which are urgently sought for development of effective approaches for growing large area, high quality graphene samples and for tuning its properties by a controlled defect formation.

In order to obtain microscopic and atomic scale information we have studied also graphene growth on Ni(111) using STM. Metal catalysts such as Fe, Co, and Ni are frequently used for the growth of carbon nanotubes and large-scale graphene wafers. The initial atomic-scale growth processes of graphitic carbon on these catalysts are however not well understood. Our atomic level STM studies have shown that a Ni-carbide *surface* phase and graphene can coexist. We have shown that the carbide phase lies in the same surface layer and the two phases match perfectly at their boundary forming a coincidence structure that facilitates the transformation of surface carbide into graphene upon annealing to ~ 900K. Furthermore, the carbide phase imposes the orientation of the graphene layer relative to the Ni(111)-substrate, confirming the importance of the carbide phase in the formation of the graphene layer. These atomic resolved STM studies are the first direct evidence that the graphene sheet may evolve from surface carbide.

In addition to the growth studies we also investigated the nickel-graphene interfaces by depositing Ni on graphene/Ni(111) interface [3]. We have shown that Ni deposits on Ni-supported graphene are unstable at temperatures higher than 100 °C. Formation of carbide allows the Ni deposits to diffuse through the surface layer. After all the Ni deposits have merged with the Ni substrate, the graphene sheet is “healed” and a perfect graphene surface is reformed. Thus, adjusting the annealing temperature and time after Ni deposition allows the controlled destruction of graphene and the formation of Ni-carbide surface phase. Both the surface carbide and the graphene have a lower surface energy than pure Ni and therefore the diffusion of the Ni clusters through the surface layer is lowering the system’s free energy. At the atomic scale, recent computational

predictions have shown that certain transition metals can break the C–C bonds in graphene and this must be the initial step in the formation of the surface carbide [4, 5].

In addition to the growth mechanisms and stability of graphene on Ni, I also have studied the atomic structures of defects formed during graphene growth using STM. We have discovered for the first time extended line defects in graphene [6]. These 1D structures are the consequence of domain boundaries between graphene-sheets occupying different registry relative to the nickel substrate. Atomic resolution STM showed that the line defect consists of fully sp^2 hybridized carbon arranged in pentagons and octagons. Density functional theory showed that these defects have a high density of electronic states at the Fermi-level. The wave functions of these electronic states at the defect decay exponentially into the graphene lattice causing a local doping in the vicinity of the defect. This self-doping effect gives rise to the brighter contrast of the surrounding of the defect in STM images and may allow these line defects to behave as atomic scale wires.

5.2 Outlook

Our research on metal graphene interface has focused on three areas mainly:(i) growth of graphene on Ni substrates, (ii) deposition and stability of Ni clusters on graphene/Ni(111) substrate, and (iii) defects produced in graphene during synthesis. These areas offer many possibilities for future research.

All our experiments have been conducted on Ni(111) substrate. It will be interesting to compare graphene growth on polycrystalline Ni film. Polycrystalline Ni thin film can be deposited on various substrates like SiO_2, YSZ etc. Figure 5.1 shows an

large scale STM image of Ni film on YSZ(111) substrate. In this case large Ni domains of different orientation separated by domain boundaries are present. We can investigate how the grain boundaries, domain size and orientation affect the growth and properties of graphene. Using scanning tunneling microscopy and spectroscopy we will be able to study how the periodicity and orientation of grain boundaries in the substrate affects the electronic property of graphene.

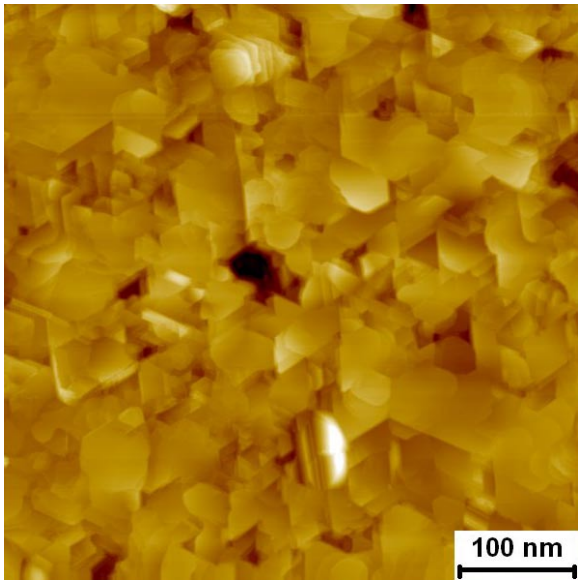

Figure 5.1: STM image of Ni on YSZ(111) substrate

Also, my work concentrated on nickel substrates as the catalyst for graphene growth. Other transition metals also have been used as catalyst for graphene growth but they differ widely in their carbon solubility. Graphene may exhibit different growth mechanisms on these metals so study of graphene growth on different catalyst is needed. For example on Ni graphene grows by surface segregation while on Cu it grows by surface adsorption. We can compare graphene growth on Ni, Cu and Ni-Cu alloys. Addition of Cu to Ni surfaces modifies its catalytic properties so we can tune the

reactivity of Ni by controlled addition of Cu. Ni-Cu alloy catalysts have been used for methane decomposition to control properties and yields of the produced hydrogen and filamentous carbon and therefore I expect addition of Cu to Ni-catalysts to strongly affect the growth of graphene.

Carbon supported metal clusters are also predicted to have unique electronic, magnetic and optical properties [7-10]. Studies of metal cluster on graphene offer many possibilities for future projects. We studied growth of Ni clusters on graphene/Ni(111) substrate at RT. Ni(111) is a special case as it has an excellent lattice match with graphene. Our studies of Ni deposition on graphene/Ni(111) shows that Ni forms 3D clusters at RT with no long range order. Growth of Ni clusters at low temperature might be different as the diffusion of adatoms is reduced so systematic study of growth of Ni clusters on graphene/Ni(111) as a function of temperature and coverage will be interesting as it can be considered as a model catalyst system (metal clusters on a substrate).

It will also be interesting to compare growth of Ni clusters on graphene/Ru(0001) and graphene/Ni(111). Graphene interacts strongly with both substrates but has good lattice match with Ni(111) only. The distance between graphene and Ru(0001) is 1.45 Å while that with Ni(111) is 2.1Å. Due to large lattice mismatch with Ru(0001) graphene forms Moiré structures, which can act as a template for growth of metal clusters. It has been shown that some metal clusters can nucleate either at fcc or hcp sites of Moiré patterns and also give rise to ordered superlattices at low temperatures. Cluster formation depends on metal–carbon bond strength and metal cohesive energies so Ni clusters might

behave differently at on Ru(0001) substrate. Also from the size distribution of the metal clusters we can compare the work of adhesion of the clusters, which will give an estimate if the metallic substrate plays a role in the formation of clusters.

Freestanding graphene at the Fermi level E_F has zero density of states (like a semiconductor) and zero band gap (like a metal). To make electronic devices with graphene it is crucial to modify the electronic structure by inducing a band gap between the π and π* bands, which will control the transport of electrical charges through the graphene sheet. One way to open a bandgap in graphene is by constraining graphene in very narrow nanoribbons with well-defined edges. The edge states depending on their shape (zigzag and armchair) modify the local electronic structure of graphene. One possible method of producing graphene nanoribbons is local destruction of graphene by Ni adsorption on graphene Moiré structure.

Our studies have shown that Ni clusters on graphene/Ni(111) substrate are not very stable and on annealing to ~500K it forms nickel carbide [3]. It will be interesting to see if we observe the same effect on graphene/Ru(0001) substrate. Local variations of the interactions may give rise to an ordered carbide superlattice. Chemical etching of this superlattice at the nanometer scale would enable to transfer this pattern to a free-standing graphene sheet and thus enable us to prepare graphene with a high density of ‘edge sites’. This would be an alternative to the preparation of graphene nano-ribbons for tuning the electronic properties of graphene.

5.3 References

1. Lahiri, J., S. Senanayake, and M. Batzill, *Soft x-ray photoemission of clean and sulfur-covered polar ZnO surfaces: A view of the stabilization of polar oxide surfaces.* Physical Review B, 2008. **78**(15): p. 155414-23.

2. Lahiri, J. and M. Batzill, *Surface functionalization of ZnO photocatalysts with monolayer ZnS.* Journal of Physical Chemistry C, 2008. **112**(11): p. 4304-4307.

3. J. Lahiri, M.B., *Graphene destruction by metal-carbide formation: An approach for patterning of metal-supported graphene*, in *Appl. Phys. Lett.* 2010.

4. E. Loginova, N.C.B., P.J. Feibelman, K.F. McCarty, *Evidence for graphene growth by C cluster attachment*, in *New J. Phys.* 2008. p. 093026.

5. Zhou, Z.H., F. Gao, and D.W. Goodman, *Deposition of metal clusters on single-layer graphene/Ru(0001): Factors that govern cluster growth.* Surface Science. **604**(13-14): p. 1071-L38.

6. J. Lahiri, Y.L., P. Bozkurt, I. I. Oleynik, M. Batzill, *An extended defect in graphene as a metallic wire*, in *Nature Nanotech.* 2010. p. 326.

7. Zhou, Z., F. Gao, and D.W. Goodman, *Deposition of metal clusters on single-layer graphene/Ru(0001): Factors that govern cluster growth.* Surface Science. **604**(13-14): p. L31-L38.

8. N'Diaye, A.T., et al., *Two-dimensional Ir cluster lattice on a graphene moire on Ir(111).* Physical Review Letters, 2006. **97**(21): p. 4.

9. Sicot, M., et al., *Nucleation and growth of nickel nanoclusters on graphene Moir[e-acute] on Rh(111).* Applied Physics Letters. **96**(9): p. 093115.

10. Feibelman, P.J., *Onset of three-dimensional Ir islands on a graphene/Ir(111) template.* Physical Review B, 2009. **80**(8): p. 4.

APPENDICES

Appendix 1: Flowchart of TPD program

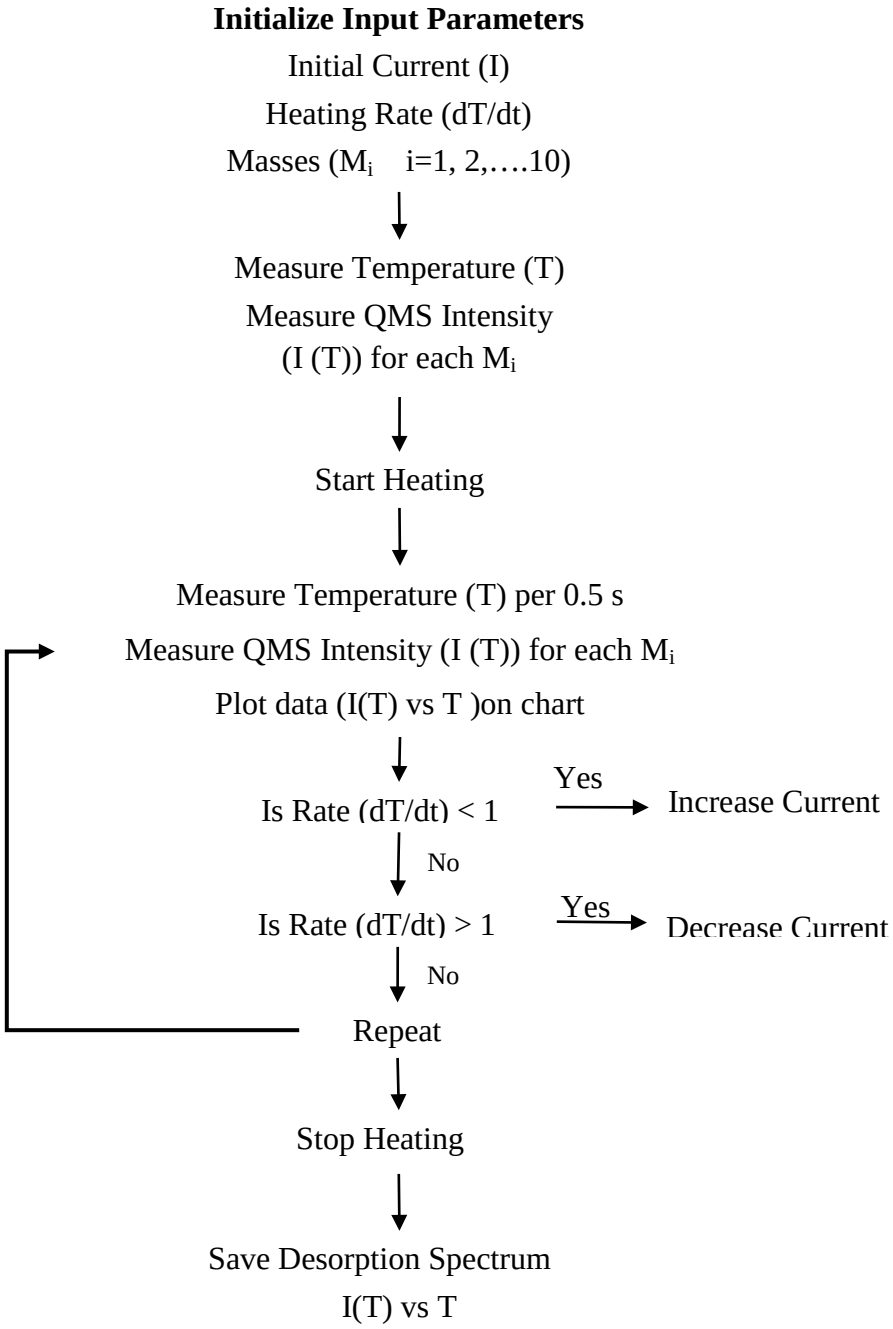

Appendix 2: List of Publications

1. Jayeeta Lahiri, Matthias Batzill "*Graphene destruction by metal-carbide formation: An approach for patterning of metal-supported graphene*" **Applied Physics Letters** 97, 023102 (2010)

2. Jayeeta Lahiri, You Lin , Pinar Bozkurt , Ivan Oleynik , and Matthias Batzill (2010) "*An extended defect in graphene as a metallic wire*" **Nature Nanotechnology** 5, 326 – 329

3. Jayeeta Lahiri , Adam Mayernick , Suzane Morrow, Bruce Koel, Adri van Duin, Dr. Michael Janik, and Matthias Batzill "*Relevance of composition and defects of YSZ(111) surfaces for oxidation of formate*" **Journal of Physical Chemistry C** 114, 5990-5996 (2010)

4. Nikolai Kisov, Jayeeta Lahiri, HimanshuVerma, D. Yogi Goswami, Elias Stefanakos, and Matthias Batzill "*Photocatalytic Degradation of Methyl Orange over Single Crystalline ZnO: Orientation Dependence of Photoactivity and Photostability of ZnO*" **Langmuir** 25 ,3310-3315 (2009)

5. Jayeeta Lahiri, Sanjaya Senanayake , and Matthias Batzill "*Soft x-ray photoemission of clean and sulfur-covered polar ZnO surfaces: A view of the stabilization of polar oxide surfaces*" **Physical Review B** 78 ,155414 (2008)

6. Jayeeta Lahiri, and Matthias Batzill "*Surface functionalization of ZnO photocatalysts with monolayer ZnS"* **Journal of Physical Chemistry C** 112,4304-4307 (2008)

***** Jayeeta Lahiri, Travis Miller, Lyudmyla Adamska, Ivan I. Oleynik, Matthias Batzill "*Graphene growth on Ni(111) by transformation of a surface carbide*" submitted in Nature Communications (2010)

* Jayeeta Lahiri Travis Miller, Andrew Ross, Lyudmila Adamska, Ivan I. Oleynik, Matthias Batzill "*Graphene growth and stability at nickel surfaces*" submitted in New Journal of Physics (2010)

ABOUT THE AUTHOR

Jayeeta Lahiri graduated from Banwarilal Bhalotia College, University of Burdwan, India in 2000 with a Bachelor of Science degree in Physics. She completed a Master of Science degree in Physics from the Banaras Hindu University at Varanasi, India in 2002. She joined the graduate program in University of Wisconsin-Milwaukee, in 2003 and tt transferred to University of South Florida, Tampa in 2005. During her PhD she published six papers in peer reviewed journals. Her paper on "*An extended defect in graphene as a metallic wire*" published in Nature Nanotechnology was highlighted in National Science Foundation(NSF) press release and US News on March 30, 2010 as "A *Tiny Defect That May Create Smaller, Faster Electronics*" Following the completion of her Ph.D., she will begin work as a postdoctoral fellow at Center for Functional Nanomaterials, Brookhaven National Laboratory.